UNIVERSITY OF CATANIA

INTERNATIONAL PhD IN CHEMICAL SCIENCES

XXXV CYCLE

PhD THESIS

Cristina Parisi

Development of Fluorescent Nitric Oxide Photoreleasing Constructs Activatable by Visible Light

Tutor
Prof. Salvatore Sortino

PhD Coordinator
Prof. Salvatore Sortino

SUMMARY

List of abbreviation

ABF: 4-amino-7-nitrobenzofurazane
ACN: acetonitrile
AO: acridine orange
ATP: adenosine 5'-triphosphate
ABC transporters: ATP binding cassette transporters
BSA bovine serum albumin
ct-DNA calf thymus DNA
DAN: 2,3-diamminonaphtalene
DANT diaminonaphthotriazole DANT
DCC: N,N'-dicyclohexylcarbodiimide
DCM: dichloromethane
DMAP: 4-(dimethyl)aminopyridine
DMF: N,N-dimethylformamide
DMSO: dimethylsulfoxide
DNA Deoxyribonucleic acid
DOX Doxorubicin
ER Endoplasmic reticulum
EtOAc: ethylacetate
FDA: Food and Drug Administration
Fl-B Fluorescein Boronate
FRET: Förster resonance energy transfer
IR: infrared
ISC: intersystem crossing
HAS Human Serum Albumin
HOBt Hydroxybenzotriazole
K_b binding constant
MAF MDR Activity Factor
MDR: ultidrug resistance
MTT: 3-(4,5-dimethylthiazol-2-yl)-2,5-diphenyltetrazolium bromide tetrazolium
NADPH nicotinamide adenine dinucleotide phosphate
NBF: nitrobenzofurazane
NHS: N-hydroxysuccinimide
NIR: near Infrared

NMR: nuclear magnetic resonance
NPs Nanoparticles
MS: mass spectroscopy
NIR: Near Infrared
NO: nitric oxide
NOPDT: nitric oxide photodynamic therapy
NOPD: nitric oxide photodonor
NOS: nitric oxide synthase
PBS: phosphate buffered saline
PDT: photodynamic therapy
PB Phosphate buffer
PdI: Polydispersity Index
PE Petroleum ether
PS: photosensitizer
Rf: retentions factor
RNS: reactive nitrogen species
ROS: reactive oxygen species
TEA: triethylamine
THF: tetrahydrofuran
TLC: thin layer chromatography
UV/ Vis: ultraviolet/visible

Chapter 1

Abstract

The alarmingly low turnover of new clinically approved anticancer drugs and the Multi Drug Resistance (MDR) phenomena emerging for drugs actually used, call for an urgent shift of attention to other “unconventional” and underexplored therapeutic modalities. The generation of reactive oxygen species (ROS) and reactive nitrogen species (RNS) as alternative therapeutic agent with great spatiotemporal control by using light stimulus has gained an increasing interest in the last years, opening new horizons for innovative therapeutic treatment. In this respect, the present project aims to contribute to spur new solutions in the field of “unconventional” therapies exclusively based on the photoregulated generation of nitric oxide (NO) as intriguing alternative to those based on the “conventional” anticancer drugs. NO offers unique advantages over conventional drug: i) it is a multitarget species, ii) it does not suffer of MDR issues, ii) it has a short lifetime and diffuses over short distances avoiding undesired systemic effects.

This work focuses on the design, synthesis, characterization and therapeutic applications of novel, fluorescent NO photodonors (NOPDs) activatable with the biocompatible visible light. Many of the NOPD developed are based on a main chromophoric unit, which act as a visible light harvesting antenna, covalently bound to a N-nitrosoaniline derivative as NO-releasing moiety, through an insulator spacer. Basically, these hybrids exploit the excitation energy of the antenna to

trigger an intramolecular electron transfer with the NO-releasing moiety that, in turn, stimulates the detachment of NO without significantly affect the emissive properties of the antenna. The fluorescence emission of the antenna is a key property to allow the visualization of the NOPD within a cellular environment, a fundamental requisite in view of image-guided phototherapies. In fact, excitation with low intensity light generates fluorescence emission, which allows its tracking in the biological environment. Afterwards, excitation with high intensity light can provide a highly localized burst of NO precisely at the desired sites.

Moreover, part of this work has been focused on the development of innovative constructs incorporating not only NOPDs but also photosensitizers (PS) for the simultaneous generation of NO and singlet oxygen ($^1O_2$) under visible light stimulus. In recent years indeed, the use of NO in combination with photodynamic therapies (PDT) is emerging as one of the most suitable strategies because opening new possibilities in the field of multimodal therapeutic strategies. This new approach aims at exploiting the additive or synergistic effects arising from the activity of multiple therapeutic species in order to amplify the therapeutic activity and minimize the side effects.

Chapter 2

Introduction

2.1 General background

Drug resistance is a well-known phenomenon that results when diseases become tolerant to pharmaceutical treatments. This concept was first considered when was discovered that some bacteria were resistant to certain antibiotics, but since then similar mechanisms have been found to occur in other diseases, including cancer. It is a natural process that will occur, sooner or later, with every drug. However, incorrect practices have made the inevitable development of drug resistance happen much sooner, rather than later. As a consequence, many drugs are being lost. Unfortunately, the approval of new drugs for clinical applications is not proceeding as fast as the emergence of new cases of MDR. In other words, resistance is moving faster than research and this problem cannot be longer ignored.

The Multi Drug Resistance (MDR) phenomena emerging for drugs actually used and the alarmingly low turnover of new clinically approved anticancer and antibacterial drugs, call for an urgent shift of attention to other “unconventional” and underexplored therapeutic modalities. The generation of reactive oxygen species

(ROS) and reactive nitrogen species (RNS) as “unconventional” therapeutic agent may open new horizons for innovative therapeutic modalities.

2.2 Nitric Oxide as unconventional therapeutic agent

Among ROS and RNS, the odourless, colourless and highly reactive radical nitric oxide (NO) has been the object of an increasing interest in the fascinating world of biomedical sciences. After being considered for a lot of years as an atmospheric pollutant produced from industrial processes, automobile exhausts and electrical storms, in 1992 it became the journal of Science ‘molecule of the year’ and six years later Drs Furchgott, Ignarro and Murad shared the Nobel Prize for Physiology and Medicine for their major discoveries surrounding NO [1]. The reasons of this success can be ascribed to its involvement in a number of physiological and pathophysiological processes. In fact, NO plays a fundamental role in the bioregulation of vital functions such as neurotransmission, hormone secretion and vasodilatation [2], and is involved in important biological processes like wound healing [3], cancer biology [4] and bacterial infections [5].

Nitric oxide is generated in vivo by the oxidation of the amino acid L-Arginine under the catalytic activity of the nitric oxide synthases (NOSs). This reaction (reported in Figure 1) requires nicotinamide adenine dinucleotide phosphate (NADPH) and oxygen (O_2) as co-substrates and yields NO and L-citrulline as end products [6].

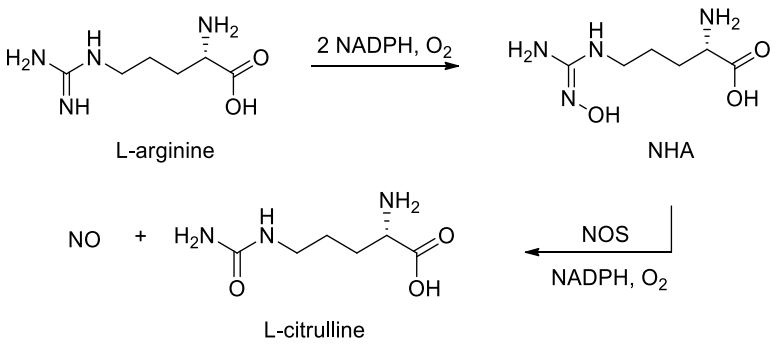

Figure 1. Endogenous NO production.

There are three main NOS isoforms: neuronal NOS (nNOS), endothelial NOS (eNOS) and inducible NOS (iNOS). The first two, nNOS and eNOS are always expressed in neuronal and endothelial cells; nNOS is involved in neurotransmission in the central and peripheral nervous systems; eNOS releases NO which causes vasodilation or inhibition of platelet aggregation. iNOS has been founded in macrophages and its expression is induced by the presence of inflammatory cytokines, oxidative stress and various endotoxins; its activation leads to a large quantity of NO as part of the body's immune response [7].

Although NO's bio-molecular role is still not completely understood, its multifaceted role has stimulated, over the last few years, a massive interest in the development of new NO-based therapies with the exciting prospect to tackle important diseases. Some of these therapies have demonstrated success in clinical settings [8]. Indeed, NO offers unique advantages over conventional drugs: i) it is a multitarget species, able to attack biological substrates of different nature like lipids, deoxyribonucleic acid (DNA) and proteins; not only ii) it does not present MDR issues encountered with several conventional drugs but iii) it can be also used as a tool to fight MDR since it can inhibit the activity of efflux pumps mainly responsible for MDR phenomena; iii) by virtue of its short half-life (<5 s), lack of

charge and small size, it diffuses in the cellular environment over short distances allowing to confine its reactivity in a restricted region of space [9] and to reduce systemic side effects common to many conventional drugs.

In general, current therapies may be categorized into two groups:

1. drugs that interfere with the NOS's activity, altering in this way the endogenous production of NO;
2. materials that release NO.

2.3 NO-donors: from aspecific donors to NO-photodonors

The direct use of gaseous NO through inhalation has proven successful for limited medical applications; for example, its use for the clinical treatment of persistent pulmonary hypertension of newborn (PPHN) was initiated many years ago and is still on-going [10]. However, due to the high reactivity and inconvenient handling of this gaseous species, the development of NO donors, in other words scaffolds able to store NO and release it under appropriate stimuli, has gained an increasing interest. Many classes of NO donors already exist, and few have been translated to the clinic, including organic nitrates, *N*-diazeniumdiolates (NONOates) and metal nitrosyls. However, they are non-specific: some of them release NO spontaneously, in other cases the NO release can be modulated by stimuli such as temperature, pH or enzymes [11], stimuli that obviously cannot be finely controlled especially in a biological environment. In view of a successful medical treatment, it is highly recommended to finely control the release of this radical species. The final activity of NO, especially in oncology is dependent on several factors: its working microenvironment, including the type of cell exposed to the compound, the final intracellular concentration, and the duration of intracellular exposure to NO, creating a complex role for this molecule in opposing beneficial and deleterious

events. For example, NO plays a double-edged role in tumour biology, acting as a tumor progressor or suppressor [12]. In fact, micromolar concentrations of NO significantly inhibit tumor growth in different ways: inducing oxidative and nitrosative stress, leading to DNA base deamination, nitrosylation of enzymes, enhancing inflammatory reactions, inhibiting mitochondrial respiration and cell apoptosis [13]. On the other hand, picomolar concentrations of NO present anti-apoptotic effects and promote angiogenesis thereby increasing nutrient delivery and facilitating tumor growth [4, 14]. This dichotomy has made mandatory the control of release in terms of space, time and dosage. Light is the perfect minimally invasive and finely controllable external stimulus to control the NO release. The idea consists in the use of appropriate **NO "photocaging"** compounds in which NO is temporary inactivated by its covalent incorporation within a photoresponsive chromogenic center (the photocage). Activation of the photosensitive moiety liberates NO in its active form allowing to confine its site of action at the illuminated area with great spatiotemporal accuracy and to define its dosage by tuning the light intensity and/or duration (Figure 2).

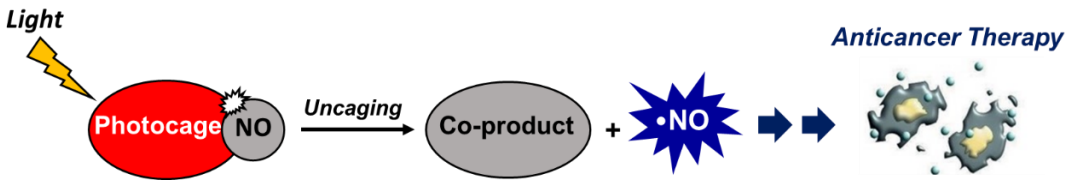

Figure 2. The photouncacing process: light-activation of the photocage liberates NO in its active form.

Moreover, light triggering is biofriendly, provides fast reaction rates and does not perturb physiological parameters like temperature and pH, fundamental requisite for biomedical applications [15]. These features make the NO photodonors (NOPD) a powerful and promising therapeutic arsenal.

A suitable NOPD must have some fundamental requisite: i) be stable and non-toxic in the dark; ii) have an efficient quantum yield of NO production; iii) conduce to the formation of non-toxic coproducts which do not absorb in the same region of the NOPD in order to avoid undesired inner filter effects and secondary photochemical reactions; iv) be activated by biocompatible light: NOPD activatable by visible light are highly preferable to those activated by UV due to its reduced toxicity and deeper penetration into tissues.

Several NO photocages based on transition metals complexes have been developed in the last years, especially in the groups of Ford and Mascharak by virtue of their good photochemical performances in the Vis/NIR region; however, toxicity issues related to the transition metals may represent serious drawbacks [16]. Only very limited examples of organic metal-free NOPD activatable with one- photon visible light have been developed [17]. They include mainly nitro derivatives that bear appropriate substituents at the *o*- and *p*-positions [18], some BODIPY [19] and rhodamine derivatives [20].

Novel NOPD activatable with the biocompatible green light have been developed in the group of Professor Sortino [21]; they are based on a main chromophoric unit, which act as a visible light harvesting antenna, covalently linked through an insulator spacer to the N-nitroso derivative of 4-nitro-3-(trifluoremetyl)aniline, which act as NO-releasing moiety. BODIPY and Rhodamine have been chosen as antennae by virtue of their intense absorption and emission properties in the visible spectral range. These two NOPD present many advantages: they have been prepared through simple synthetic steps, combine clean NO release exclusively regulated by the highly biocompatible green light with remarkable quantum efficiencies and present good fluorescence emission performances in the green and orange region, which allow their track within the cellular environment.

The uncaging of NO from these NOPD is triggered by a photoinduced electron transfer from the N-nitrosoaniline-derivative moiety, which acts as electron donor, to the excited state of the antenna, which acts as electron acceptor. As illustrated in Figure 3, a back-electron transfer leads to the detachment of NO from the nitrosamine and to the formation of an anilino radical derivative which is stabilized by the presence of the electron drawing nitro and trifluoromethyl groups. This radical evolves to the stable photoproducts via H-transfer from solvent.

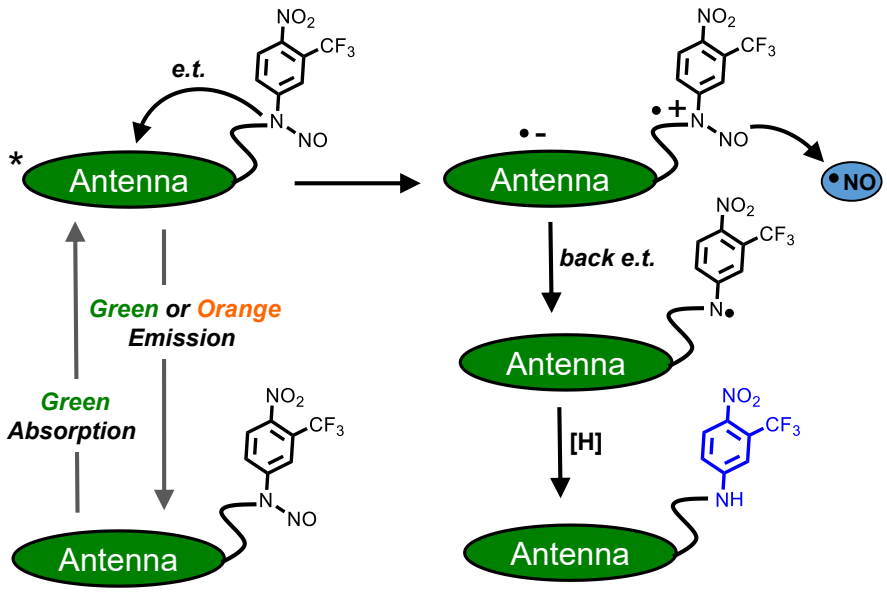

Figure 3. Proposed mechanism for the NO release triggered by green light.

2.4 Fluorescent NO-Photodonors

In view of a therapeutic use of NOPD, their visualization in a cellular environment represents an indispensable requisite to be addressed. This purpose can be reached through the aid of fluorogenic components, offering great prospects in view of image-guided phototherapies based on NO. In this way, excitation of the NOPD with low intensity light generates fluorescence emission which allows its tracking in the

biological environment. Afterwards, excitation with high intensity light can provide a highly localized burst of NO precisely at the desired sites.

Although several NO-photocages lack of emissive properties, the problem can be surmounted through the combination of the photocage with suitable fluorogenic centers.

As discussed above, the biological effects of NO have been shown to be highly site-, concentration- and dosage-dependent. Another important issue to be faced regards the quantification and the localization of NO released in a biological system. In this case the problem can be surmounted through the use of systems based on the principle of the "*release with fluorescence reporting"* illustrated in Figure 4.

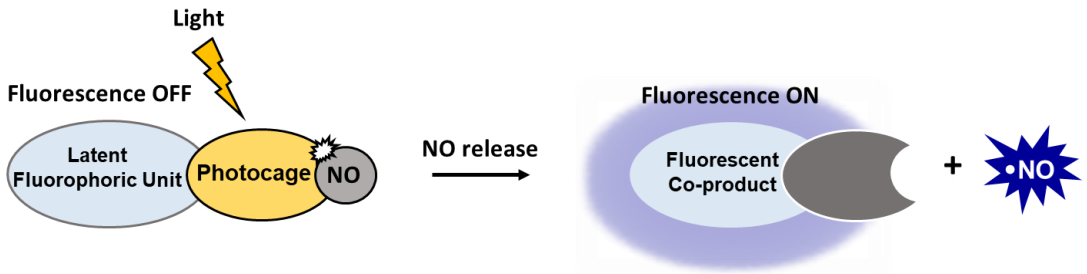

Figure 4. The principle of the "release with fluorescence reporting" which can be used to quantify and localize the NO released.

The photocage is covalently linked to a fluorophoric unit whose fluorescence is temporarily quenched by intermolecular processes. Photoexcitation of the photocage and consequent release of NO generate a co-product whose fluorescence is restored [22]. In this way, the uncaging process can be quantified by monitoring the fluorescence emission of the reporter and, furthermore, the spatial distribution of the released species in a biological environment can be followed in real time by fluorescence microscopy.

2.5 Combination of PDT with NOPDs

Photodynamic therapy (PDT) is a well-known therapeutic modality used for the treatment of malignant lesions like cancer and a variety of localized microbial infection [23]. This innovative therapeutic modality is based on the effects generated by the appropriate combination of Vis/NIR light with a photosensitizer (PS) in presence of molecular oxygen. Under light excitation, PS passes from the ground state to the excited state and can decay to the ground state with concomitant emission of light in the form of fluorescence or may undergo intersystem crossing to form a more stable and long-lived excited triplet state (Figure 5). This latter can be quenched by nearby molecular oxygen via energy transfer mechanism (Type II reaction) which leads to the generation of the highly reactive singlet oxygen ($^1O_2$) and/or via electron transfer mechanisms (Type I reaction), leading to the formation of other ROS [24].

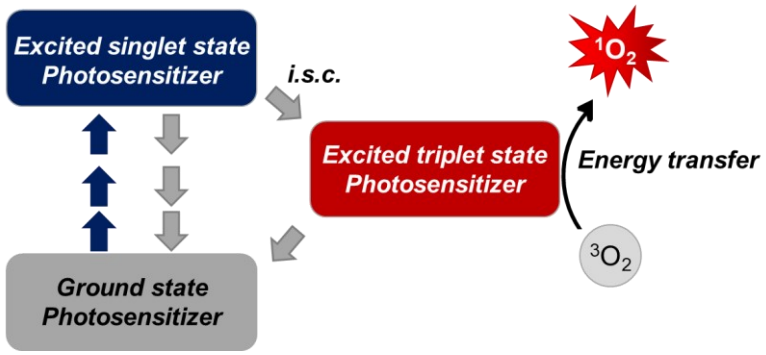

Figure 5. Photocatalytic production of $^1O_2$ in PDT.

Both Type I and Type II reactions can occur simultaneously and competitively, and the ratio between these processes depends on the type of PS used, on the concentrations of substrate and oxygen. However, Type II reaction appears to play

a central role in cytotoxicity, because of the efficient interaction of $^1O_2$ with various biomolecules [25].

In recent years, the combination of PDT with other unconventional therapeutic treatment controlled with the light is emerging as one of the most suitable strategies. This new approach aims at exploiting the additive or synergistic effects arising from the activity of multiple therapeutic species in order to amplify the therapeutic activity and minimize the side effects. The combination of PDT with the controlled release of NO is opening new possibilities in the field of multimodal therapeutic strategies. NO and $^1O_2$ share important features like small size, capability to be multitarget species, absence of MDR and confinement of their activity over short distances. Moreover, NO photorelease is independent of O_2 availability and it can complement PDT under hypoxic conditions typical of some tumours, where PDT may fail [26].

Chapter 3

Results and discussions

3.1 DNA-targeted NO release photoregulated by green light

3.1.1 Design

DNA is the most important biomacromolecule since it carriers the genetic instructions for the correct functioning and development of living organisms. For this reason, it is considered the prime intracellular target for several pharmaceutical agents. In this regard, DNA has been labelled as the main target of NO; it can induce nitrosative deamination of the DNA bases causing AT → GC transition mutation [27] and leading to strand breaks.

The achievement of novel NOPDs able to bind DNA and to release NO upon light stimuli even after DNA binding represents a challenging objective to follow. This is not an easy task because, in principle, localization of photoresponsive guests in specific pockets of a biosubstrate with particular hydrophobicity and in the presence of steric constrains and specific interactions, could lead to competitive processes. As a result the photochemical performances can be affected in nature, efficiency or both. Based on the above considerations, a novel NOPD for the photocontrolled generation of NO nearby DNA has been developed (Figure 6) [28].

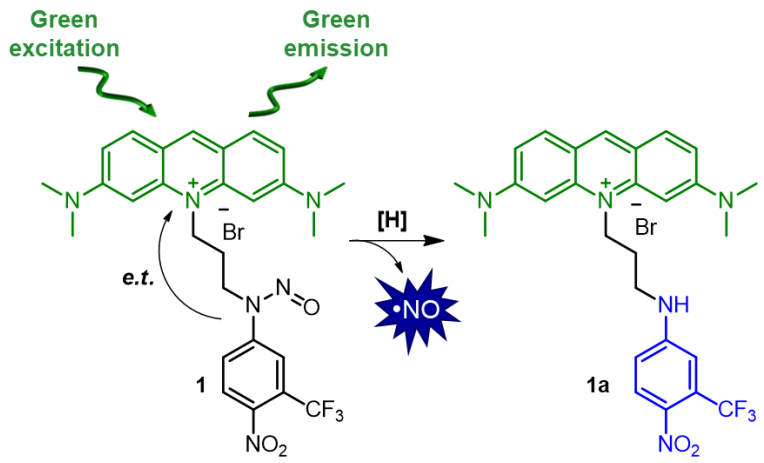

Figure 6. Structure of hybrid **1**, proposed mechanism for the NO release and its main photoproduct **1a**.

It consists of acridine orange (AO) which will act not only as DNA binder but also as a green light harvesting antenna, covalently linked to an N-nitrosoaniline appendage as NO releasing unit, through a flexible alkyl spacer. Photoexcitation of the hybrid with the biocompatible green light results in an intense fluorescence emission and triggers NO detachment from the N-nitroso moiety via an intramolecular electron transfer. AO was chosen mainly for two reasons: it is a well-known DNA binder, whose derivative are extensively used in biology as standard compounds for nuclear staining due to their strong emission properties, as well as for therapeutic applications [29]. Moreover, AO is a good electron acceptor in the excited state, so it is expected to encourage NO detachment from the N-nitroso moiety according to the mechanism reported in Figure 3.

3.1.2 Synthesis

Compounds **1** and the corresponding non-nitrosate compound **1a** were synthesized according to the procedure reported in Scheme 1. Briefly the commercially

available compound **1b** was subjected to aromatic nucleophilic substitution with 3-aminopropan-1-ol to give aniline derivative **1c**. Acridinium derivative **1a** was obtained reacting acridine orange with the tosylate **1d** in DMF at 100 °C. Compound **1** was obtained through nitrosation of **1a** with $NaNO_2$ and CH_3COOH.

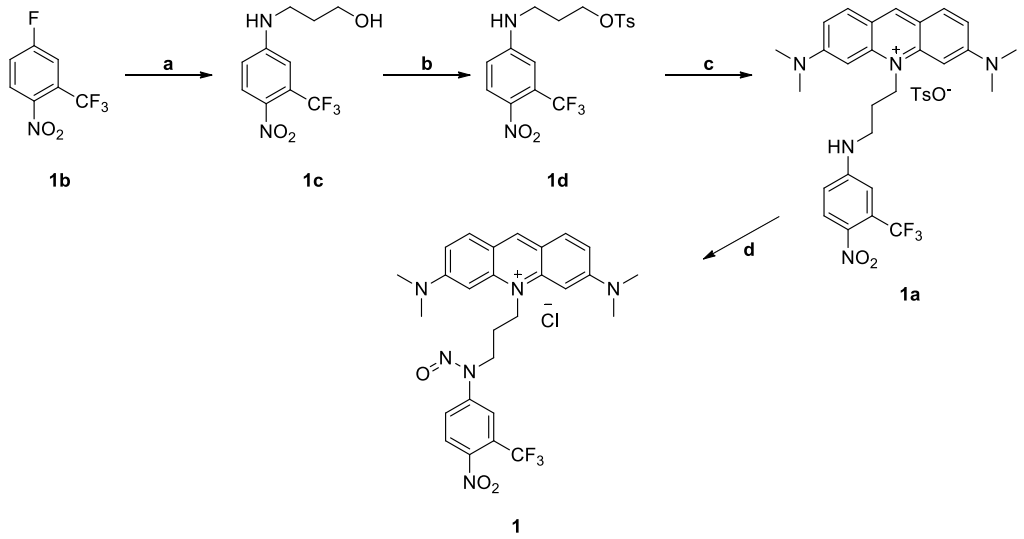

Scheme 1. (a) 3-aminopropan-1-ol, K_2CO_3, CH_3CN, reflux, 18 hours, 77%; (b) Et_3N, *p*-toluenesulfonyl chloride, CH_3CN, room temperature, 24 hours; (c) acridine orange, DMF, 100 °C, 72 hours, 46%; (d) $NaNO_2$, CH_3COOH, CH_3OH, room temperature, 48 hours, ion-exchange, 48 hours, 22%.

3-{[4-Nitro-3-(trifluoromethyl)phenyl]amino}propan-1-ol (1c).

4-Fluoro-1-nitro-2-(trifluoromethyl)benzene **1b** (10 mmol), 3-aminopropan-1-ol (1.5 eq.) and K_2CO_3 (2 eq.) were dispersed in 20 mL of CH_3CN. The mixture was refluxed for 18 hours; the solvent was removed under reduced pressure, the residue was taken with water and the mixture was filtered under vacuum to obtain the title compound as a yellow solid. Yield: 77%. Mp. (H_2O): 112 °C. MS: 265 $[M+1]^+$; ^{1}H-NMR (d_6-DMSO): δ 8.06 (1H, d, J = 9.1 Hz), 7.55 (1H, t, J = 5.1 Hz), 7.05 (1H, broad s), 6.80 (1H, dd, J = 9.1 Hz, 2.6 Hz), 4.57 (1H, t, J = 4.9 Hz), 3.50 (2H, q, J = 5.9 Hz),

3.23 (2H, m), 1.71 (2H, quin, J = 6.6 Hz). ^{13}C (d_6-DMSO): δ 153.3, 133.4, 129.8, 125.0 (q, ^2J_F = 32 Hz), 122.6 (q, ^1J_F = 272 Hz), 111.6, 111.0, 58.1, 39.4, 31.4.

3,6-Bis(dimethylamino)-10-(3-{[4-nitro-3(trifluoromethyl)phenyl]amino}propyl) acridin-10-ium-4-methylbenzene-1-sulfonate (1a).

Compound **1c** (5 mmol) was dissolved in 10 mL of CH_2Cl_2; Et_3N (1.5 eq.) and *p*-toluenesulfonyl chloride (1.2 eq.) were added and the solution was stirred at room temperature for 24 hours. The mixture was then washed with water, saturated solution of $NaHCO_3$ and brine, dried over Na_2SO_4, filtered and distilled under reduced pressure. Without further purification, intermediate **1d** was dissolved in 10 mL of DMF; acridine orange (2 eq.) was added to the solution and the mixture was stirred at 100 °C for 72 hours. The mixture was concentrated under reduced pressure and the residue was purified through flash-chromatography on aluminium oxide eluting with CH_2Cl_2:CH_3OH (98:2 v/v) to afford the title product as a red solid. The NMR sample was converted into the corresponding chloride through ion exchange. Yield: 46%. Purity: 95%. Mp.: 157 °C. MS: 512 $[M]^+$; ^{1}H-NMR (CD_3OD): δ 8.71 (1H, s), 8.02 (1H, d, J = 9.3 Hz), 7.94 (2H, d, J = 9.3 Hz), 7.28 (2H, dd, J = 9.3 Hz, 2.1 Hz), 7.0 (1H, d, J = 2.4 Hz), 6.84 (1H, dd, J = 9.1 Hz, 2.6 Hz), 6.73 (2H, m), 4.89 (2H, m), 3.57 (2H, t, J = 6.0 Hz), 3.24 (12H, s), 2.37 (2H, m). ^{13}C (CF_3COOH + $CDCl_3$): δ 156.4, 144.5, 142.9, 135.9, 130.4, 128.9, 125.0, 121.9, 118.2, 116.0 (q, ^2J_F = 52 Hz), 115.1 (q, ^1J_F = 142 Hz), 114.5, 113.8, 111.9, 53.0, 44.6 (two overlapping peaks), 24.3.

3,6-Bis(dimethylamino)-10-(3-{[4-nitro-3-3,6-bis(dimethylamino)-10-(3-{[4-nitro-3-(trifluoromethyl)phenyl](nitroso)amino}propyl)acridin-10-ium chloride (1).

Compound **1a** (1 mmol) was suspended in 15 mL of methanol; $NaNO_2$ (5 eq.) and CH_3COOH (5 eq.) were added and the mixture was stirred at room temperature for

48 hours. The mixture was then concentrated under reduced pressure, taken up with water and filtered under vacuum. The residue was purified through flash-chromatography on aluminium oxide eluting with CH_2Cl_2:CH_3OH (99:1 v/v). The red solid thus obtained was treated with ion-exchange resin to afford the title product. Yield: 22%. Purity: 95%. Mp.: 135 °C. MS: 541 $[M]^+$; ^{1}H-NMR (d_6-DMSO): δ 8.83 (1H, s), 8.36 (1H, d, J = 8.3 Hz), 8.27 (2H, m), 7.96 (2H, d, J = 9.6 Hz), 7.31 (2H, d, J = 9.6 Hz), 6.72 (2H, s), 4.86 (2H, m), 4.52 (2H, m), 3.33 (12H, s), 2.05 (2H, m). ^{13}C (D^6-DMSO): δ 156.6, 145.0, 144.4, 143.1, 142.2, 133.2, 127.6, 123.0 (q, ^2J_F = 40 Hz), 122.9, 119.1 (q, ^1J_F = 261 Hz), 117.4, 116.5, 114.5, 92.4, 44.0, 40.4, 40.1, 22.0.

3.1.3 Photochemical characterization and NO release

The absorption spectra of compounds **1** and **1a** (see Figure 7A) in MeOH:H_2O (80:20 v:v) are dominated by the band with the maximum at 500 nm and a shoulder at 478 nm: this band is attributable to the AO dye. The shoulder at 478 nm is due to the presence of dimeric species, which results from the self-association of the AO rings. In fact, the dye mainly exists in its monomeric form in diluted aqueous solution, starts to dimerize at about 10 µM concentration and above 1 mM concentration it almost exclusively exists in the dimeric form [30]. The absorption spectrum of **1a** is characterized by the presence of a band at 380 nm which arises from of the push-pull character of the nitroaniline moiety. This band is absent int the absorption spectrum of compound **1** due to the presence of the electron withdrawing NO group attached at the amino functionality.

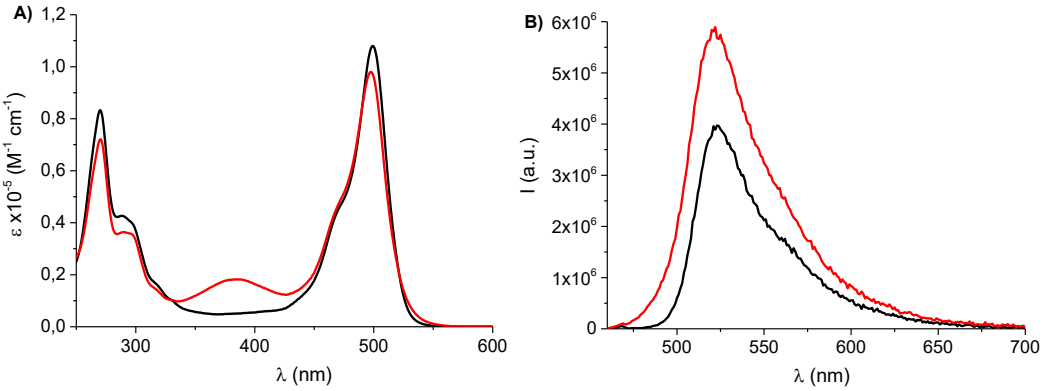

Figure 7. A) Absorption and B) fluorescence emission spectra of a solution of **1** (black line) and **1a** (red line) in MeOH:H_2O (80:20 v/v). The emission spectra have been recorded at λ_{exc} = 470 nm using two optically matched solutions.

Interestingly, the presence of the NO donor appendage does not turn off the emissive properties of the AO dye (see Figure 7B). Both compounds **1** and **1a** show an intense green fluorescence emission, with a fluorescence quantum yield, Φ_f, of 0.23 in the case of compound **1** and a Φ_f = 0.35 in the case of compound **1a**. The related fluorescence decays show a dominant component with a lifetime, τ of 1.10 ns for compound **1** and. τ = 1.40 ns for compound **1a**. These values suggest the presence of a photoprocess competitive with the fluorescence emission in compound **1** and which will be explained later.

Photoexcitation of the hybrid **1** with green light triggers NO detachment from the N-nitroso moiety. Figure 8A shows the absorption spectral changes observed during irradiation of a solution of **1** (MeOH:H_2O 80:20 v/v, 60 minutes) with green light under aerobic conditions. They show the appearance of a new absorption band at 384 nm which clearly arise by the loss of the NO from the nitrosamine and the restored amino group of the nitroaniline moiety. Moreover, the absorption spectrum at the end of the photolysis is identical to that of compound **1a**.

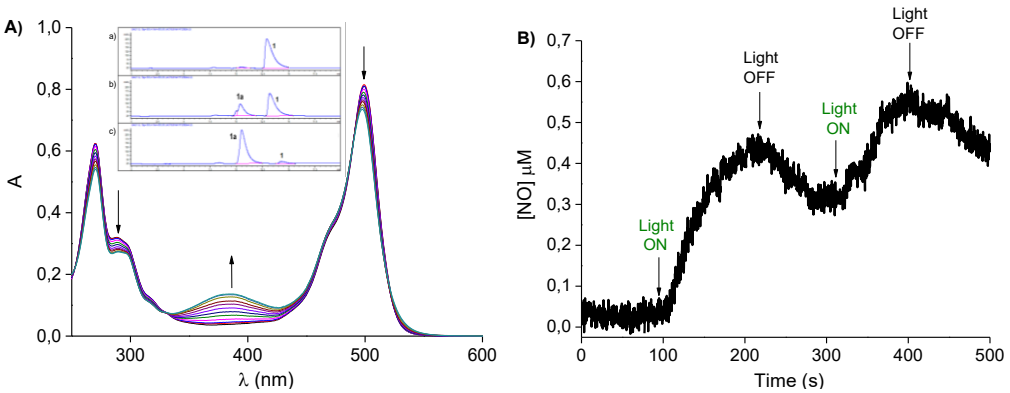

Figure 8. A) Absorption spectral changes observed upon exposure of a solution of **1** in MeOH:H_2O (80:20 v/v) at λ_{exc} = 532 nm for time intervals from 0 to 60 min. The arrows indicate the course of the spectral profile with the illumination time. The inset shows HPLC traces (monitored at 500 nm) related to solutions of **1** after a) 5 minutes, b) 30 minutes and c) 50 minutes of irradiation with green light. B) NO release profile observed for a solution of **1** in MeOH:H_2O (80:20 v/v) upon alternate cycles of light and dark.

The presence of isosbestic points is indicative of the occurrence of a clean photochemical reaction. HPLC analysis carried out using compound **1a** as reference allow to confirm both the nature of the photoproduct and the purity of the photoreaction (inset Figure 8A). Moreover, the photolysis profile and the kinetic behaviour is identical to that observed under N_2-saturated conditions, suggesting that the presence of oxygen does not affect neither the nature nor the efficiency of the photochemical reaction. These data, together with the smaller fluorescence quantum yields and the faster fluorescence decay observed with compound **1** rules out the participation of the long lived excited triplet states and accounts for a photochemical pathway mediated by the short lived excited singlet state.

The NO release was unequivocally demonstrated by the direct detection of this radical species through an amperometric technique using an ultrasensitive NO electrode. Figure 8B shows that NO release takes place exclusively under light stimulus: indeed, it starts under green light stimulus, stops in the dark, and restarts once the green light is turned on again. The quantum yield for the NO photorelease,

Φ_{NO} was $0.9x10^{-3}$, in good agreement with the other NOPDs activatable with green light working with a similar mechanism [21, 31].

Since the AO is the sole unit absorbing the green light, photorelease of NO from the nitro-derivative moiety must necessarily involve an electronic communication between these two components. A photoinduced energy transfer from the excited AO to the nitroso-derivative appendage is thermodynamically uphill. The uncaging of NO from **1** seems to be triggered by the photoinduced electron transfer from the N-nitrosoaniline-derivative moiety, which act as electron donor, to the excited singlet states of the antenna, which act as electron acceptor. This is in according to what recently observed with BODIPYs and Rhodamine antennae linked to the same nitroso derivative moiety [21]. The proposed mechanism is also supported by the considerable changes in free energy for the photoinduced electron transfer process, $\Delta G \cong -0.7$ eV estimated by the Rehm-Weller equation 1 [32]:

$$\Delta G = e[E_{ox} - E_{red}] - E_{0,0} \quad (1)$$

where E_{ox} is the half-wave potential for one-electron oxidation of the electron-donor unit, ca. 1 eV vs. SCE [33], E_{red} is the half-wave potential for one-electron reduction of the electron-acceptor unit, ca. –0.7 vs. SCE [34] and $E_{0,0}$ is the energy of the lowest excited singlet state of the AO antennae, respectively [35].

Such photoinduced electron transfer between two species separated by insulator spacers like in the case of **1** requires their very close spatial vicinity. This was confirmed by a conformational study conducted through well-tempered metadynamics simulation [36]; the molecule assumes an U-shape conformation characterized by a π-π stacking between the benzene-like ring of AO moiety and the nitro-aniline ring (see Figure 9).

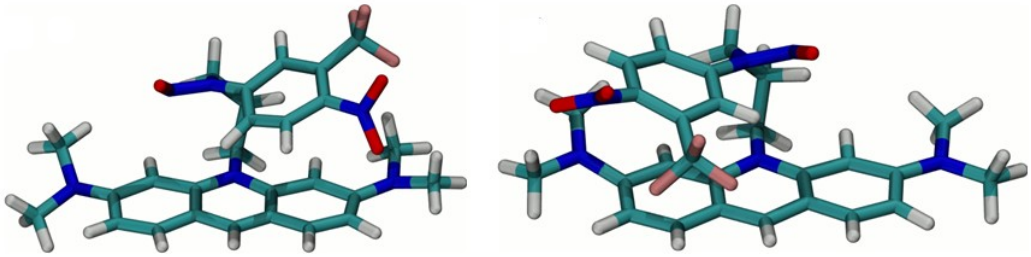

Figure 9. U-shaped conformation assumed by the molecular hybrid **1** during MD simulations.

3.1.4 Interaction with ct-DNA

As already mentioned, AO is an excellent DNA binder. The characterization of the photochemical behaviour of the NOPD after DNA binding is of fundamental importance: some competitive processes can occur after the localization of the photoresponsive guest within a specific pocket of a biosubstrate by virtue of the characteristics of the microenvironment (hydrophobic or hydrophilic), presence of steric costrains and specific interactions that can affect in nature and/or efficiency the photochemical performances of the NOPD [37]. For this reason, interaction of compound **1** with calf thymus DNA (ct-DNA) has been object of study. Spectroscopic techniques such as UV-Vis absorption and fluorescence spectroscopy are largely used to investigate changes in the physicochemical properties of small molecules in the presence of different biomolecules [38].

The first aspect to be analyzed is the interaction mode of the hybrid with the DNA. Dyes can interact with DNA through covalent or noncovalent interactions. These latter are the most desired due to their reversible and dynamic nature and can be of three types: (i) intercalative mode of binding, where planar dye molecules are intercalated between DNA base pairs through π–π interactions, (ii) groove binding, where drug molecules bind either to the minor or the major grooves of the DNA helix, and (iii) electrostatic or surface binding, where cationic dye/drug molecules

electrostatically bind to the negatively charged DNA surfaces composed of the phosphate backbones [39].

The behavior of a solution of compound **1** in presence of increasing concentration of ct-DNA has been explored. The absorption spectrum of compound **1** (9 µM) in H_2O:DMSO (90:10 v/v) in absence of the biopolymer (black spectrum of Figure 10A) is similar to that observed in MeOH:H_2O (80:20 v/v), with a maximum at 503 nm and a shoulder at 478 nm arising from the presence of dimeric species which, however, at the concentration used, are present in small amount.

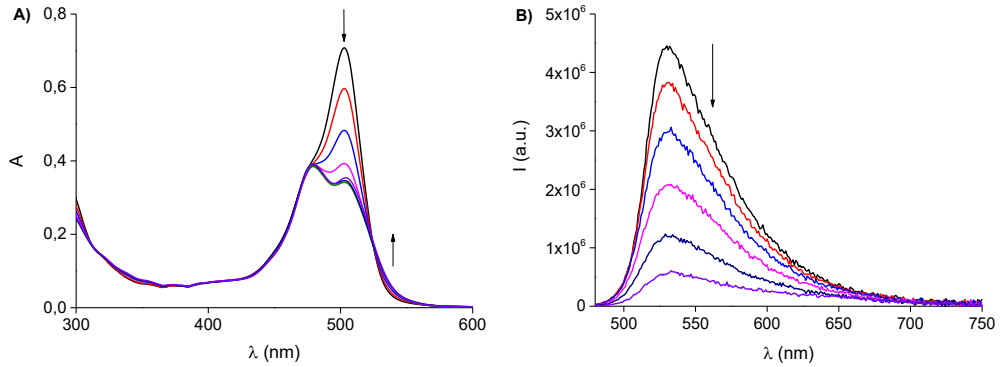

Figure 10. A) Absorption spectral changes and B) fluorescence emission spectra (λ_{exc} =470 nm) observed for solution of **1** (9 µM) upon addition of ct-DNA from 0 to 14.4 µM ([ct-DNA]$_{bp}$:[**1**] = 1,6), H_2O:DMSO (90:10 v/v).

Initial addition of DNA leads to a change of the spectral shape until a [ct-DNA]$_{bp}$:[**1**] = 1.6, with a decrease of the absorbance at 503 nm and the absorption at 478 nm which become the main absorption band (Figure 10A). Such a spectroscopic behaviour is indicative of the fact that the dimeric form prevails over the monomeric form. The fluorescence emission spectra reported in Figure 10B show a considerable decrease in the fluorescence intensity up to a [ct-DNA]$_{bp}$:[**1**] ratios = 1.6; indeed, dimeric species are weakly emissive due to self-quenching phenomena encouraged by their proximity. These results converge towards an unique explanation: a DNA-assisted dimerization of the AO moiety. In view of the positive

charge of AO, this behaviour can be due to external stacking of the hybrid on the biopolymer surface stabilized by the negative charge of the phosphate backbone of the DNA though electrostatic interactions. Moreover, the fluorescence decay of **1** observed before and after the addition of ct-DNA show a dominant component with τ = 2.1 ns. The decay observed after the addition of ct-DNA is due to the presence of residual monomeric species in solution and probably the decay of the dimers falls in a time window below the instrumental time-resolution (200 ps).

Further addition of DNA leads to a reversal of the absorption features with the partial restoring of the peak of the monomer which, however, was red-shifted to 506 nm (Figure 11A). Moreover, the fluorescence emission spectra reported in Figure 11B show a partial restoring of the fluorescence. A saturation for this second binding process was observed for $[\text{ct-DNA}]_{bp}$:[**1**] ratios >100.

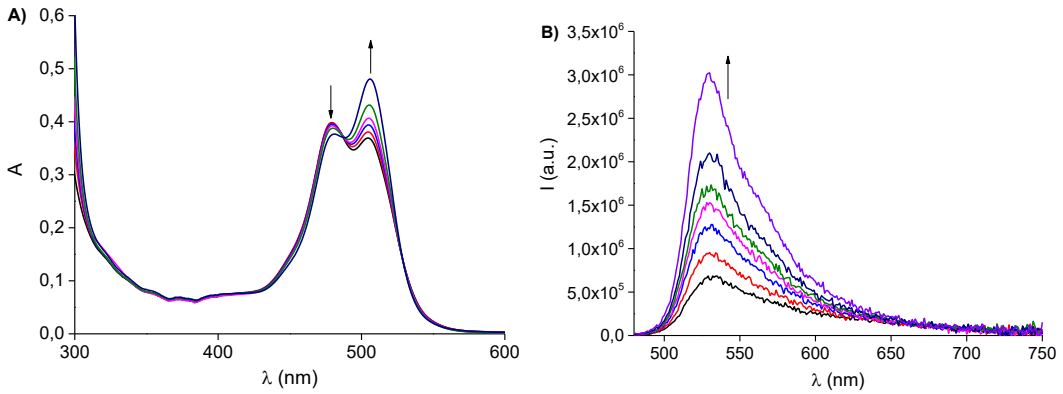

Figure 11. A)Absorption spectral changes and B) fluorescence emission spectra (λ_{exc} =470 nm) observed for solution of **1** (9 µM) upon addition of ct-DNA from 14.4 µM to 1440 µM ($[\text{ct-DNA}]_{bp}$:[**1**] = 160), H_2O:DMSO (90:10 v/v).

These data suggest that at such higher $[\text{ct-DNA}]_{bp}$:[**1**] ratio, the dimerization process becomes less important due to the increase of the concentration of the DNA and that the monomeric form prevails over the dimeric one. The observed red shift of the monomer band is indicative of an intercalative binding mode of the AO dye

between the DNA bases which is stabilized by π-π interactions [40, 41]. However, the smaller spectral shift observed in this case when compared with other AO and its derivatives with pendant functional units, seems to suggest a partial intercalation of **1** between the DNA base pair. This hypothesis is supported by the partial restore of the hybrid's fluorescence emission. Pal et al. explored the binding of AO dye in a large range of DNA concentration [40a]. At $[\text{ct-DNA}]_{bp}$:[**1**] ratios higher than 1,6, the authors found a notable increase of the fluorescence intensity, which was larger than that of the free AO. This behavior is typical for a fully intercalative binding mode. The fact that in the case of compound **1** the fluorescence remains lower than that of the free **1** confirms that monomeric **1** interacts with DNA through a partial intercalation. Moreover, the fluorescence decay of **1** in presence of a large excess of DNA shows a dominant component of 3.6 ns probably due to the restricted rotational and vibrational motions of the fluorogenic centre bound to the biopolymer. This lengthening in the lifetime is smaller than that reported in literature for AO fully intercalated between DNA base pairs.

3.1.5 Determination of the DNA binding constants

The spectroscopic data were used to calculate the binding constant (K_b). Due to the two-different binding mode observed, the K_b related to the first (K_b^1) and the second (K_b^2) binding event were calculated using two different equations.

The K_b^1 was estimated by using the absorption spectral changes reported in figure 10A. The half-reciprocal plot fitted well the data of Figure 10A according to the equation 2 [42]:

$$[\text{ct-DNA}]_{bp}/(\varepsilon_A-\varepsilon_F) = [\text{ct-DNA}]_{bp}/(\varepsilon_B-\varepsilon_F) + 1/K_b^1\,(\varepsilon_B-\varepsilon_F) \qquad (2)$$

where $[ct\text{-}DNA]_{bp}$ is the concentration of the polynucleotide in base pairs, ε_A, ε_F and ε_B correspond to $A_{obs}/[\mathbf{1}]$, the extinction coefficient for the free **1** and the extinction coefficient for the totally bound form of **1** after the first association step, respectively. The K_b^1 value has been evaluated by the ratio of the slope to intercept of the linear plot in Figure 12A and gives a K_b^1 value of 2.1×10^5 M^{-1}. This value is more than one order of magnitude larger than that reported for the self-dimerization process of AO [43], in excellent agreement with the DNA-assisted dimerization of **1**.

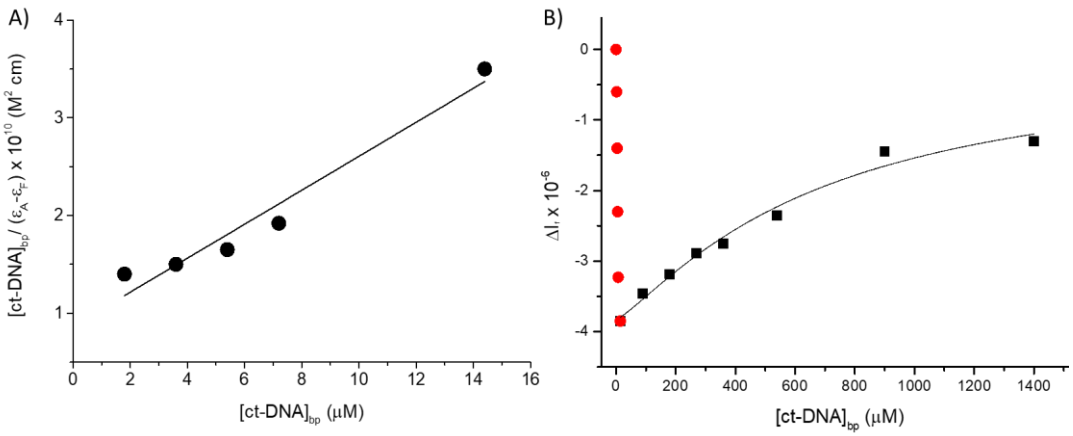

Figure 12. A) Half-reciprocal plot of binding of **1** with ct-DNA determined using the absorbance changes observed in Figure 10A at λ = 503 nm. B) Fluorescence intensity differences of **1** observed at λ = 530 in the presence of increasing amounts of ct-DNA from $[ct\text{-}DNA]_{bp}$:[**1**] = 0 to 1.6 (●) and from $[ct\text{-}DNA]_{bp}$:[**1**] = 1.6 to 160 (■) and determined using the fluorescence changes observed in Figure 11B. The continuous line is the fit of the experimental data related to the second step of the binding process.

The K_b^2 was estimated by using the fluorescence emission spectral changes reported in Figure 11B. The K_b^2 value was calculated correlating the changes in the fluorescence intensity (ΔI_f) with the added ct-DNA concentration according to the equation 3 [44]:

$$\Delta I_f = \Delta I_f^{\infty} K_b^2[\text{ct-DNA}]^n_{bp}/1+ K_b^2[\text{ct-DNA}]^n_{bp} \quad (3)$$

where ΔI_f^{∞} is the saturation value of the change in the fluorescence intensity and n is the number of binding sites for each molecule of **1**. As shown in Figure 12B, this equation could be applied quite satisfactory for the second step of the titration resulting in a K_b^2 value of $1.2x10^4$ M^{-1} and *n* = 1.4. Both values are lower than that reported for a fully intercalative binding of AO [40] and their derivatives [41], conferring a quantitative confirmation for the proposed partial intercalation binding.

3.1.6 Evaluation of the NO release after binding with DNA

As mentioned above, the preservation of the photochemical performances of the NOPDs after the binding with a biopolymer is of fundamental importance. For this reason, after the investigation of the binding mode between compound **1** and DNA, the work focused on the evaluation of the capability of compound **1** to release NO once bounded to DNA and if the different binding mode can affect the release of NO. At first, it was explored the photoreactivity of the free **1** in H_2O:DMSO (90:10 v/v) which is the solvent mixture used in all experiments performed in the presence of ct-DNA. Irradiation of this solution with green light leads to the same absorption spectral changes observed in MeOH:H_2O and to the formation of compound **1a** as the only stable photoproducts, as confirmed by HPLC analysis (data not shown). The quantum yield for this process was Φ_{NO} = $0.7x10^{-3}$, only slightly lower than that found in MeOH:H_2O.

At this point, the capability of **1** to release NO once bounded to DNA has been evaluated. The evaluation was performed at $[\text{ct-DNA}]_{bp}$:[**1**] ratios of 1.6 and 160. Irradiation of these two solutions leads to the same absorption spectral changes

observed in absence of DNA, with the restoring of the absorption band at ca 400 nm arising from the push-pull character of the nitroaniline moiety (Figure 13A and 13B). The reaction profiles show an identical behaviour in presence of different [ct-DNA]$_{bp}$:[**1**] ratios with quantum yields of 0.8x10^{-3} for ratio 1.6 and 0.9x10^{-3} for ratio 160.

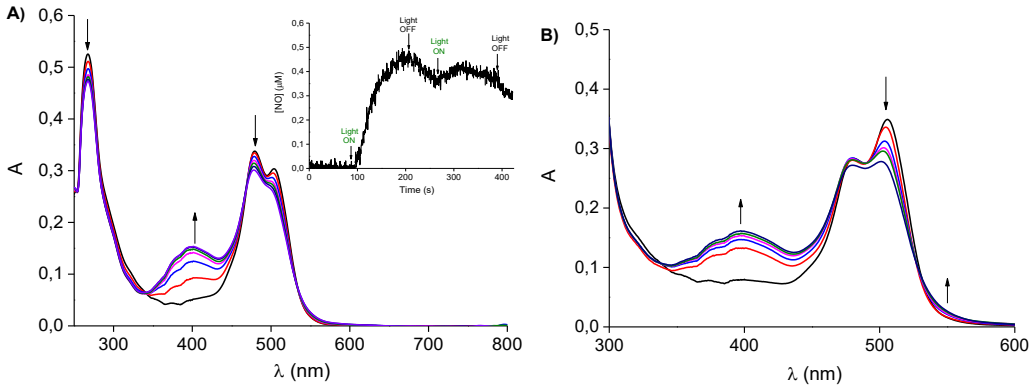

Figure 13. Absorption spectral changes observed upon exposure of a solution of **1** (8 μM) at λ_{exc} = 532 nm for different time intervals from 0 to 40 min in the presence of A) ct-DNA 12.8 μM ([ct-DNA]$_{bp}$:[**1**] = 1.6) and B) ct-DNA 1280 μM ([ct-DNA]$_{bp}$:[**1**] = 160. The arrows indicate the course of the spectral profile with the illumination time. The inset shows NO release profiles observed upon green light irradiation.

The NO release was also demonstrated by its direct detection through an amperometric technique using the ultrasensitive NO electrode. The amperogram reported in the inset of Figure 13A unequivocally shows the green light-regulated release of NO from the complex between **1** and the biopolymer. The similar values of Φ_{NO} found in the absence and in the presence of ct-DNA also suggests that neither the massive dimerization of **1** occurring at DNA surface nor its partial intercalation affect the nature and the efficiency of the photochemical reaction.

These results are confirmed by the conformational studies performed to evaluate the probable conformation adopted by **1** under the two different DNA binding modes. At first, the binding of a single molecule of **1** with DNA was simulated. Both

the formation of stacking interaction at the beginning/ending of the double helix (figure 14A) and the free intercalation of the ligand (figure 14B) were observed. Figure 14B, in particular, shows how the ligand assumes the U-shaped conformation intercalating the double stranded DNA.

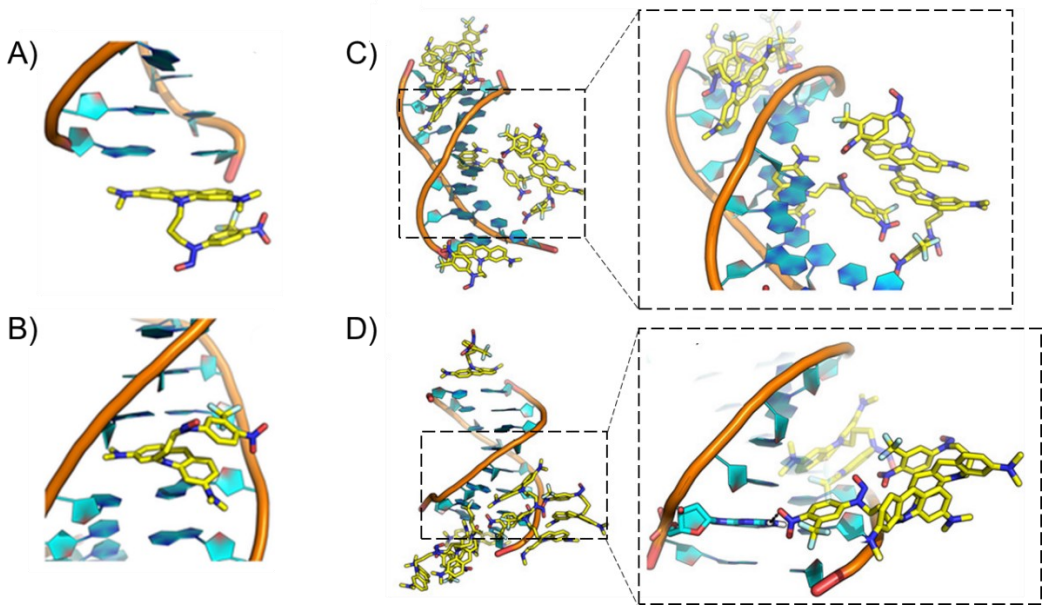

Figure 14. Possible orientations assumed by **1** when submitted to molecular dynamics simulations in the presence of a DNA octamer. A) One single molecule of **1** interacts with the last base pair. B) One single molecule of **1** intercalates among G-C and C-G base pairs and assumes the U-shaped conformation. C) and D) Aggregation of the acridine derivatives around the DNA octamer as simulated by molecular dynamics. The H-bond between the derivative and a guanine base in D) is shown as black dashed line. The DNA is shown as carton, the ligands as capped sticks.

Then seven copies of **1** have been submitted to simulation. Once again, it has been observed the stacking interactions at the ends of the double helix. Most importantly, numerous aggregations formed (Figure 14C and 14D) with some of theme preserving the U-shaped form that allows NO release. In Figure 14D one ligand H-bonds with a guanine through the nitro group, while forming π–π contacts with other two molecules, one of those is in the U-shaped conformation. These

studies showed that whatever the binding mode between compound **1** and the biopolymer, the former assumes mainly the U-shape conformation which is essential for the intramolecular electron transfer triggering the NO release.

3.1.7 Conclusion

In summary, it has been reported a novel photoactivable, molecular hybrid based on AO antenna. Photoexcitation of the AO with the highly biocompatible green light results in intense fluorescence emission and triggers the NO detachment from the N-nitroso appendage via an intramolecular electron transfer. Moreover, the presence of the AO moiety encourages the binding with DNA through a dual-mode binding depending on the DNA:molecular hybrid molar ratio. The NO photorelease performances of the hybrid are not affected by the different binding mode with the biopolymer thanks to the maintenance of the U-shape conformation of the hybrid, a fundamental requisite for the electron transfer and as a consequence to observe the NO release. These properties make the presented compound an intriguing candidate for potential applicative research studies where NO delivery in the DNA proximity precisely regulated by the biocompatible green light is required.

3.2 NO release regulated by doxorubicin as green light-harvesting antenna

3.2.1 Design

Doxorubicin (DOX) is an anthracycline derivative, which represents one of the most potent anti-cancer drugs for the treatment of a large variety of solid tumors, including breast, ovarian, bladder and lung tumors. However, its clinical use is hindered by the emergency of MDR, a problem that cannot be overcome by increasing dosage due to the serious side effects caused by this drug, first of all the cardiotoxicity. Different mechanisms are at the basis of MDR, but it has been seen that the resistance to DOX is mainly exerted through its increased efflux from the cancer cells as result of the overexpression of adenosine 5'-triphosphate (ATP) binding cassette (ABC) transporters. Many strategies have been proposed to overcome DOX resistance and amplify its antitumor activity, like its coadministration with compounds able to inhibit the activity of ABC transporters [45]. NO is the ideal candidate for this purpose. When it is generated within a certain concentration range (nM to mM), NO can inhibit the activity of these pumps through a mechanism involving nitration of critical tyrosine residues. Combination of DOX with NOPDs has recently proven a suitable strategy to overcome DOX resistance and amplify its antitumor activity [46, 65].

With this in mind, a novel NOPD operated by DOX as light-harvesting antenna has been developed [47]. It permits NO uncaging from a N-nitroso appendage upon selective excitation of DOX with the highly biocompatible green light, without precluding its typical red emission useful for the localization of the NOPD within the cellular environment (Figure 15).

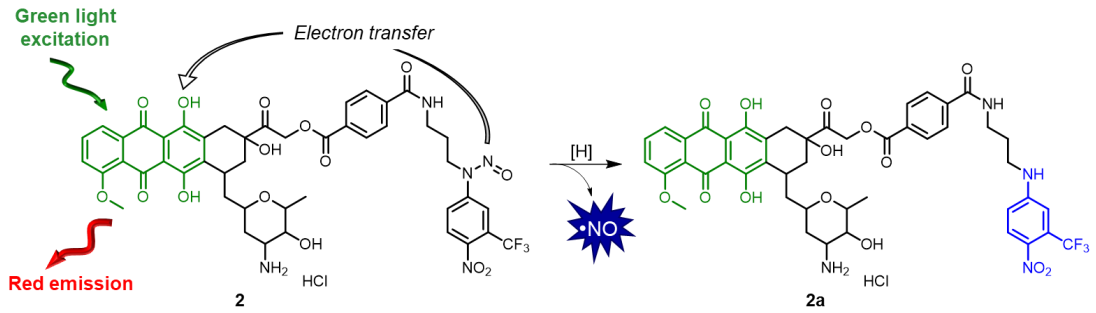

Figure 15. Structure of the hybrid **2**, proposed mechanism for the NO release and its main photoproduct **2a**.

3.2.2 Synthesis

Compound **2** was synthesized according to the procedure reported in Scheme 2. Compound **2b** was prepared as reported in literature [65]. Briefly compound **2c**, which was obtained through nitrosation of **2b** with $NaNO_2$ and CH_3COOH, was covalently linked to a mixture of 14-bromo and 14-chlorodaunorubicine hydrobromide **2d** to obtain the final compound **2**. All syntheses were carried out under a low intensity level of visible light.

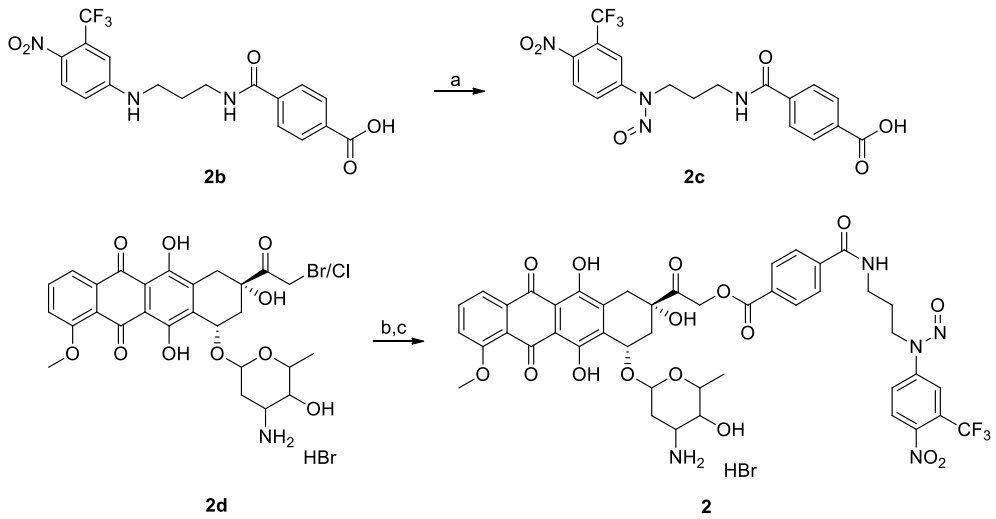

Scheme 2. a) $NaNO_2$, CH_3COOH:THF 1:1, r.t.; b) **a2**, KF, DMF, rt; c) THF, HCl in dry dioxane.

4-((3-((4-Nitro-3(trifluoromethyl)phenyl)(nitroso)amino)propyl)carbamoyl) benzoic acid (2c).

To a solution of **2b** (760 mg, 1.85 mmol) in a mixture of THF:CH_3COOH (1:1 v/v; 150 mL) cooled at 0 °C with an ice bath, sodium nitrite (1 g, 14.78 mmol) was added; the reaction mixture was stirred at 0 °C for 2 h. Then, the mixture was stirred for another 12 h at room temperature. When the reaction was completed (TLC), the obtained mixture was diluted with DCM and washed with water (3 × 20 mL), dried over Na_2SO_4 and concentrated to dryness. Purification of the residue by flash chromatography, using CH_2Cl_2:MeOH (95:5 v/v) as the eluent, gave the target compound **2c** as a yellow solid (474 mg, 58%). ESI MS $[M-H]^-$: 439.

Doxorubicin-4-((3-((4-nitro-3-(trifluoromethyl)phenyl)(nitroso)amino)propyl) carbamoyl) benzoate (2).

To a stirred solution of **2c** (366 mg, 0.83 mmol) in dry DMF, KF (96 mg, 1.66 mmol) was added in one portion, and the reaction was vigorously stirred for 15 min. 14-Bromo/chloro daunorubicin hydrobromide **2d** (184 mg, 0.28 mmol) was added and the reaction was stirred at rt for 4 h. Solvent was removed under reduced pressure at 30°C and the resulting mixture was purified by flash chromatography CH_2Cl_2:MeOH (95:5 to 80:20 v/v) as the eluent to give a dark-red solid. The resulting compound was suspended in dry THF (10 mL), and 2 equivalents of HCl solution in dry dioxane were added. The resulting mixture was stirred for 1 h at rt and then diluted with Et_2O. The resulting precipitate was filtered, washed with Et_2O and dried under vacuum to give the title compound **2** as a red powder (123 mg, 44%). ESI MS $[M+H]^+$: 966. ^1H NMR (500 MHz, DMSO-d_6) δ 8.68 (t, *J* = 5.6 Hz, 1H, CONH), 8.33 (d, *J* = 8.8 Hz, 1H, CHAr), 8.23 (d, *J* = 2.4 Hz, 1H, CHAr), 8.20 (dd, *J* = 8.8, 2.4 Hz, 1H, CHAr), 8.07 (d, *J* = 8.2 Hz, 2H, CHAr), 7.94 (d, *J* = 8.2 Hz, 2H, CHAr), 7.92 (d, *J* = 4.6

Hz, 2H, ^{1}CHAr , ^{3}CHAr), 7.66 (t, *J* = 5.2, 4.6 Hz, 1H, ^{2}CHAr), 5.76 (s, 1H, ^{9}COH), 5.57 – 5.44 (m, 2H, $^{14}CH_2$), 5.30 (d, *J* = 3.5 Hz, 1H, $^{1'}$CH), 4.99 (dd, *J* = 5.5, 2.9 Hz, 1H, ^{7}CH), 4.23 (m, *J* = 6.0, 5.5 Hz, 3H, $^{5'}$CH, -CH_2CH_2CH2-N(NO)), 3.98 (s, 3H, -OCH_3), 3.57 (s, 1H, $^{4'}$CHOH), 3.25 (m, 2H, -$CH_2CH_2CH_2$-), 3.12 (d, *J* = 18.1 Hz, 1H, $^{10}CH_2$), 2.95 (d, *J* = 18.1 Hz, 1H, $^{10}CH_2$), 2.38 – 2.32 (m, 1H, $^{8}CH_2$), 2.13 (m, 1H, $^{8}CH_2$), 1.88 (td, *J* = 12.7, 3.8 Hz, 1H, $^{2'}$CH), 1.78 – 1.64 (m, 3H, -$CH_2CH_2CH_2$-, $^{3'}$CH), 1.19 (d, *J* = 6.5 Hz, 3H, $^{6'}CH_3$). ^{13}C NMR (126 MHz, DMSO-d_6) δ 207.70, 206.18, 188.63, 186.51, 165.34, 164.69, 160.83, 155.94, 150.25, 144.44, 138.72, 136.30, 135.15, 134.76, 133.85, 131.15, 129.26, 127.58, 127.55, 123.42, 123.41, 120.02, 117.85, 117.80, 110.82, 110.73, 99.33, 75.21, 69.64, 66.61, 66.22, 56.62, 46.60, 40.49, 40.02, 36.89, 36.16, 31.93, 28.51, 28.47, 25.77, 16.68.

3.2.3 Photochemical characterization and NO release

The absorption spectrum of compound **2** is dominated by the DOX chromophore showing a main intense band with maximum at ca. 490 nm and extending in the whole green region (black line Figure 16A). Differently to the absorption spectrum of the analogue non-nitrosate compound **2a** (red line Figure 16A), the hybrid **2** does not show the intense absorption band at 390 nm arising from of the push-pull character of the nitroaniline moiety, due to the presence of the electron withdrawing NO group attached at the amino functionality.

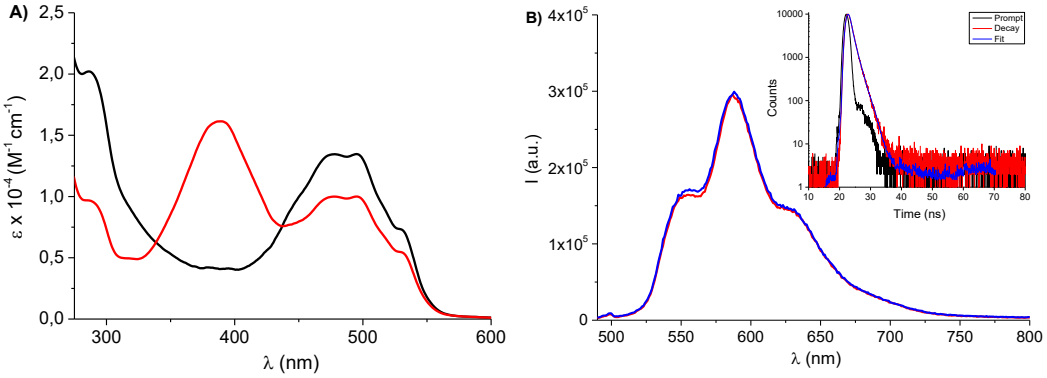

Figure 16. A) Absorption spectra of a solution of **2** (black line) and **2a** (red line) in MeOH:H_2O (80:20 v/v). B) Fluorescence emission spectra of **2** and free DOX recorded using two optically matched solutions in MeOH:H_2O (80:20 v/v). λ_{exc} = 480 nm. The inset shows the fluorescence decay and the related fitting of the same solution of **2** recorded at λ_{exc} = 455 nm and λ_{em} = 600 nm.

The fluorescence emission spectra reported in figure 16B show the presence of the N-nitroso appendage does not influence the emissive properties of the DOX moiety. In fact, **2** displays the typical red fluorescence emission of the free DOX with a quantum yield, Φ_f of 0.06 and related fluorescence decay with a dominant component of 1.4 ns (inset figure 16B), both values identical to that observed for the free DOX.

Irradiation of a solution of **2** (MeOH:H_2O 80:20 v/v) with green light leads to the detachment of NO from N-nitrosamine moiety; this is clearly demonstrated by the restoring of the absorption band with a maximum at 390 nm (see figure 17A) and by the real time detection of NO through an amperometric technique (see figure 17B). This latter also demonstrate that the release of NO is exclusively regulated by the green light since it starts when the green light is turned on and stops when it is turned off. The isosbestic points present in the photolysis profile are indicative of a clean photochemical reaction and the absorption spectrum at the end of the photolysis is identical to that of compound **2a**: this indicate compound **2a** as the

principle photoproduct. This hypothesis has been confirmed by HPLC analyses carried out using compound **2a** as reference (see inset figure 17A).

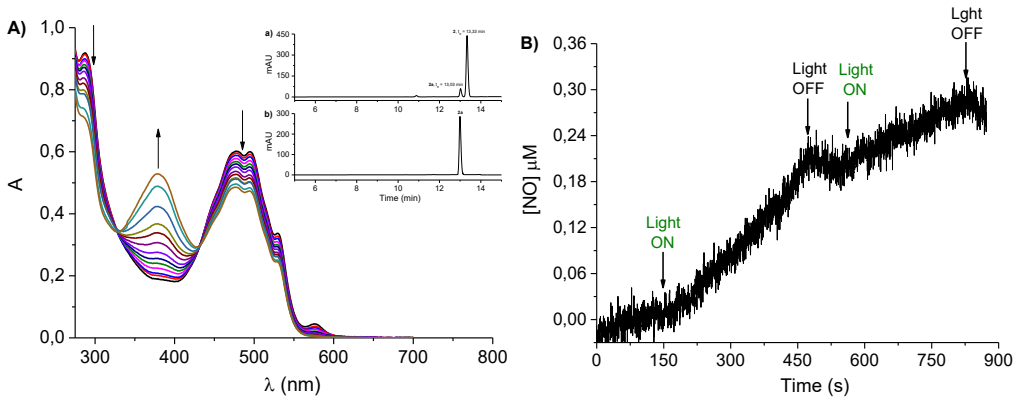

Figure 17. A) Absorption spectral changes observed upon exposure of a solution of **2** (48 µM) at λ_{exc} = 532 nm for different time intervals from 0 to 590 minutes in MeOH:H_2O (80:20 v/v). The arrows indicate the course of the spectral profile with the illumination time. HPLC trace related to a) a solution of **2** after 60 min of irradiation times with green light and b) the authentical non nitrosate derivative **2a**. B) NO release profile observed for a solution of **2** (48 µM) upon alternate cycles of green light (λ_{exc} = 532 nm) and dark.

The mechanism at the basis of the NO release is once again a photoinduced electron transfer but in this case it is mediated by a long-lived excited triplet state. The first proof of the involvement of the triplet state comes from the identical values of the Φ_f and τ found for **2** and free DOX, which exclude other deactivation process from the excited singlet state of **2** competitive with fluorescence. Moreover, irradiation of a solution of **2** under N_2-saturated conditions (spectra not reported) leads to the same absorption spectral changes observed in presence of oxygen (so the nature of the process is the same) but the photoreaction proceeds faster. The quenching of the photodecomposition observed in air-equilibrated solution represents another proof of the involvement of the triplet state. Another proof comes from the laser flash photolysis measurements. This technique is a powerful tool to obtain

information on the spectroscopic and kinetic behavior of transient species that absorb in the UV-Vis spectral region. Excitation of a solution of **2** results in a transient species with spectral features similar to those observed for DOX (see Figure 18A) and which can be attributable to the lowest excited triplet of the DOX [48], confirming the population of this state also in compound **2**. The triplet lifetime (τ_T) of **2** under anaerobic conditions was $\tau_T \approx 1.5$ µs while the triplet lifetime of free DOX under identical experimental conditions was $\tau_T \approx 5$ µs (see insets Figure 18A): this shorter triplet lifetime confirms the occurrence of an additional decay pathway (i.e. the intramolecular electron transfer) in compound **2**.

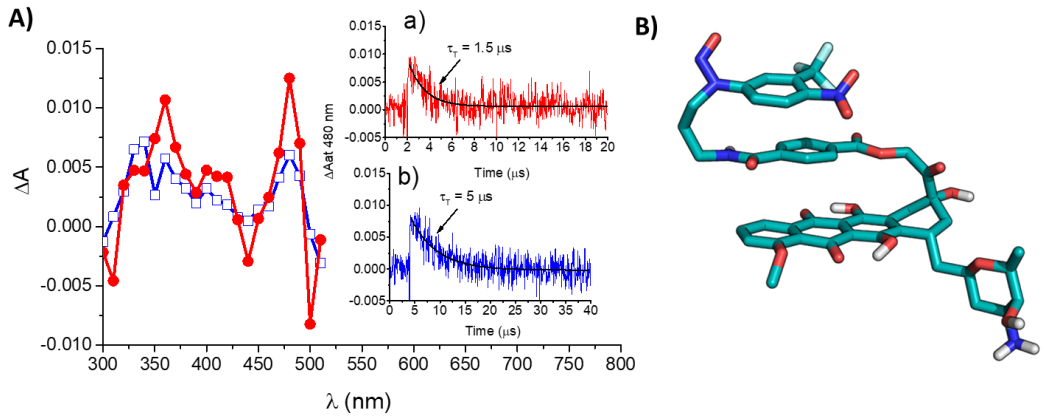

Figure 18. A) Transient absorption spectra observed 0.1 µs after 532 nm laser excitation (pulse with ≈ 6 ns, $E_{532} \approx 10$ mJ pulse^{-1}) of N_2-saturated solutions of **2** (●) and DOX (☐) (48 µM). The insets show the decay traces monitored at 480 nm and the related first-order fitting for a) **2** and b) DOX. MeOH: H_2O (80:20 v/v). B) Sandwich conformation assumed by the molecular hybrid **2** during molecular dynamics simulations.

This proposal is also well supported by the negative free energy value for the photoinduced triplet electron transfer processes $\Delta G \cong -0.2$ eV, estimated by the Rehm-Weller equation 4 [32]:

$$\Delta G = e[E_{ox} - E_{red}] - E_T \qquad (4)$$

where E_{ox} is the half-wave potential for one-electron oxidation of the electron-donor unit, ca. 1 eV vs. SCE [33], E_{red} is the half-wave potential for one-electron reduction of the electron-acceptor unit, ca. –0.6 1 eV vs. SCE [49] and E_T is the average energy of the lowest excited triplet states of the light harvesting centers, ca. 1,8 eV [48].

Such a photoinduced electron transfer is facilitated by the spatial proximity between the electron donor and the electron acceptor. Molecular dynamics simulation (see Figure 18B) shows the sandwich conformation adopted by **2** and stabilized by π-π interactions which allows the communication between the nitrosate ring, the benzoate moiety and the DOX chromophore.

3.2.4 Interaction with DNA

Interaction with DNA is at the basis of the anticancer activity of DOX. It intercalates into DNA base pairs and inhibits macromolecular biosynthesis [50]. DOX also inhibits the progression of topoisomerase II, an enzyme which relaxes supercoils in DNA for transcription. It stabilizes the complex enzyme-DNA after it has broken the DNA chain for replication, preventing the DNA double helix from being re-sealed and thereby stopping the process of replication [51].

The binding properties of **2** with ct-DNA and the preservation of its photochemical performances even after the binding with the biopolymer were explored. Figure 19A shows the absorption spectral changes registered for a solution of **2** in H_2O:DMSO (95:5 v/v) upon addition of increasing amount of ct-DNA; it shows a clear hypochromicity and the presence of an isosbestic point at ca 550 nm, suggesting the formation of a strong complex with DOX bound in a host environment with enhanced π-π stacking. The emission spectra reported in Figure 19B show a considerably quenching of the fluorescence; the fluorescent decay

present a dominant component τ of ≈ 1 ns during the whole titration (inset figure 19B). These results account for an intercalative binding mode of compound **2** and are in good agreement with what reported in literature for the free DOX [52].

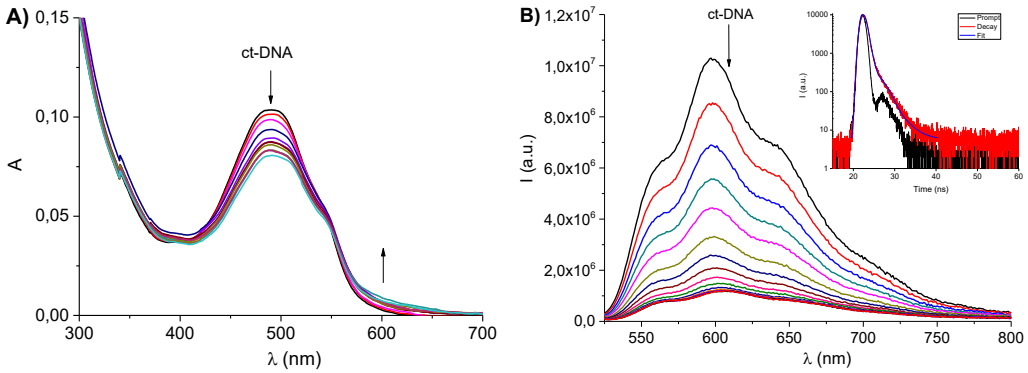

Figure 19. A) Absorption and B) fluorescence emission (λ_{exc} = 510 nm) spectral changes observed for a solution of **2** in H_2O:DMSO (95:5 v/v) upon addition of ct-DNA from 0 to 14.2 μM. The inset shows the fluorescence decay and the related fitting of the same solution of **2** recorded at λ_{exc} = 455 nm and λ_{em} = 600 nm.

3.2.5 Determination of the DNA binding parameters

The absorption and fluorescence spectra reported in Figure 19 allow to calculate the binding constant (K_b) and the number of binding sites (*n*) for each molecule of **2**. The half-reciprocal plot reported in figure 20A fitted fairly well the data of Figure 19A according to the equation 5:

$$[\text{ct-DNA}]_{bp}/(\varepsilon_A-\varepsilon_F) = [\text{ct-DNA}]_{bp}/(\varepsilon_B-\varepsilon_F) + 1/K_b(\varepsilon_B-\varepsilon_F) \qquad (5)$$

where $[\text{ct-DNA}]_{bp}$ is the concentration of the polynucleotide in base pairs, ε_A, ε_F, ε_B correspond to A_{obs}/[**2**], the extinction coefficient for the free **2** and the extinction coefficient for the totally bound form of **2**, respectively. By the ratio of the slope to intercept of the linear plot reported in Figure 20A a K_b of ≈ $3x10^5$ M^{-1} value was obtained. K_b is one order of magnitude larger than that reported for DOX for ct-

DNA, accounting for a significant cooperative effect of the N-nitrosoaniline appendage in the binding process.

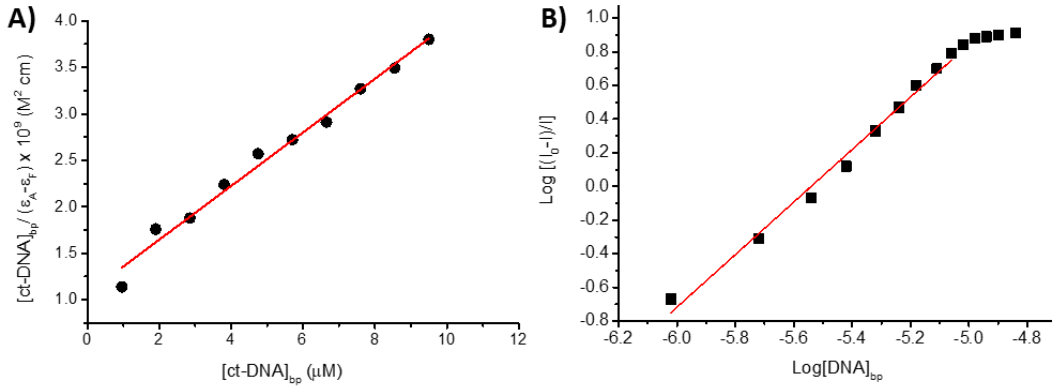

Figure 20. A) Half-reciprocal plot of binding of **2** with ct-DNA determined using the absorbance changes reported in Figure 19A at λ = 490 nm. B) Plot of $\log(I_0 - I)/I$ as a function of $\log[DNA]_{bp}$ obtained by using the fluorescence changes reported in Figure 19B at λ_{em} = 600 nm.

The fluorescence data were also useful to calculate the value of n which represent the number of binding sites for each molecule of **2**, by applying the equation 6:

$$\log [(I_0 - I)/I] = \log Kb + n\log[\text{ct-DNA}]_{bp} \qquad (6)$$

From the linear part of the plot in Figure20B, a value of *n* ≈ 1.5 was obtained. The value of *n* founded is a further indication of an intercalative binding mode, because groove binding would have led to much larger values of *n* [53].

3.2.6 Evaluation of the NO release after binding with DNA

Interestingly, the NO photoreleasing properties are maintained even after binding with the biopolymer. Figure 21A reports the absorption spectral changes observed upon irradiation of a solution of **2** in presence of DNA (20 μM); the photoreaction

was not completed (it was stopped at 20% of transformation) but the photolysis profile shows the appearance of the characteristic band of the nitroaniline moiety whose maximum of absorbance in this case is shifted of about 10 nm (400 nm) due to the solvent. NO release was also demonstrated through its direct and in real time detection using an ultrasensitive electrode which also demonstrate that the NO release is exclusively regulated by the green light (see Figure 21B).

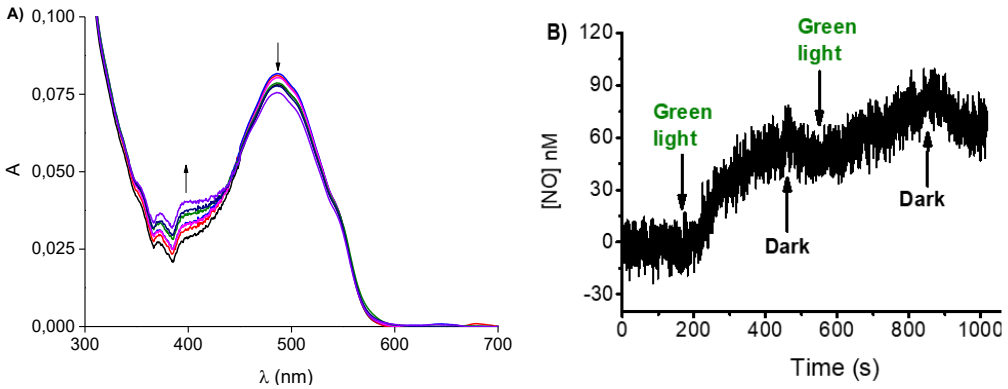

Figure 21. A) Absorption spectral changes observed upon exposure of an air-equilibrated solution of **2** (9.5 µM) in the presence of ct-DNA (20 µM) at λ_{exc} = 532 nm for different time intervals from 0 to 120 minutes. The arrows indicate the course of the spectral profile with the illumination time. H_2O:DMSO (95:5 v/v). B) NO release profile observed for a solution of **2** (9.5 µM) in the presence of ct-DNA (20 µM) upon alternate cycles of green light and dark.

In silico simulations (Figure 22) have revealed why NO release occurs even after intercalation of **2** into DNA: although the sandwich conformation of the free **2** is lost after DNA binding, the electron donor and the electron acceptor remain spatially close to allow NO release.

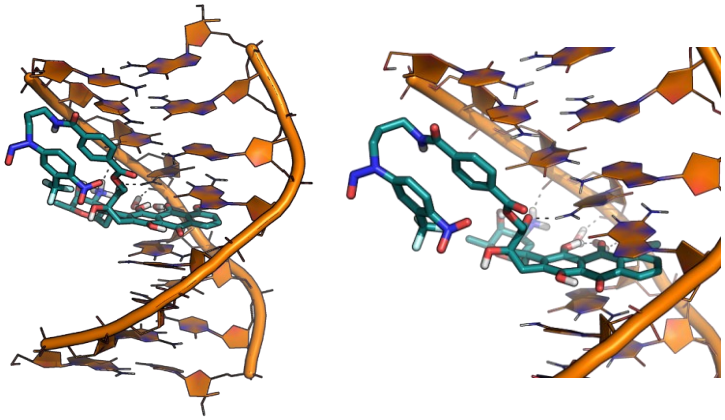

Figure 22. Possible orientation (left) and related zoom view (right) assumed by **2** when submitted to static docking and subsequent MD simulations in the presence of a DNA octamer. The DNA is shows as carton, **2** as capped sticks and hydrogen bonds as black dashed lines.

3.2.7 Biological activity. Toxicity and cell internalization

The photo-chemotherapeutic properties of compound **2** have been evaluated using two different breast cancer cell lines: adenocarcinoma MCF-7 and MDA-MB-231 triple negative breast cancer cells [54]. They have been categorized as MDR1-negative and MDR1-positive, respectively, on the bases of their expression of MDR1 pump evaluated by flow cytometry analyses and expressed as MDR Activity Factor (MAF). MCF-7 are MDR1-negative with a MAF approximately equals to zero. MDA-MB-231 is a highly aggressive and invasive form of breast cancer with limited treatment options. MDA-MB-231 are classified as MDR1-positive since they show over-expression of MDR1 pump and present a MAF of 54. Moreover, both cell lines can be considered positive for the expression of other two types of efflux pumps involved in MDR phenomena: MRP1/2 and BCRP, even if MDR1 pumps play the major role [55].

Dark cytotoxicity experiments showed that compound **2** does not induce any significative reduction of cell viability in both cancer cell lines while DOX is highly

cytotoxic only towards MCF-7 (IC_{50} = 7.6 µM) (Figure 23). These results are in good agreement with the MDR1 expression and allow to classify MCF-7 and MDA-MB-231 as DOX-sensitive and DOX-resistant cell lines, respectively.

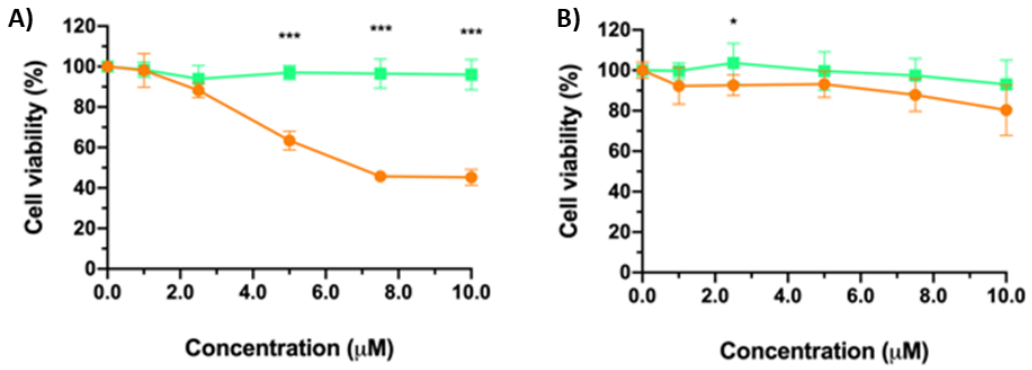

Figure 23. Decrease of cell viability in A) MCF-7 and B) MDA-MB-231 breast cancer cells after incubation for 2 h with increasing concentrations of compound **2** (green) or DOX (orange) and maintained in the dark. Data are expressed as mean percentage ± SD of at least three independent experiments, carried out in triplicate. *p<0.05; **p<0.01;***p<0.001 significantly different from DOX (Student's t Test).

In contrast, compound **2** shows a significant cytotoxic action towards both cancer cell lines under irradiation with green light (irradiation time 30 minutes, power density 40 mW/cm^2): IC_{50} is 3.9 µM for MDA-MB-231 and 0.46 µM for MCF-7. A photodynamic effect has also been observed for free DOX, although in a lesser extent than the hybrid and with a much more pronounced difference in the case of resistant MDA-MB-231 cells (Figure 24).

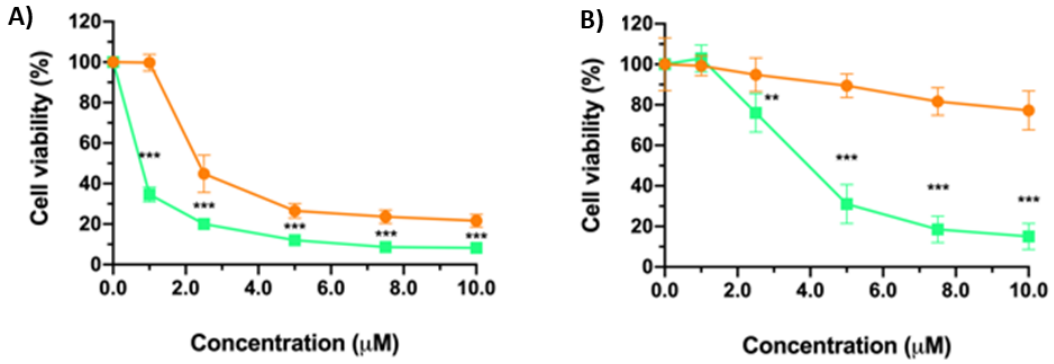

Figure 24. Decrease of viability in A) MCF-7 and B) MDA-MB-231 breast cancer cells after incubation for 2 h with increasing concentrations of compound **2** (green) or DOX (orange) and irradiated with green light. Data are expressed as mean percentage ± SD of at least three independent experiments, carried out in triplicate. **p<0.01; ***p<0.001 significantly different from DOX (Student's t Test).

In order to investigate the mechanism of action of compound **2**, it has been evaluated its cellular uptake by flow cytometry analysis after different incubation times, exploiting DOX fluorescence. The results reported in Figure 25A clearly shows that the cellular uptake of compound **2** is more than 5-fold higher than that observed with free DOX in both cancer cell lines.

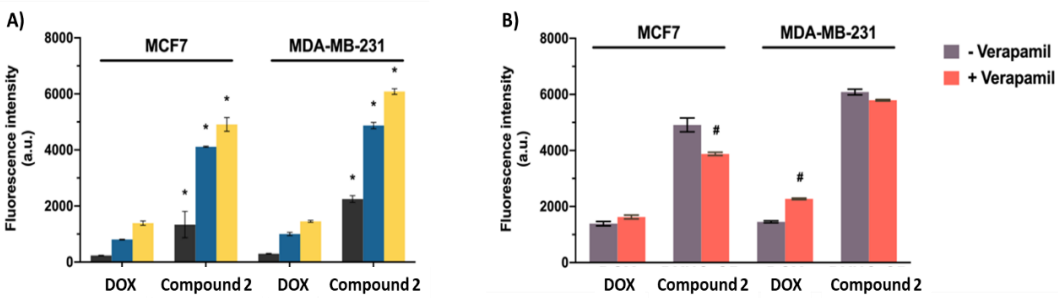

Figure 25. Cellular uptake of 2.5 μM DOX and compound **2** in MCF-7 and MDA-MB-231 cells measured by flow cytometry in A) the absence or in B) the presence of the MDR-1 inhibitor Verapamil (50 μM). Data are expressed as mean fluorescence intensity (a.u.) ± SD of at least three independent experiments, carried out in triplicate. *p<0.001 significantly different from DOX (Student's t-Test); #p<0.001 significantly different from -Verapamil (Student's t-Test).

The experiment has been repeated after treatment of both cell lines with Verapamil, a typical inhibitor of MDR1 efflux pump. Verapamil significantly increases the intracellular uptake of DOX only in MDA-MB-231 cells but doesn't affect the cellular uptake of compound **2** in both cancer cell lines (results reported in Figure 25B), demonstrating that compound **2** does not suffer of cell extrusion through a MDR1-mediated mechanism.

In view of these results and considering that compound **2** binds DNA with a binding constant higher than that reported for free DOX, the absence of dark toxicity by compound **2** is quite surprising and seems to suggest that the anticancer activity of the DOX has been lost after its covalent conjugation with the NOPD moiety. The intracellular localization of compound **2** has been evaluated using confocal fluorescence microscopy (Figure 26).

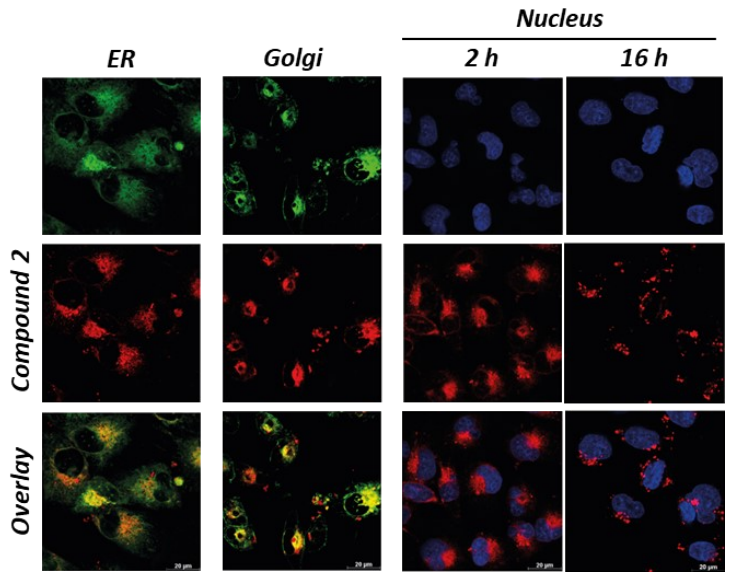

Figure 26. Intracellular localization of compound **2** in MDA-MB-231 cells after 2 h of incubation. Compound **2** fluorescence (red fluorescence) clearly co-localized with endoplasmic reticulum (ER-TrackerTM Green probe) and Golgi apparatus (BODIPY® FL C5-ceramide probe). Confocal microscopy images show the absence of co-localization between compound **2** (red fluorescence) and the nucleus (stained with Hoechst-33342).

The fluorescence images clearly show that after 2 h incubation compound **2** mainly localizes within the Golgi apparatus and within the endoplasmic reticulum. However, this behaviour is time dependent; in fact, for long incubation time (16 h) compound **2** localizes exclusively in the Golgi apparatus. In contrast, no localization has been observed within the nucleus (even after 16 h incubation), precluding any DNA intercalation and, as a consequence, explaining the lack of dark toxicity.

The fact that compound **2** does not suffer of cell extrusion through MDR1 efflux pumps is not sufficient to explain the higher cellular uptake of the hybrid with respect to DOX since it has been shown that its cellular uptake is higher also in the MDR1-negative MCF-7 cells. In fact, cellular uptake of drugs is a complex phenomenon which can be affected by different factors: chemical-physical properties of the drug, like ionization and lipophilicity, plasma membrane composition and drug efflux mechanisms.

The ionization degree is not expected to have an effect on the lipophilicity at physiological pH since compound **2** has a pK_a comparable with that of DOX (about 8.5). The experimental value of the partition coefficient between *n*-octanol and PBS at pH 7.4 has been calculated; the higher value founded for compound **2** with respect to DOX ($LogD_{7,4}$ of -0.04 for compound **2** against $LogD_{7,4}$ of -0.87 for DOX) justifies the high intracellular uptake of hybrid into both cell lines and is coherent with the evidence that the permeability of cells to the anthracyclines is mediated via the lipid domain of the plasma membrane as shown for DOX [56].

To explore the mechanisms of compound **2** internalization, it is important to understand if the uptake occurs only through passive diffusion throughout plasma membranes or if it is an energy-dependent mechanism mediated by cells. For this purpose, the cellular uptake of compound **2** has been evaluated at 4 °C (data not shown). The data show that the accumulation of compound **2** and DOX in both cell

lines was largely reduced at such low temperature, suggesting that it's an energy-dependent mechanisms other than simple diffusion through plasma membranes.

3.2.8 Interaction with bovine serum albumin and determination of binding constant

Serum albumins are a long-circulating and highly abundant proteins in the blood; they are natural carriers of native ligands and other hydrophobic compounds [57] and they have been studied as carriers for many anti-cancer agents since they are able to prolong the circulation half-life of otherwise rapidly cleared drugs and, importantly, promote their accumulation within tumors [58]. Since albumin is present in the culture medium as the prevailing serum component (in the experiments here reported serum accounts for the 10% of the culture medium), it must be considered that the internalization of compound **2** and its cytotoxic effect can be influenced by this group of proteins.

The capability of compound **2** to bind serum albumin has been evaluated using steady-state and time resolved fluorescence techniques. It has been used bovine serum albumin (BSA) which is the most studied protein of the serum albumin group due to its structural homology with human serum albumin (HSA). BSA has two tryptophan residues that possess intrinsic fluorescence [59]; when BSA is excited at 280 nm, it shows a strong fluorescence emission with a maximum at 347 nm. The analysis of the fluorescence of BSA in the presence of increasing amounts of drug represent the most appropriate method to study the binding affinities of the protein with a specific guest.

Upon addition of increasing amount of compound **2**, it has been observed a decrease of the fluorescence intensity and a slight red shift of the fluorescence maximum (see Figure 27A). The quenching of the fluorescence well accounts for an

interaction between the protein and the hybrid; moreover, the slight red shift observed reveals that tryptophan residue was brought to a more hydrophilic environment due to the BSA/compound **2** interaction.

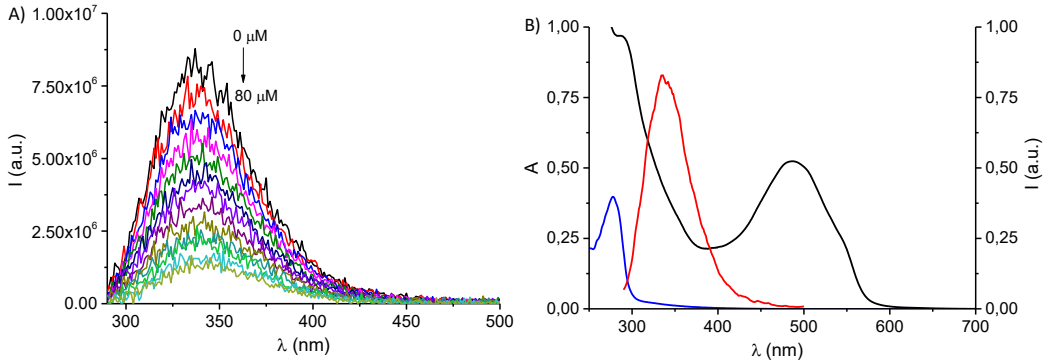

Figure 27. A) Fluorescence emission spectra (λ_{exc} = 280 nm) of BSA (10 µM) observed upon addition of increasing amount of compound **2** from 0 to 80 µM. B) Normalized absorption spectra of BSA (blue line) and compound **2** (black line) and the fluorescence emission spectrum of BSA (red line). T = 25 °C, pH 7.4.

Figure 27B clearly shows the overlap between the emission spectrum of BSA and the absorption spectrum of compound **2**; in order to avoid a trivial fluorescence quenching arising from inner filter effect due to competitive absorption of the excitation light and re-absorption of the emitted light, all the emission spectra have been corrected according to the equation 7 [60]:

$$F_c = F_m \, e^{(A_1 + A_2)/2} \qquad (7)$$

where F_c and F_m are the corrected and measured fluorescence, respectively, and A_1 and A_2 are the absorbance of compound **2** at excitation wavelength and emission wavelength, respectively.

In order to determine the type of quenching mechanism, if static or dynamic, it has been plotted the fluorescence data according to the Stern-Volmer equation 8 [61]:

$$\frac{F_0}{F} = 1 + K_{SV}[\mathbf{2}] \quad (8)$$

where F_0 and F are the fluorescence intensities in the absence and presence of compound **2**, respectively; [**2**] is the concentration of the hybrid; K_{sv} is the Stern–Volmer quenching constant. From the linear part of the plot reported in Figure 28 it has been obtained a value for K_{SV} equal to 1.95×10^4 M^{-1}.

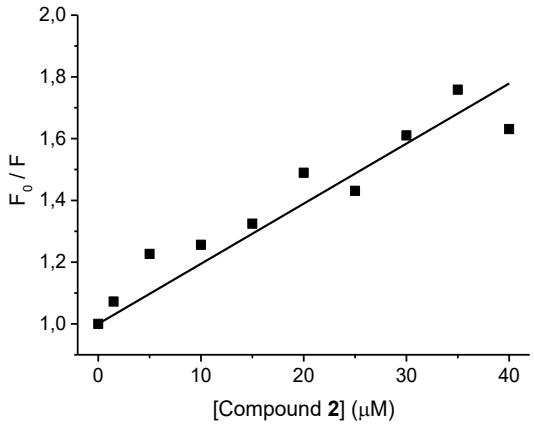

Figure 28. Stern Volmer plot of fluorescence quenching constant (K_q) for the compound **2**/BSA complex at different concentration of compound **2**. All the data has been corrected by equation 7.

There is a correlation between the K_{SV} and the quenching constant k_q represented by equation 9:

$$K_{SV} = k_q t_0 \quad (9)$$

where k_q is the bimolecular quenching constant and t_0 is the average lifetime of the fluorophore in absence of compound **2** and its value is 5.9 ns. k_q results to be 3.3×10^{12} M^{-1} s^{-1}. This value exceeds by more than two order of magnitude the

diffusional rate constant, suggesting that the quenching process takes place exclusively through a static mechanism according to the formation of a non-fluorescent BSA/compound **2** complex.

The binding constant, K_b and the fraction of fluorophore accessible to quencher, f, where obtained by the modified Stern-Volmer equation 10 [61, 62]:

$$F_0/(F_0 - F) = 1/(fK[\mathbf{2}]) + 1/f \qquad (10)$$

The plot of $F_0/(F_0–F)$ vs $1/[\mathbf{2}]$ (see Figure 29A) yields f^{-1} as the intercept on y axis and $(f \cdot K)^{-1}$ as the slope. It has been obtained an f value of 0.5 ± 0.05 and a K_b value of $1.05 \cdot 10^5$ M^{-1}; the K_b value is more than one order of magnitude larger than that reported for free DOX under the same experimental conditions (K_b reported in literature for free DOX is 7.8 (±0.7) x 10^3 M^{-1}) [63].

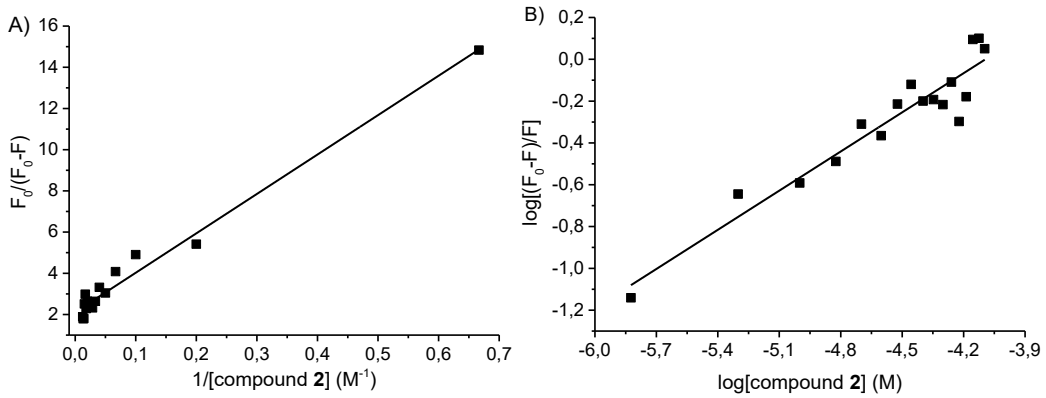

Figure 29. Plots of the data of Figure 27, corrected by equation 7, according to equation 10 (plot A) and 11 (plot B).

The number n of molecules bound/BSA molecule has been calculated according to equation 11 [64]:

$$\log[(F_0 - F)/F] = \log K_A + n \log[\mathbf{2}] \qquad (11)$$

A value of 0.62 ± 0.05 has been obtained by the linear plot of log[(F_0–F)/F] as a function of log[**2**] which is shown in Figure 29B.

All these results clearly show that BSA is able to bind compound **2** and suggest that it can play a key role as carrier in the cellular internalization.

3.2.9 Photochemical characterization of complex with BSA and NO release

In view of this effective binding, it is important to verify if the photophysical and photochemical properties of compound **2** have been preserved even after the interaction with the protein.

The fluorescence decay of compound **2** in presence of BSA exhibits a bi-exponential behaviour with lifetimes τ_1= 0.82 ns (relative amplitude A_1: 76%) and τ_2 = 1.97 ns (A_2: 24%) (see figure 30A). These values are similar to that observed in absence of BSA (in the same solvent τ_1= 1.01 ns and τ_2 = 2.40 ns with A_1: 85% and A_2 15%, respectively) and clearly suggest that the excited singlet state of compound **2** is only slightly influenced by binding with BSA.

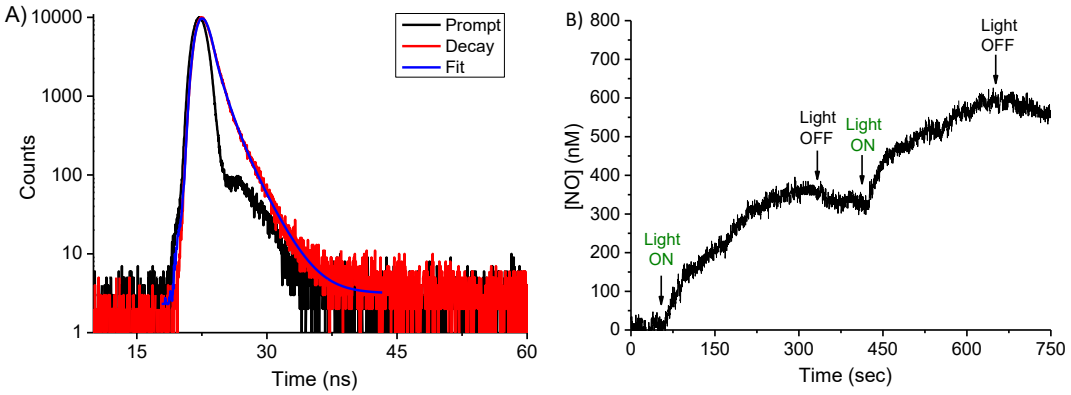

Figure 30. A) Fluorescence decay and the related fitting of the compound **2** recorded at λ_{exc} = 455 nm and λ_{em} = 600 nm. B) NO release profile observed for a solution of compound **2** in the presence of BSA upon alternate cycles of green light (λ_{exc} = 532 nm) and dark. [BSA] = 10 mM; [compound **2**] = 80 µM. T = 25 °C, pH 7.4.

The NO photo-release capability of compound **2** has been investigated through an amperometric technique using an ultrasensitive electrode. The amperogram (Figure 30B) shows that the capability to release NO is well preserved even after binding with BSA and is controlled by green light; in fact, it starts upon excitation with green light and stops in the dark. This result clearly suggests that also the lowest excited triplet state is not affected by binding with protein.

3.2.10 Intracellular photogeneration of NO

The light-controlled generation of NO inside cellular environment has also been measured by flow cytometry using the probe DAF-FM. This latter is a highly sensitive and non-fluorescent probe which is used for quantification of low concentrations of NO; in fact, after reaction with NO, it becomes fluorescent due to the formation of a benzotriazole derivative. The results obtained after incubation of MDA-MB-231 cells with compound **2** and irradiated or maintained in the dark are reported in Figure 31A. In the dark, no significant increase of the cellular NO level has been observed; in contrast, a remarkable increase of cellular NO level has been observed in cells exposed to green light. In fact, DAF-FM fluorescence displays a two-fold increase with respect to that observed with cells maintained in the dark. When cells have been incubated with DOX, a slightly increase of the DAF-FM fluorescence has been observed only in cells exposed to light; this result can be explained with an upregulation of iNOS [46].

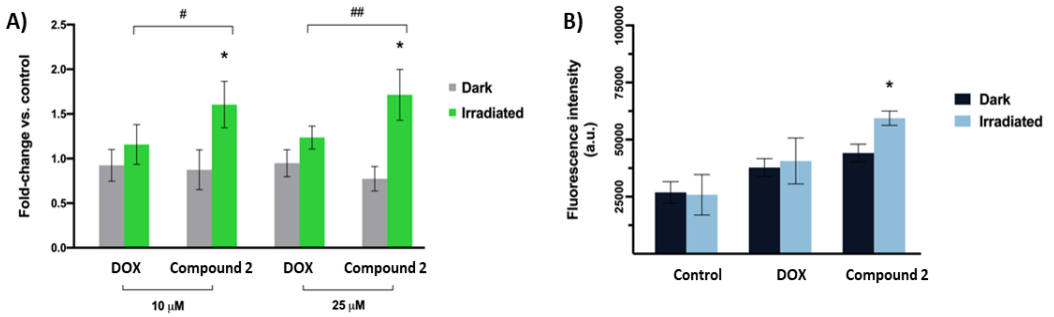

Figure 31. A) Detection of the intracellular levels of NO generated by compound **2** or DOX in the absence or in the presence of green light irradiation. NO increment is expressed as increase of DAF-FM probe fluorescence with respect to the fluorescence signal measured in control cells and set equal to 1. *p<0.001 significantly different from dark sample (Student's t-Test). #p<0.01; ##p<0.001 significant difference between dark and light (Student's t-Test). B) Inhibition of MDR efflux pumps measured through the retention of the substrate EFLUXX-ID. *p<0.001 significantly different from dark sample (Student's t Test).

As already explained before, NO has also an inhibitory effect on the efflux pumps mainly responsible of MDR [65]. In order to evaluate if this effect has been reached, it has been evaluated the intracellular accumulation of an MDR-pump substrate, EFLUXX-ID. It is a hydrophobic non-fluorescent compound that readily penetrates the cell membrane; once inside of the cells, it is hydrolyzed by intracellular esterases leading to the formation of fluorescent products. The fluorescence signal generated within the cells depends upon the activity of the ABC transporters: cells with highly active transporters will demonstrate lower fluorescence due to the active efflux of the probe from the cell. The results reported in Figure 31B clearly show an increased intracellular accumulation of the probe in cells incubated with compound **2** and irradiated with green light, proving the direct inhibition of pumps upon the activity of the photo-released NO.

3.2.11 Conclusion

A novel NOPD which combines the well-known chemotherapeutic DOX and a derivative of the N-nitrosoaniline has been developed. Photoexcitation of DOX with the green light triggers the NO detachment from the N-nitroso appendage via a triplet-state mediated intramolecular electron transfer without precluding the red emission of DOX, useful for cellular tracking of the hybrid. Moreover, the novel NOPD binds DNA with a binding constant higher than that reported for free DOX and it maintains the capability to release NO even after binding with DNA. The biological activity of the hybrid has been evaluated against two different breast cancer cell lines. The hybrid does not suffer cell extrusion by MDR-pumps and shows a cellular internalization higher than that of free DOX. However, it does not show any cytotoxic activity in the dark against neither of the two cancer cell lines used but induces remarkable cell death under activation with green light. This lack of dark toxicity is due to the cellular localization of the hybrid; differently to DOX, it does not localize within the nucleus but is confined in the Golgi apparatus and endoplasmic reticulum and consequently, it does not act as DNA intercalator. The higher cellular internalization is mediated by the BSA; the hybrid bounds BSA with a binding constant which is more than one order of magnitude larger than that reported for free DOX. In addition, protein binding does not affect the NO photo-releasing properties of the hybrid, which releases NO under green light even after binding with BSA and at intracellular level.

3.3 A Generator of Peroxynitrite Activatable with Red Light

3.3.1 Design

NO is not the only useful RNS with photo-chemotherapeutic applications. Peroxynitrite ($ONOO^-$) is another RNS that plays a dominant role in biology and chemistry. It is the product of the diffusion-controlled reaction between NO and the superoxide anion ($O_2^{\bullet-}$) ($k \sim 10^{10}\ M^{-1}\ s^{-1}$) [66]. $ONOO^-$ is labelled as a strong cytotoxic agent due to its double capability to act as a nucleophile and generator of very reactive secondary free radical species [67]. It is studied as unconventional therapeutic agent since it presents the same advantages mentioned for NO, like the absence of MDR and the capability to react with biological substrate of different nature. However, this lack of selectivity for bio-substrates requires a precise spatiotemporal control in its delivery. Also in this case, this purpose can be reached with the light. However, there are only few examples of $ONOO^-$ generators activatable with a biocompatible light reported in literature. The design of photoactivatable generators of $ONOO^-$ is not simple. As just said, $ONOO^-$ is the product of a very fast reaction between NO and $O_2^{\bullet-}$ and these two species need to be simultaneously generated under light stimulus from appropriate chromogenic units.

A novel photoactivatable construct activatable with the red light has been developed. It combines an N-nitrosoaniline derivative as NO-donor moiety with the benzophenothiazine moiety which acts as red-light harvesting antenna and as generator of superoxide anion ($O_2^{-\bullet}$) (Figure 32) [68].

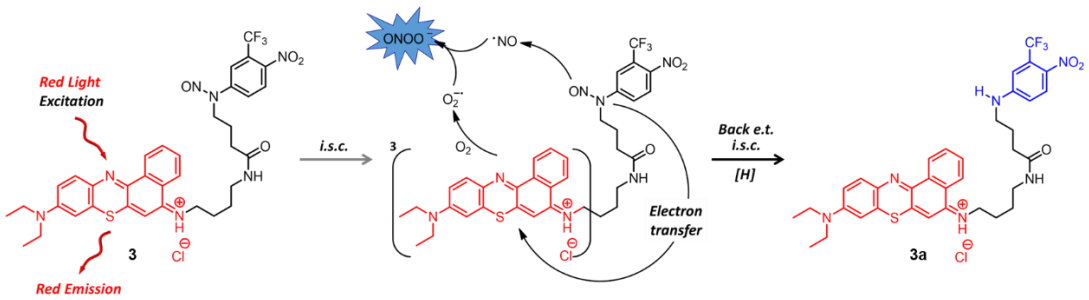

Figure 32. Structure of hybrid **3** and proposed mechanism leading to the generation of $ONOO^-$ and the formation of the photoproduct **3a**.

The design of the molecular hybrid has been done taking into account two different findings:

i) the first one regards the AO and DOX based NOPDs already presented in this work [28, 47] and which release NO under visible light activation due to an intramolecular photoinduced electron transfer;

ii) the second one regards the phenothiazine-based systems developed by *Peng et al*. which are able to generate $O_2^{\bullet-}$ under red light excitation due to an intermolecular photoinduced electron transfer involving the lowest triplet state of the red-absorbing chromophore and the molecular oxygen [69].

The combination of these two moieties leads to the generation of the construct **3** that, under red light excitation, releases NO and $O_2^{\bullet-}$ through the two above descripted mechanism and produces the non-nitrosated derivative **3a** as the main stable photoproduct. The reaction between the two active species (NO and $O_2^{-\bullet}$) leads to the generation of $ONOO^-$, making this construct one of the few organic generators of $ONOO^-$ activatable with red light. The hybrid also offers the additional advantage of red fluorescence emission, a useful tool for its cellular tracking.

3.3.2 Synthesis

The designed compound **3** and its main stable photoproduct **3a** have been synthesized following the procedure reported below. All syntheses were carried out under a low intensity level of visible light.

The direct coupling of commercial ethyl 4-aminobutyrate hydrochloride **3b** with 5-fluoro-2-nitrobenzotrifluoride in acetonitrile at room temperature gave rise to **3c**, which, in turn, yielded the acid NOPD **3d** when treated with sodium hydroxide in dioxane. The nitroso NOPD **3e** was obtained through nitrosation of **3d** with $NaNO_2$ and CH_3COOH (Scheme 3).

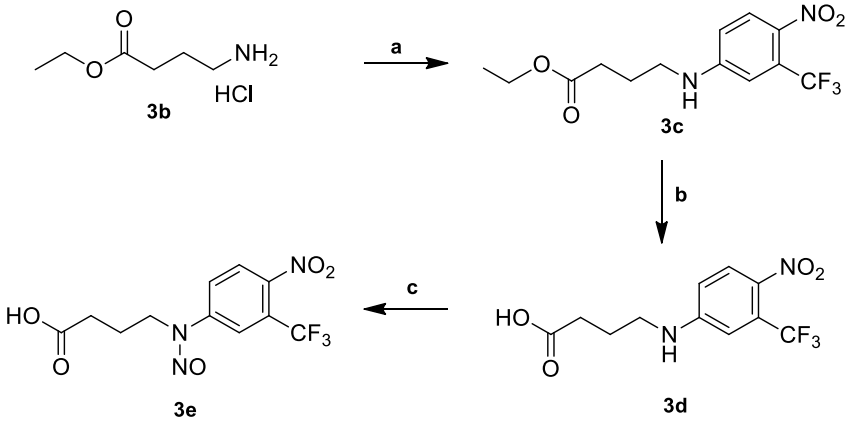

Scheme 3. Synthesis of nitroaniline acid derivative **3d** and **3e**. a) 5-fluoro-2-nitrobenzotrifluoride, K_2CO_3, CH_3CN, r.t. 79%; b) NaOH, dioxane, r.t. 95%; c) $NaNO_2$, CH_3COOH:THF 1:1, r.t. 86%.

The benzophenothiazine scaffold **3h** was synthesized according to literature [70] through reaction between the Bunte salt, an S-arylthiosulfate which in turn has been prepared following the literature [70], with the naphthyl derivative **3g** in the presence of $K_2Cr_2O_7$ in DMSO and MeOH with the addition of HCl 2 M. The benzophenothiazine ring was directly synthesized with the side chain acting as a

spacer and then bound with the nitrosated or non-nitrosated nitro-derivative appendage. The naphthyl derivative **3g** is the product of the reaction between 1-bromonaphthalene **3f** with butane-1,4-diamine in 2-methoxyethanol solution at reflux. The reaction of **3h** with compound **3d** in presence of EDC·HCl as coupling agent, HOBt and DMAP in dry DMF gave the reference compound **3a**. The nitrosated compound **3** was obtained in analogous way from compound **3e** (Scheme 4).

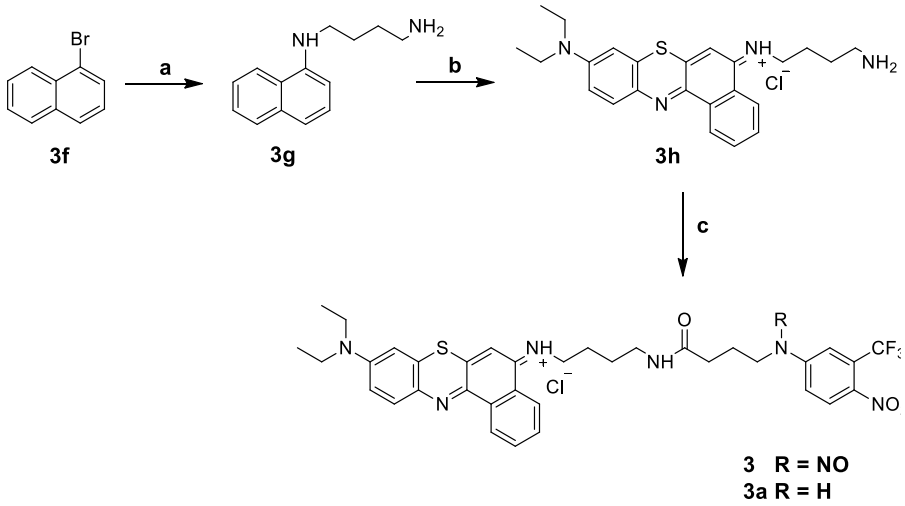

Scheme 4. Synthesis of compound **3** and its main stable photoproduct **3a**. a) butane-1,4-diamine, CuI, $CsCO_3$, 2-methoxyethanol, reflux, 33%; b) Bunte salt, $K_2Cr_2O_7$, DMSO, CH_3OH, HCl, r.t. 23%; c) **3d** or **3e**, EDC·HCl, HOBt, DMAP, DMF dry, r.t., 16%.

Ethyl 4-((4-nitro-3-trifluoromethylphenyl)amino)butanoate (3c).

A solution of ethyl 4-aminobutyrate hydrochloride (**3b**, 2 g, 12 mmol) and 5-fluoro-2-nitrobenzotrifluoride (1.3 g, 6 mmol) in CH_3CN (50 mL) was stirred at room temperature in the presence of K_2CO_3 (3.4 g, 12 mmol). The reaction mixture was stirred for 72 h and the solvent removed under reduced pressure. The residue was dissolved in EtOAc (20 mL) and washed with water (3 × 25 mL), dried over Na_2SO_4 and concentrated to dryness to give a yellow compound that was treated with

petroleum ether (PE), filtered and the filtrate concentrated to dryness to give the target compound as a yellow solid (1.5 g, 79%). ^{1}H NMR (600 MHz, $CDCl_3$) δ 8.01 (m, 1H), 6.87 (bs, 1H), 6.66 (dd, J = 9.1, 2.6 Hz, 1H), 4.16 (q, J = 7.1 Hz, 2H), 3.30 (m, 2H), 2.47 (t, J = 6.6 Hz, 2H), 2.00 (q, J = 6.6 Hz, 2H), 1.27 (t, J = 6.6 Hz, 3H). ^{13}C NMR (150 MHz, $CDCl_3$) δ 173.53, 151.78, 136.50, 129.32, 126.66 (q, $^{2}J_F$ = 33 Hz), 122.22 (q, $^{1}J_F$ = 271.5 Hz), 112.78, 111.16, 60.90, 43.17, 31.93, 23.88, 14.22. ESI-MS $[M+H]^+$: m/z 321.3.

4-((4-Nitro-3-trifluoromethylphenyl)amino)butanoic acid (3d).

To a solution of **3c** (1.5 g, 4.67 mmol) in 1,4-dioxane (10 mL), NaOH 1 M (23 mL) was added, and the resultant mixture was stirred at room temperature for 5 h. The reaction mixture was acidified to pH 3 with 7% sulphuric acid and the product was extracted with EtOAc (20 mL). The organic phase was dried over Na_2SO_4 and concentrated to dryness to obtain the target compound as a yellow solid (1.29 g, 95%). ^{1}H NMR (600 MHz, CD_3OD) δ 8.02 (d, J = 9 Hz, 1H), 7.00 (s, 1H), 6.80 (dd, J = 9.1, 2.5 Hz, 1H), 3.27 (t, J = 7.2 Hz, 2H), 2.43 (t, J = 7.2 Hz, 2H), 1.93 (quint, J = 7.2 Hz, 2H). ^{13}C NMR (150 MHz, CD_3OD) δ 175.79, 153.53, 134.9, 129.05, 125.96 (q, $^{2}J_F$ 34.5 Hz), 122.7 (q, $^{1}J_F$ = 270 Hz), 117.20, 110.82, 42.02, 30.49, 23.99. ESI-MS $[M-H]^-$: m/z 291.2.

N-Nitroso-4-((4-nitro-3-trifluoromethylphenyl)amino)butanoic acid (3e).

To a solution of **3d** (685 mg, 2.34 mmol) in a mixture THF:CH_3COOH (1:1 v/v; 22 mL) cooled at 0 °C with an ice bath, sodium nitrite (65 mg, 9.37 mmol) was added; the reaction mixture was stirred at 0 °C for 1 h. When the reaction was completed (TLC), the obtained mixture was diluted with EtOAc (20 mL) and washed with water (3 × 20 mL), dried over Na_2SO_4 and concentrated to dryness to obtain the target

compound as a dark yellow solid (644 mg, 86%). ^{1}H NMR (600 MHz, CD_3OD) δ 8.30 (s, 1H), 8.19 (d, J = 9 Hz, 1H), 8.15 (d, J = 9 Hz, 1H), 4.16 (t, J = 9 Hz, 2H), 2.34 (t, J = 7.2 Hz, 2H), 1.78 (quint, J = 7.8 Hz, 2H). ^{13}C NMR (150 MHz, CD_3OD) δ 176.25, 146.72, 146.42, 128.53, 125.93 (q, $^{2}J_F$ 34.5 Hz), 123.32 (q, $^{1}J_F$ = 271.35 Hz), 122.66, 118.13, 42.81, 31.20, 22.24. ESI-MS $[M-H]^-$: m/z 320.3.

N^1-(naphthalen-1-yl)butane-1,4-diamine (3g).

To a solution of 1-bromonaphthalene (**3f**, 2 g, 9.7 mmol) and butane-1,4-diamine (4.87 mL g, 48.5 mmol) in 2-methoxyethanol (20 mL), CuI (92 mg, 0.49 mmol) and Cs_2CO_3 (2.5 g, 7.6 mmol) were added, and the mixture was refluxed at 125 °C for 24 h. After completion of the reaction (TLC), the mixture was allowed to reach room temperature and filtered off to yield a pale brown solution. The filtrate was diluted with EtOAc (100 mL) and washed with saturated sodium chloride solution (3 × 20 mL), dried over Na_2SO_4 and concentrated to dryness. The crude product was purified by silica gel column chromatography with CH_2Cl_2:MeOH (NH_3 sat) (95:5 v/v) and gets the desired dark orange oil product (660 mg, 33%). ^{1}H NMR (600 MHz, $CDCl_3$) δ 7.79 (d, J = 8.4 Hz, 2H), 7.47 – 7.34 (m, 3H), 7.25 (m, 1H), 6.54 (m, 1H), 4.57 (bs, 1H), 3.06 (bs, 2H), 2.57 (bs, 2H), 1.55 (bs, 2H), 1.39 (bs, 4H).^{13}C NMR (150 MHz, $CDCl_3$) δ 143.04, 133.63, 127.82, 126.07, 125.10, 123.82, 122.69, 119.53, 116.03, 103.42, 43.14, 41.08, 30.45, 25.84. ESI-MS $[M+H]^+$: m/z 215.2.

(Z)-4-Amino-N-(9-(diethylamino)-5H-benzo[a]phenothiazin-5-ylidene)butan-1-aminium chloride (3h).

To a solution of Bunte salt (605 mg, 2.19 mmol) and **3g** (670 mg, 3.13 mmol) in DMSO (12 mL), potassium dichromate (757 mg, 2.57 mmol) was added. The mixture was stirred at room temperature for 20 min, then methanol (120 mL) and HCl 2M

(12 mL) were added. The resulting mixture was stirred for further 40 min at r.t., and the reaction progress was monitored by TLC. When the reaction was complete, methanol and water were removed under reduced pressure, and the remaining solution was slowly poured into a saturated sodium chloride solution (60 ml). The blue precipitate was filtered, collected and dried. The crude product was purified by silica gel column chromatography using CH_2Cl_2:MeOH (NH_3 sat) (90:10 to 80:20 v/v) as the eluent. The target compound was obtained as a dark blue solid (223 mg, 23%). ^{1}H NMR (600 MHz, CD_3OD) δ 8.20 (d, J = 7.8 Hz, 1H), 7.98 (d, J = 7.8 Hz, 1H), 7.44 (m, 2H), 7.30 (d, J = 9.2 Hz, 1H), 6.97 (dd, J = 9.3, 2.2 Hz, 1H), 6.73 – 6.67 (m, 2H), 3.49 (q, J = 7.0 Hz, 4H), 3.36 (t, J = 6.7 Hz, 2H), 3.02 (t, J = 7.0 Hz, 2H), 1.85 – 1.76 (m, 4H), 1.23 (t, J = 7.2 Hz, 6H). ^{13}C NMR (150 MHz, CD_3OD) δ 153.68, 152.27, 140.52, 138.07, 134.35, 133.99, 133.56, 132.84, 131.84, 130.40, 125.80, 124.96, 123.70, 118.47, 105.89, 103.00, 46.91, 44.80, 40.40, 26.77, 26.15, 13.34. ESI-MS $[M+H]^+$: m/z 405.6.

General procedure for the synthesis of compound 3 and 3a.

Under N_2 atmosphere, a mixture of **3h** (1 mmol), **3d** or **3e** (2 mmol), EDCl (1.95 mmol), HOBt (2.25 mmol), and DMAP (1.95 mmol) were dissolved in dry DMF (50 mL), and the mixture was stirred at r.t. for 24 h. After the reaction was complete, the resulting solution was diluted with saturated sodium chloride solution (50 mL) and extracted with EtOAc (3 × 20 mL), dried over Na_2SO_4 and concentrated to dryness. Purification of the residue by silica gel column chromatography using CH_2Cl_2:MeOH (95:5 to 90:10 v/v) as the eluent, gave the target compounds. All operations were carried out under a low intensity level of visible light.

(Z)-N-(9-(diethylamino)-5H-benzo[a]phenothiazin-5-ylidene)-4-(4-((4-nitro-3-(trifluoromethyl)phenyl)amino)butanamido)butan-1-aminium chloride (3a). Yield

16%, blue/green solid. Purity: 100%. This compound exists as a mixture of rotamers in a 72:28 ratio as determined by ^{1}H NMR. ^{1}H NMR (600 MHz, CDCl3) δ 8.94 (d, J = 8.1 Hz, 1H), 8.81 (d, J = 8.2 Hz, 1H), 8.25 and 8.16 (bs, 1H), 7.92 (d, J = 9.4 Hz, 1H), 7.81 – 7.71 (m, 2H), 7.68 (m, 2H), 7.10 (dd, J = 9.4, 2.7 Hz, 1H), 7.03 (s, 1H), 6.88 (bs, 1H), 6.94 (bs, 1H), 6.83 (d, J = 2.6 Hz, 1H), 6.59 (d, J = 10.0 Hz, 1H), 3.69 (bs, 2H), 3.59 (q, J = 7.2 Hz, 4H), 3.32 and 3.27 (m, 2H), 3.14 and 3.04 (m, 2H), 2.45 and 2.39 (t, J = 7.0 Hz, 2H), 2.00 – 1.87 (m, 4H), 1.70 and 1.54 (m, 2H), 1.34 (t, J = 7.2 Hz, 6H). ^{13}C NMR (150 MHz, $CDCl_3$) δ 174.10, 154.11, 152.61, 150.66, 140.34, 137.24, 135.17 and 134.83, 133.53, 132.48, 131.40, 130.95, 130.18, 129.18 and 129.05, 126.29 (q, $^{2}J_F$ = 27.2 Hz), 125.68, 125.23, 124.58, 123.99, 122.43 (q, $^{1}J_F$ = 271.5 Hz) 117.48, 116.37, 111.00, 104.31, 102.38, 45.67, 44.37, 42.88 and 42.16, 39.21 and 38.69, 33.82 and 33.74, 26.77 and 26.21, 26.06 and 25.78, 24.63 and 24.17, 12.66. ESI-MS $[M+H]^+$: m/z 679.8.

(Z)-4-(4-(((3-Trifluorometil-4-nitro)phenyl)(nitroso)amino)butanamido)-N-(9-(diethylamino)-5H-benzo[a]phenothiazin-5-ylidene)butan-1-aminium chloride (3). Yield 16%, dark blue solid. Purity: 97%. ^{1}H NMR (600 MHz, $CDCl_3$) δ 8.99 (dd, J = 6.0, 3.2 Hz, 1H), 8.81 (dd, J = 6.2, 3.4 Hz, 1H), 8.26 (d, J = 1.8 Hz, 1H), 8.22 (t, J = 5.3 Hz, 1H), 8.05 – 7.97 (m, 3H), 7.84 (d, J = 9.4 Hz, 1H), 7.66 (m, 2H), 7.08 (dd, J = 9.4, 2.7 Hz, 1H), 7.01 (s, 1H), 6.81 (d, J = 2.7 Hz, 1H), 4.04 (m, 2H), 3.74 (t, J = 7.0 Hz, 2H), 3.58 (q, J = 7.2 Hz, 4H), 3.33 (dd, J = 11.8, 5.7 Hz, 2H), 2.45 (t, J = 6.7 Hz, 2H), 2.01 (m, 2H), 1.77 (m, 4H), 1.32 (t, J = 7.2 Hz, 6H). ^{13}C NMR (150 MHz, $CDCl_3$) δ 172.61, 154.33, 150.64, 145.05, 144.95, 140.27, 137.16, 135.25, 133.48, 132.29, 131.40, 130.70, 130.30, 127.58, 125.41 (q, $^{2}J_F$ = 34.4 Hz), 125.13, 124.91, 124.80, 121.75 (q, $^{1}J_F$ = 273 Hz), 120.65, 116.56, 116.27, 104.50, 102.75, 45.78, 44.42, 42.31, 38.58, 32.56, 26.18, 25.88, 21.91, 12.82. ESI-MS $[M+H]^+$: m/z 708.6.

3.3.3 Photochemical characterization and NO release

Figure 33A displays the absorption spectrum of compound **3** and compound **3a** in phosphate buffer (PB):MeOH (1:1 v/v), where the two compounds are well soluble. Both the spectra are dominated by a main absorption band in the visible region, with a maximum at 670 nm extending in the whole red region and an absorption band in the UV region with a maximum at about 310 nm. The spectrum of compound **3a** presents an absorption band at 390 nm arising from the push-pull character of the nitroaniline moiety and which is suppressed in compound **3** due to the electron-withdrawing NO group attached at the amino functionality.

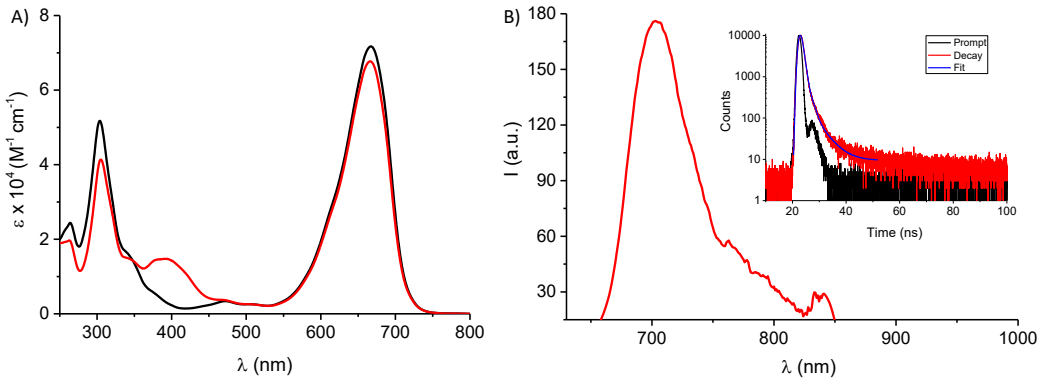

Figure 33. A) Absorption spectra of a solution of compound **3** (black line) and **3a** (red line) at the same concentration (18 μM). B) Fluorescence emission (λ_{exc} = 620 nm) spectrum of a solution of compound **3**. The inset shows the fluorescence decay and the related fitting of the same solution recorded at λ_{exc} = 455 nm and λ_{em} = 710 nm. PB:MeOH (1:1 v/v), T = 25 °C.

The fluorescence emission spectrum (see figure 33B) displays the typical band of the benzophenothiazine moiety with a maximum at 700 nm extending up to the near infrared region. Both compounds present a ϕ_f of 0,024 and τ_f exhibiting a dominant component with a lifetime of 0.90 sec (92%) (inset figure 33B).

Irradiation of a solution of compound **3** in MeOH:PB (1:1 v/v) with red light (671 nm) and under N_2-saturated conditions, leads to the absorption spectral changes

reported in figure 34A: it is possible to observe a bleaching of the two absorption bands in the Vis and in the UV region and the appearance of a new absorption band with a maximum at 390 nm. These variations clearly suggest the NO detachment from N-nitrosamine moiety and the formation of compound **3a** which is characterized by a lower molar absorptivity in the UV/Vis region and the presence of an absorption band at 390 nm.

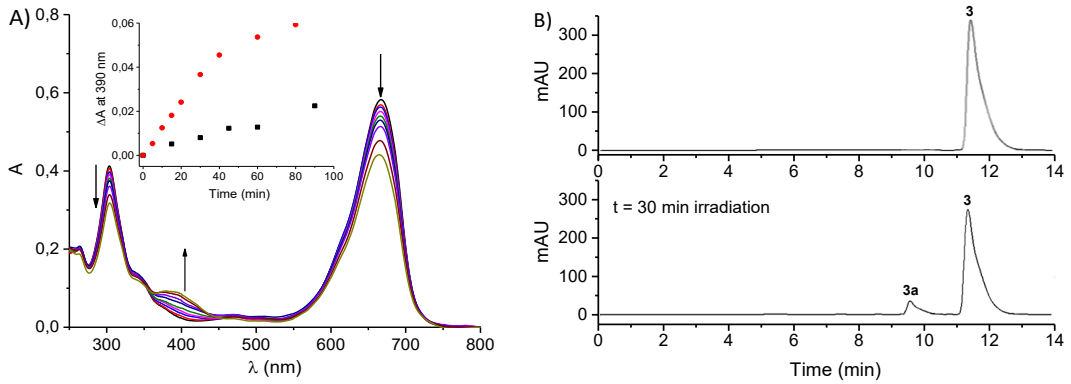

Figure 34. A) Absorption spectral changes observed upon exposure of a N_2-saturated solution of compound **3** to red light (λ_{exc} = 670 nm) for different time intervals (0-80 min). The arrows indicate the course of the spectral profile. The inset shows the difference absorbance changes at 390 nm in N_2-saturated (red) and air-equilibrated (black) solutions. B) HPLC traces related to solutions of compound **3** (50 μM) before (top) and after 30 min irradiation with red light (bottom). PB:MeOH (1:1 v/v) T = 25 °C.

Moreover, the presence of two isosbestic points at 583 and 324 nm in the photolysis profile is indicative of the occurrence of a very clean photoreaction. The nature of the photoproduct was confirmed with HPLC analysis carried out using the authentic compound **3a** as reference (Figure 34B). The same photoreaction was performed in air-equilibrated conditions: the evolution of the absorption profile was identical in nature but slower when compared to that observed under N_2-saturated conditions (see inset of figure 34A). This observation provides the first indication of the involvement of the long-lived excited triplet state of the

benzophenothiazine moiety in the photoreactivity of compound **3** and is further confirmed by the same values of ϕ_f and τ_f observed for compound **3** and **3a**.

The NO release has been unequivocally demonstrated by its real time detection through an amperometric technique using an ultrasensitive electrode (Figure 35). The amperogram demonstrates that the NO release is exclusively regulated by the red light since it starts when the red light is turned on and stops when it is turned off.

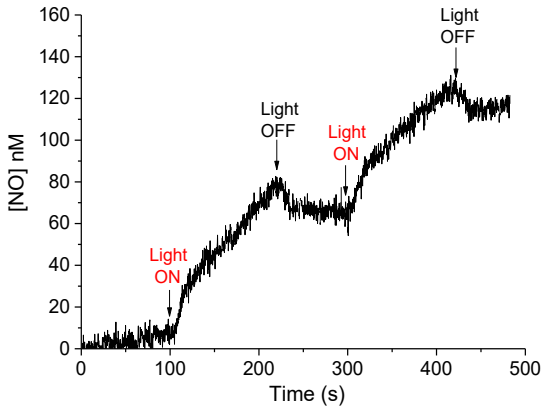

Figure 35. NO release profile observed for a solution of **3** upon alternate cycles of red light (λ_{exc} = 670 nm) and dark. [compound **3**] = (8.5 µM); PB:MeOH (1:1 v/v), T = 25 °C.

The mechanism at the basis of the NO release is certainly a photoinduced electron transfer mediated by the lowest excited triplet state. Since the phenothiazine moiety is the only part of the molecule absorbing in the red region, the NO release must necessarily involve an electronic communication between the antenna and the N-nitrosoaniline derivative. A photoinduced energy transfer from the excited phenothiazine moiety to the N-nitroso appendage is not possible because highly endergonic [71]. Consequently, NO release must be triggered by a photoinduced electron transfer. This hypothesis is supported by the negative free energy value

for the photoinduced triplet electron transfer processes, ΔG ≈ 0.2 eV, estimated by the Rehm-Weller equation 12 [72]:

$$\Delta G = e[E_{ox} - E_{red}] - E_T \qquad (12)$$

where E_{ox} is the half-wave potential for one-electron oxidation of the electron-donor unit, ca. 1 eV vs. NHE [73], E_{red} is the half-wave potential for one-electron reduction of the electron-acceptor unit, ca. –0.2 eV vs. NHE [74], and E_T is the average energy of the lowest excited triplet states of the light harvesting centers, ca. 1.4 eV [75].

Such photoinduced electron transfer between two species separated by an insulator spacer requires their spatial proximity. Molecular dynamics simulations show that compound **3** assumes a U-shaped conformation with the electron donor and the electron acceptor coming to be very close in the space (Figure 36).

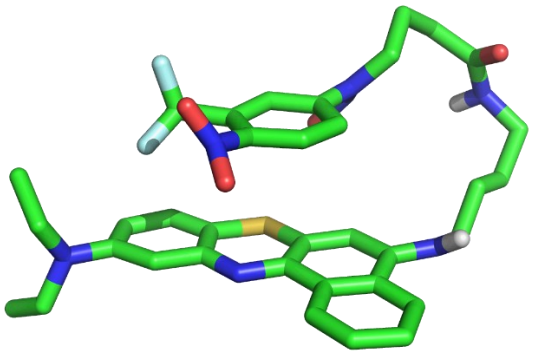

Figure 36. Collapsed U-shaped conformation assumed by compound **3** during the molecular dynamics simulation.

3.3.4 Evidence of the peroxynitrite photogeneration

The generation of peroxynitrite is strongly correlated to the simultaneous generation of NO and $O_2^{\bullet-}$ and as just underlined above, the benzophenothiazine

moiety has been chosen for its capability to generate $O_2^{\bullet-}$. At this point, it is important to evaluate if this capability has been maintained even after binding with the N-nitrosoaniline derivative.

The generation of $O_2^{\bullet-}$ is the result of the quenching of the lowest triplet state by molecular oxygen through Type I reaction [76, 77]. The earliest evidence of the $O_2^{\bullet-}$ formation arises out of the analysis of nitrite formed after irradiation and its quantitative comparison with the only stable photoproduct **3a**. Indeed, in absence of other reactive species, the released NO is almost quantitatively oxidized to NO_2^- but not to NO_3^- by molecular oxygen [78]. In such a case NO_2^- and compound **3a** are expected to be found in equimolar ratio. The nitrite analysis has been performed using two different tests: the DAN test [79] and the Griess test [80].

NO_2^- were first evaluated by means of the well-known and highly sensitive (detection limit on the order of the picomoles) spectrofluorimetric DAN assay [79]. It is based on the acid catalyzed ring closure of the nonfluorescent 2,3-diaminonaphthalene (DAN) with NO_2^- to form the highly fluorescent product 2,3-diaminonaphthotriazole (DANT) (Scheme 5). On the other hand, NO_3^- yields no reaction product.

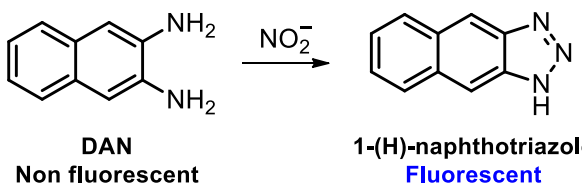

Scheme 5. DAN test mechanism.

Figure 37A clearly shows the characteristic well-structured fluorescence emission and excitation spectra of the DANT only in the irradiated solution of compound **3** and with intensity strictly dependant on the irradiation time. Quantitative

comparison between NO_2^- and compound **3a** was performed in the early stage of the photoreaction (after 30 minutes of irradiation) by the spectrophotometric Griess test [80]. Data reported in Figure 37B (first two columns) show a marked difference between the amount of NO_2^- and that of compound **3a**, with the related % (mol/mol^{-1}) being 3.2 ± 0.5 and 9.6 ± 1.4, respectively.

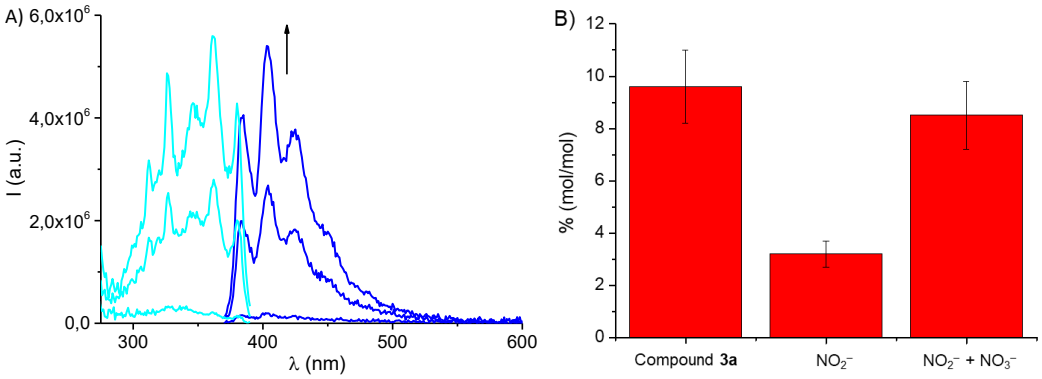

Figure 37. Analysis of NO_2^-. A) Fluorescence excitation (cyan) and emission (blue) spectra obtained after fluorimetric DAN assay of solutions of compound **3** (8.5 µM) after 0, 30 and 60 min of irradiation (from bottom to top) with red light at λ_{exc} = 670 nm. The emission wavelength for the excitation spectra was 410 nm whereas the excitation wavelength for the emission spectra was 360 nm. B) Quantitative comparison performed through Griess test which shows the % (mol/mol) of the photoproduct **3a** and the amounts of NO_2^- and NO_2^-+ NO_3^- (after treatment with VCl_3) observed after 30 min of irradiation. PB:MeOH (1:1 v/v), T = 25 °C.

This result clearly suggests the formation of $O_2^{\bullet-}$ which rapidly converts the NO photoreleased into $ONOO^-$ before it can be slowly oxidized to NO_2^- by molecular oxygen. How can be this proved? $ONOO^-$ is in equilibrium with its conjugate acid, ONOOH (pKa = 6.8). The decomposition pathway of $ONOO^-$ and of its conjugate acid ONOOH leads to the formation of large amount of NO_3^-. On these bases, the NO_2^- analysis has been performed again after treatment of the irradiated solution with vanadium trichloride (VCl_3) which is able to reduce NO_3^- to NO_2^-. The result of the Griess test reported in figure 37B (compare the first and the third columns) shows that the total amount of NO_2^- detected after treatment of the irradiated solution

with VCl_3 remarkably increased reaching a value very close to that of the photoproduct **3a**.

Obviously, the direct detection of $ONOO^-$ represents the best way to confirm all the hypothesis. Generation of $ONOO^-$ was demonstrated using fluorescein-boronate (Fl-B), a very selective and sensitive probe for $ONOO^-$ which has been recently developed [81]. Fl-B is weakly fluorescent, but it is rapidly ($k \sim 10^6\ M^{-1}\ s^{-1}$) and effectively (yield = 99%) oxidized by $ONOO^-$, liberating the highly fluorescent fluorescein (Scheme 6).

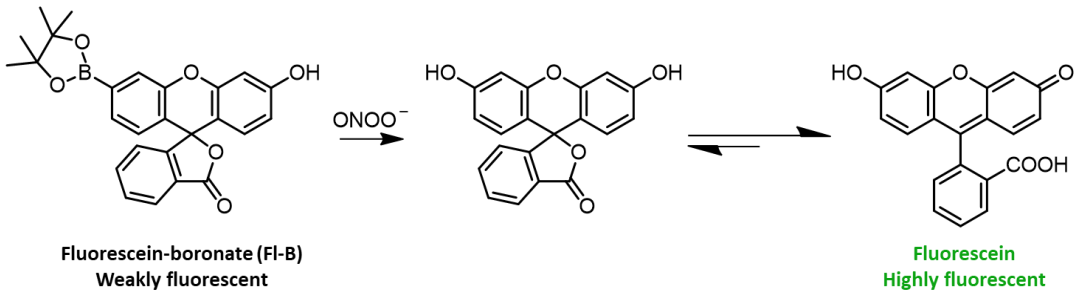

Scheme 6. Oxidation of Fl-B to yield the corresponding phenol. The product of the reaction is in tautomeric equilibrium with the open lactone named fluorescein, a highly fluorescent product. In aqueous solution and at pH 7.4, the monoanionic (pKa 4.3) and dianionic (pKa 6.4) forms of the open lactone are predominant.

Irradiation of an air-equilibrated solution of compound **3** in presence of Fl-B leads to the oxidation of the probe and the formation of fluorescein. Figure 38A clearly shows the appearance of the typical fluorescence excitation and emission spectra of fluorescein with λ_{max} = 490 nm and 520 nm, respectively. The same experiment has been performed under N_2-saturated conditions (inset figure 38A); under these conditions, where $O_2^{\bullet-}$ is not generated, negligible fluorescein emission was observed confirming the good selectivity of this probe for the $ONOO^-$ detection. Besides, the same experiment under air-equilibrated conditions has been performed with the model compound **3a** (inset figure 38A). In this case, a lower

emission increase was observed, according to the absence of NO photorelease occurring in this compound. However, this low emission increase could result from the very slow oxidation (k ~ 1-2 M^{-1} s^{-1}) of Fl-B by the H_2O_2 [77] derived by the slow dismutation of $O_2^{\bullet-}$, which in compound **3a** is expected to be produced similarly to compound **3**.

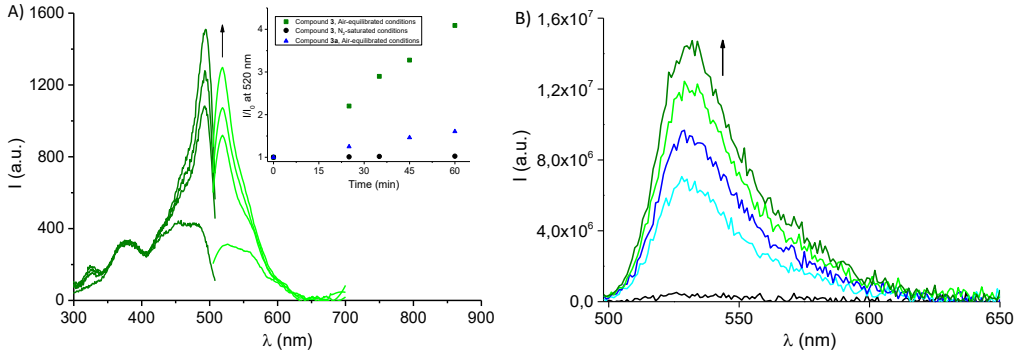

Figure 38. A) Fluorescence emission (green) and excitation (olive) spectra recorded at λ_{exc}= 492 nm and λ_{em}= 520 nm, respectively, observed upon irradiation with red light at λ_{exc}= 670 nm of an air-equilibrated solution of compound **3** in the presence of Fl-B. The arrow indicates the course of the spectral profile with the illumination time. The inset shows the fluorescence emission increase observed at λ = 520 nm in the case of the air-equilibrated solutions of compound **3** (green) and the model compound **3a** (blue), and a N_2-saturated solution of compound **3** (black) (I and I_0 represent the fluorescence intensities after and before irradiation, respectively). [compound **3**] = [Fl-B] = [compound **3a**] = 25 µM; PB : MeOH (1 : 1 v/v); T = 25 °C. B) Fluorescence emission spectra recorded at λ_{exc} = 488 nm, observed upon irradiation with red light at λ_{exc} = 670 nm of an air-equilibrated solution of compound **3a** in the presence of DHR123. The arrow indicates the course of the spectral profile with the illumination time (0, 2, 4, 6 and 8 min). [compound **3a**] = [DHR123] = (10 µM); PB:MeOH (1:1 v/v), T = 25 °C.

This hypothesis was confirmed by using the dihydrorhodamine 123 (DHR123) as a probe for $O_2^{\bullet-}$; DHR123 is a non-fluorescent compound which is converted into the highly fluorescent Rhodamine 123 after reaction with $O_2^{\bullet-}$ [69a]. The fluorescence emission spectra reported in Figure 38B clearly shows the formation of Rhodamine 123 upon irradiation of an air-equilibrated solution of compound **3a** in presence of DHR123.

Quantitative comparison between the amount of the photoproduct **3a** and the fluorescein formed in the early stage of the photoreaction (30 minutes of irradiation) was performed by HPLC and revealed the % (mol/mol) for these compounds to be 9.8 $\pm$ 1.3 and 7.4 $\pm$ 1.1, respectively. Since $ONOO^-$ quantitatively oxidizes Fl-B to fluorescein, this finding suggests that NO is produced only slightly in excess with respect to $O_2^{\bullet-}$ (ca. 1.3-fold).

A specific point that needs to be clarified is related to the photodegradation mechanism proposed in Figure 32. The type I reaction involved in the generation of $O_2^{\bullet-}$ involves the formation of a benzophenothiazine-centered radical cation, which is expected to evolve to products besides compound **3a**. Therefore, the observation of compound **3a** as the only stable product of photolysis can seem surprising. A possible hypothesis to explain this finding might consist into a typical deprotonation of the benzophenothiazine-centered radical cation, leading to neutral radical species which would restore the starting benzophenothiazine chromophore by H-transfer from the solvent.

3.3.5 Cell internalization and viability assay

Biological activity of compound **3** was evaluated using two different cancer cell lines, HeLa (derived from a human cervix carcinoma) and MDA-MB-231 (derived from a human breast carcinoma).

The intracellular localization of compound **3** was determined by confocal fluorescence microscopy. Fluorescence images of the cells reported in Figure 39 show that the hybrid is mainly located within the endoplasmic reticulum and the Golgi apparatus of both cancer cell lines. Poor localization has also been observed in lysosomes and mitochondria.

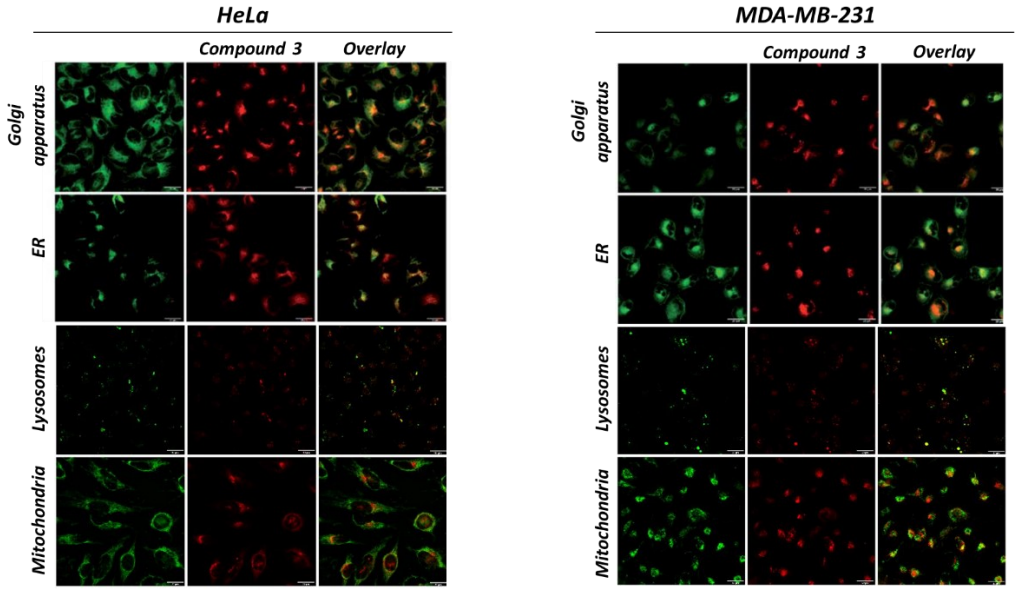

Figure 39. Confocal images of cancer cells incubated for 2 h with 0.5 µM compound **3** (red fluorescence). The cells are stained with BODIPY® FL C5-ceramide (Golgi apparatus), ER-Tracker™ Green (endoplasmic reticulum ER), LysoTracker Green (lysosomes) or MytoTracker Green (mitochondria) (green fluorescence). Overlays of red and green fluorescence are shown in the right of each panel. Scale bar = 20 µm.

The cellular uptake of compound **3** was determined by flow cytometry analysis in presence of different concentration of compound **3** (0.25, 0.5 and 1 µM) and after 2 hours incubation. The results (reported in Figure 40A) show an efficient intracellular uptake which is strictly dependent on the concentration of compound **3**.

To evaluate the efficacy of compound **3** as a phototherapeutic agent, both cancer cell lines were incubated for 2 h with increasing concentrations of compound **3** and either kept in the dark or irradiated with very low doses of red light (1 J cm^{-2}). The results are reported in Figure 40B. The compound is well tolerated in the dark in a concentration range below 2 µM. In contrast, in the same concentration range a remarkable decrease of cell viability was observed with both cell lines upon

irradiation. Moreover, the loss of cell viability is strictly dependent on the concentration of compound **3**.

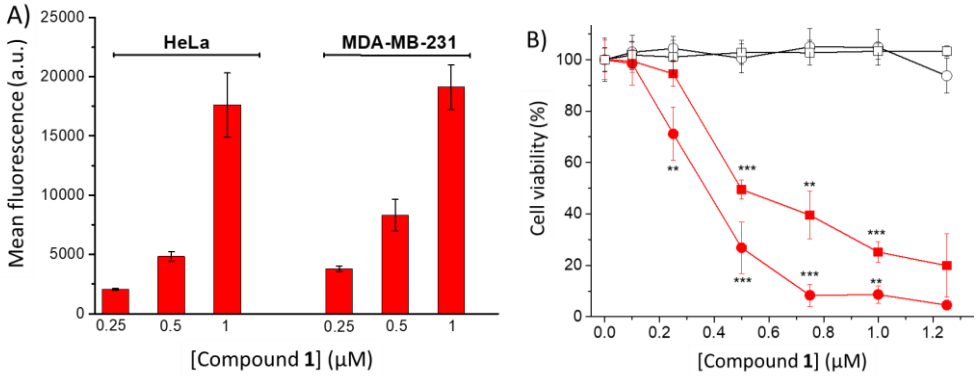

Figure 40. Cell viability of HeLa (circles) and MDA-MB-231 (square) cancer cells incubated for 2 h with compound **3** and either kept in the dark (open symbols) or irradiated (filled circles) with red light at a fluency of 1 J cm^{-2} (40 mW cm^{-2} for 25 s). *p < 0.05; **p < 0.1; ***p < 0.001.

It is important to underline that the strong phototoxic effect has been induced by using very low concentrations of compound **3** and very low doses of red-light irradiation. This result is in excellent agreement with the high toxicity of the $ONOO^-$ and has also been confirmed by the lower phototoxic effects exhibited by the model compound **3a** (data not shown).

3.3.6 Conclusion

In conclusion, it has been designed and developed a novel molecular hybrid which represents the first example of $ONOO^-$ generator activatable with the highly biocompatible and tissue penetrating red light. Excitation of this molecular construct with red light triggers the release of NO from the N-nitroso moiety, mediated by an intramolecular electron transfer, and produces $O_2^{\bullet -}$, through a Type I mechanisms from the lowest excited triplet state of the benzophenothiazine.

$ONOO^-$ is then generated due to the diffusion-controlled reaction between these two species. The hybrid presents the additional advantage of the red fluorescence which allows its cellular tracking in HeLa and MDA-MB-231 cancer cells. Moreover, it is well tolerated in the dark by both cell lines at concentrations up to ca. 2 µM. In contrast, irradiation with red light in this very low concentration range with very low light doses (ca. 1 J cm^{-2}) results into remarkable levels of cell mortality according to the very high cytotoxicity of $ONOO^-$.

3.4 A High-Performing Nonmetal-Containing Photoactivatable NO Donor with a Green Fluorescent Reporter

3.4.1 Design

As stressed in the introductive chapter of this work, the biological effects of NO are highly site- and dosage-dependent. The quantification and the localization of the NO released represent an important issue to be faced. One way to address this task is to use systems which are based on the principle of the "*release with fluorescence reporting*". A novel NOPD activatable with blue light and with an in-built green fluorescent reporter has been developed (figure 41) [82].

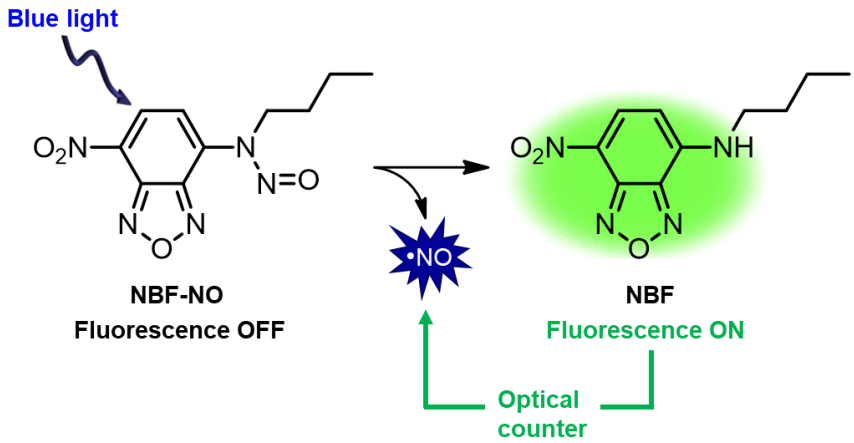

Figure 41. Structures of **NBF-NO** and of its stable photoproduct **NBF** which is generated after NO release.

NBF-NO is a nitroso-derivative of the 4-amino-7-nitrobenzofurazane (ABF) and bears a short alkyl chain to facilitate its entrapping into hydrophobic carrier system. It belongs to the family of intramolecular charge transfer molecules, with the amino group which act as an electron donor and the nitro group which act as an electron acceptor [83]. The choice to use a derivative of ABF was driven by different reasons: the main absorption band with "push-

pull" character of these compounds falls in the blue region of the Vis range and is characterized by a considerably high absorption coefficient (larger than 10^4 $M^{-1}cm^{-1}$). Moreover, they exhibit excellent fluorescence in the green region with quantum yield values, Φ_f which strongly depend on the solvent polarity [83b].

3.4.2 Synthesis

The synthesis of **NBF-NO** has been performed following the procedure reported in Scheme 7. All syntheses were carried out under a low intensity level of visible light.

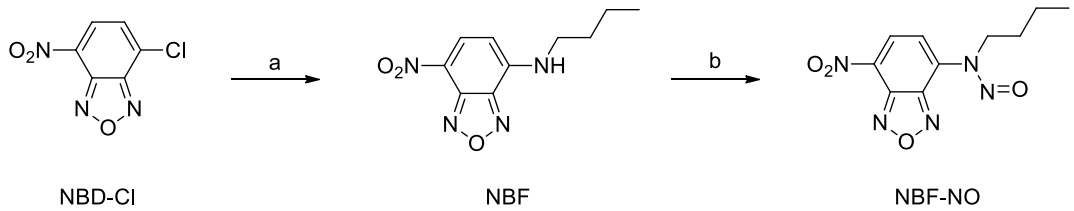

Scheme 7. a) Butylamine, CH_3CN dry, N_2, r.t., 2 hours, 97%; b) $NaNO_2$, CH_3COOH:THF (1:1 v/v), r. t., 12 hours, 50%.

N-butyl-7-nitro[1,2,3]benzoxadiazol-4-amine (NBF)

To a solution of NBD-Cl (100 mg, 0.5 mmol) in dry CH_3CN (40 mL) stirred at room temperature under N_2, butylamine (250 µL) was added dropwise. The reaction mixture was stirred at room temperature for 2 hours and then the solvent was removed under reduced pressure. DCM (20 mL) was added to the residue which was washed with water (3 x 15 mL) and brine (3 x 15 mL), dried over Na_2SO_4 and concentrated to dryness. Purification of the residue by flash chromatography, using Cy:EtOAc (4:1 v/v)as eluent, gave **NBF** as an orange solid (115 mg, 97%). Melting point 91-93 °C. HRMS (ESI): $[M+H]^+$ = 237.09778. ^1H NMR (200 MHz, $CDCl_3$): δ 8.51

(d, *J* = 8.7 Hz, 1H), 6.19 (d, *J* = 8.7 Hz, 1H), 3.61 – 3.40 (m, 2H), 1.94 – 1.69 (m, 2H), 1.67 – 1.38 (m, 2H), 1.03 (t, *J* = 7.2 Hz, 3H).

N-butyl-N-(7-nitro[1,2,3]benzoxadiazol-4-yl)nitrous amide (NBF-NO).

To a solution of **NBF** (60 mg, 0,25 mmol) in THF:CH_3COOH (1:1 v/v; 10 mL) cooled at 0 °C with an ice bath, sodium nitrite (140 mg, 2 mmol) was added; the reaction mixture was stirred at 0 °C for 1 hour and at room temperature for 12 hours. The solvent was removed under reduced pressure and the residue was purified through flash chromatography, using Cy:EtOAc (4:1 v/v) as eluent, to give **NBF-NO** as a yellow solid (34 mg, 50%). Melting point 59- 60 °C. HRMS (ESI): $[M+H]^+$ = 266.08779. ^1H NMR (200 MHz, $CDCl_3$): δ 8.64 (d, *J* = 8.3, 0.7 Hz, 1H), 7.81 (d, *J* = 8.3, 0.7 Hz, 1H), 4.47 – 4.37 (m, 2H), 1.66 – 1.47 (m, 2H), 1.45 – 1.26 (m, 2H), 0.94 (td, *J* = 7.3, 0.7 Hz, 3H). ^{13}C NMR (50 MHz, $CDCl_3$): δ 145.09, 144.47, 137.93, 132.30, 114.51, 44.72, 29.50, 20.71, 14.11.

3.4.3 Photochemical characterization and NO release

Figure 42A reports the absorption spectra in MeOH:H_2O (1:1 v/v) of **NBF-NO** and of **NBF**, the corresponding non nitrosate compound. The absorption spectrum of this latter presents a main absorption band at *ca* 470 nm which is blue-shifted by *ca* 90 nm in the absorption spectrum of **NBF-NO** due to the introduction of the NO group at the amino functionality. However, the large extinction coefficient and the broad band shape make possible to excite **NBF-NO** in the visible region. The introduction of the NO group on the amino functionality leads also to a drastic quenching of the intense green fluorescence (see figure 42B): the fluorescence quantum yield value passes from 0.13 for **NBF** to 0.01 for **NBF-NO**, more than 1 order of magnitude of difference.

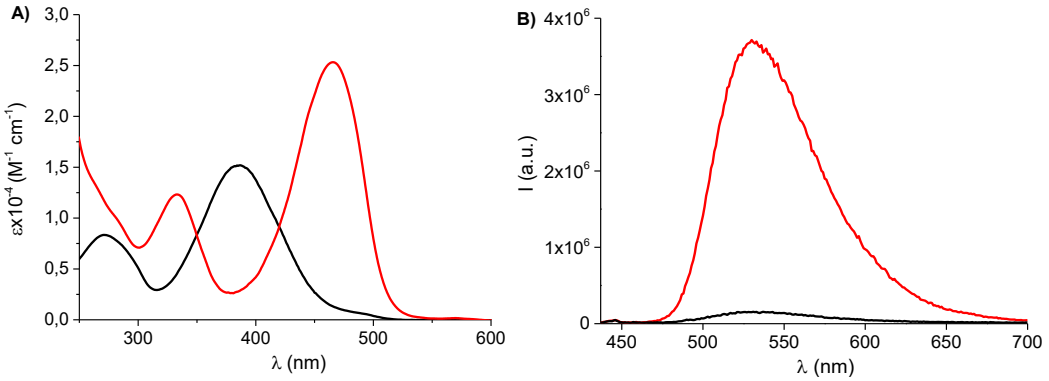

Figure 42. A) Absorption spectra and B) fluorescence emission spectra of **NBF** (red line) and **NBF-NO** (black line) in MeOH:H_2O (1:1 v/v) recorded at λ_{exc}=427 nm.

The NO release was evaluated under aerobic conditions following the absorption and emission spectral changes. Irradiation of a solution of **NBF-NO** in MeOH:H_2O (1:1 v/v) with blue light leads to the bleaching of the band at 385 nm, the formation of a new intense band at 475 nm and 4 clear isosbestic points which are indicative of a very clean photoreaction (figure 43A).

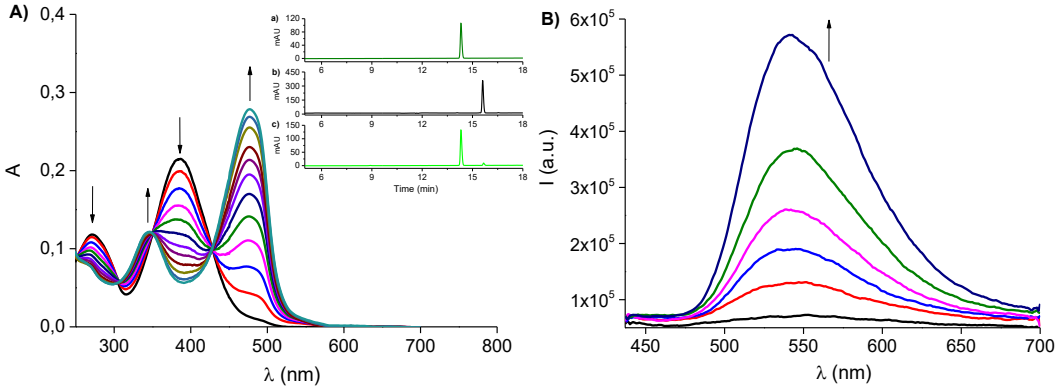

Figure 43. A) Absorption spectral changes observed upon exposure of a solution of **NBF-NO** (15 μM) at λ_{exc} = 420 nm (ca. 20 mW cm^{-2}) for time intervals from 0 to 75 s. The arrows indicate the course of the spectral profile with the illumination time. The inset shows. HPLC traces related to solutions of a) **NBF**, b) **NBF-NO** and c) **NBF-NO** after 60 s irradiation at λ_{exc} = 420 nm. B) Evolution of the fluorescence emission spectra corresponding to the sample of figure A and recorded at λ_{exc} = 427 nm. MeOH:H_2O (1:1 v/v).

The spectrum at the end of the photolysis is identical to that of **NBF**; HPLC analysis carried out using **NBF** as reference confirmed the nature of the photoproduct and the fact that the photorelease of NO occurs from **NBF-NO** (see inset Figure 43A). Moreover, the fluorescence emission spectra (figure 43B) show a dramatic revival of the emission with a λ_{max} = 546 nm. This finding clearly suggests that **NBF** can be a suitable optical reporter to follow the NO uncaging. The quantum yield for the NO photorelease, Φ_{NO} is 0.15, a value which is ca 1 order of magnitude larger than that reported for other organic NOPD activatable with visible light. Such an high value of Φ_{NO} founds a rational explanation in the mechanism which is at the basis of the NO release; excitation of **NBF-NO** leads to the homolytic cleavage of the N-NO bound and to the formation of an anilinyl radical which is stabilized by the nitro group. The anilinyl radical evolves to the stable photoproduct **NBF** via H-transfer from solvent, a mechanism already seen in the case of the other N-nitrosamine after loss of NO.

3.4.4 Encapsulation of NBF-NO within polymeric micelles and NO release

In view of a biological application, an important issue to be faced regards the encapsulation of **NBF-NO** within biocompatible polymeric carriers and the evaluation of the preservation of its photochemical performances also once encapsulated. Poly(ethyleneoxide)/poly(propyleneoxide)/poly(ethyleneoxide) (PEO-PPO-PEO) triblock copolymers are FDA-approved excipients for pharmaceutical use and available in the market under the trademark Pluronic®, in a large range of molecular weight and different ratio between PEO and PPO units. In particular, we used Pluronic® P123 (EO_{20}–PO_{70}–EO_{20}, MW *ca.* 5,750 g mol^{-1}) and F127 (EO_{100}–PO_{70}–EO_{100}, MW *ca.* 12,600 g mol^{-1}) as suitable polymeric component. Due to the same length of propylene chain, they self-assemble into core-shell

micelles with a hydrophobic core of PPO and a hydrophilic PEO shell which confers high colloidal stability, high capacity to encapsulate hydrophobic drugs and reduced critical micelle concentration (cmc). Water formulations were prepared at 0.5% (w/v) of Pluronics at P123:F127 ratio of 1:1 (w/w). Under these conditions the cmc is 0.0030%. These properties guarantee the presence of micelles with diameter *ca*. 30 nm in the experimental condition used.

The black spectrum of Figure 44A shows the absorption spectrum of a solution of **NBF-NO** encapsulated within Pluronics micelles. This spectrum represents the proof of the occurred encapsulation since **NBF-NO** is poorly soluble in water but effectively solubilizes in the presence of Pluronic® micelles as confirmed by the appearance of its typical absorption spectrum with maximum at 385 nm.

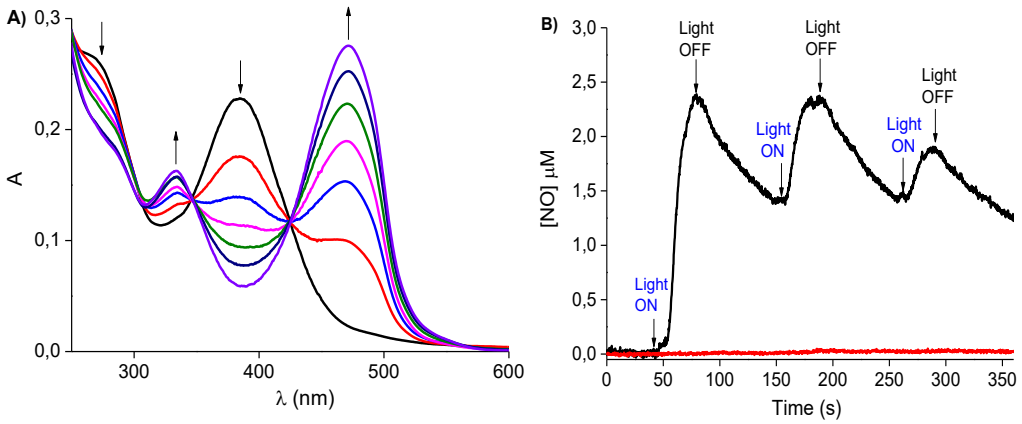

Figure 44. A) Absorption spectral changes observed upon exposure of a solution of **NBF-NO** (15 µM) encapsulated in 0.5 % (w/v) Pluronic mixed micelles P123:F127 (1 : 1) at λ_{exc}=420 nm (ca. 20 mW cm^{-2}), for time intervals from 0 to 15 s. The arrows indicate the course of the spectral profile with the illumination time. B) NO release profiles observed for micellar solutions of **NBF-NO** (15 µM) and of **NBF** (15 µM), encapsulated in 0.5 % (w/v) Pluronic mixed micelles P123 : F127 (1 : 1) upon alternate cycles of light λ_{exc}=420 nm (ca. 20 mW cm^{-2}).

Irradiation with blue light of this micellar solution leads to the same spectral changes observed in the absence of micelles, according to the formation of **NBF** as

stable photoproduct (figure 44A). However, the photoreaction was completed in less than 15 seconds (against the 75 seconds needed for the reaction in MeOH:H_2O 1:1). The quantum yield Φ_{NO} in this case is 0.80, a remarkably high value even if compared with other organic NOPDs encapsulated in carrier systems. This enhanced photoreactivity can be explained considering the active role that the polymeric network plays in providing easily abstractable hydrogens close to the anilinyl radical. NO release was once again demonstrated by the direct detection of this radical through amperometric technique; the amperogram clearly shows that the release of NO is exclusively regulated by light since it stops in the dark and restart once the illumination is turned on again (figure 44B). A similar micellar solution of **NBF** was used as control; any detectable signal was observed in this case proving that the signal observed can be safely attributable to the NO released from **NBF-NO** and cannot be ascribed to other effects like the intense fluorescence restored.

Figure 45A shows the dramatic revival of the green emission, typical of the **NBF** fluorophore, demonstrating that the fluorescence activation upon light irradiation was well preserved in the micellar system. The restoring of the emission of the optical reporter is visible even at naked eye (see inset of figure 45B). The NO photorelease measured by its direct detection was then related to the increase of the fluorescence emission. As shown in Figure 45B, there is a very good correlation between the concentration of NO photogenerated and the increase of the fluorescence intensity of the optical reporter .

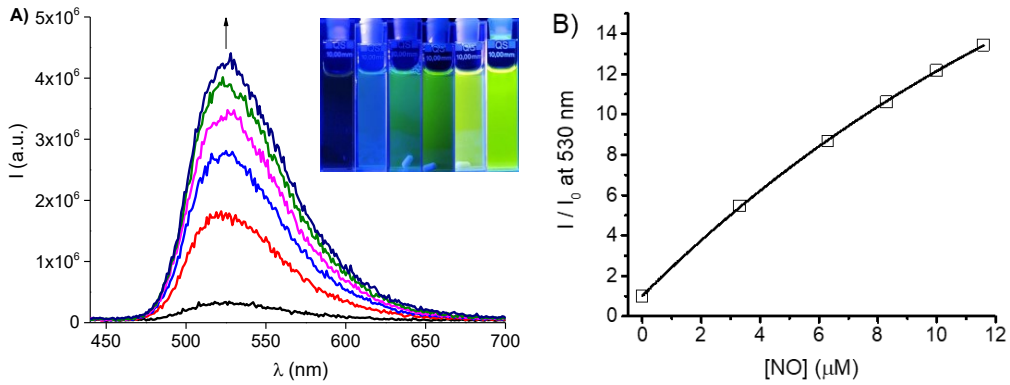

Figure 45. A) Evolution of the fluorescence emission spectra corresponding to the sample of Figure 44A and recorded at λ_{exc} = 427 nm (isosbestic point). The inset shows the actual images of the samples acquired under illumination with a blue LED. B) Correlation between the concentration of NO released under light stimulus and measured by direct amperometric detection and the fluorescence increase observed in Figure 45A. I_0 and I represent the fluorescence intensities before and after irradiation.

3.4.5 Conclusion

A novel NOPD activatable with blue light has been developed. This NOPDs releases NO with excellent photochemical performances, with a quantum yield of 0,15 in solution and simultaneously releases a single, highly fluorescent stable photoproduct. The remarkable fluorescence difference between the photoproduct and the poorly fluorescent starting compound permits the former to be an excellent optical reporter for the easy detection and quantification of the NO released. The developed NOPD can be effectively encapsulated in biocompatible polymer micelles of Pluronic®, where it preserves the nature of the photoprocess but increases its photochemical efficiency. Indeed, the quantum yield for the NO release increases up to 0,80, the largest value ever reported in literature for nonmetal-containing NO donors activatable with visible light. Besides, this NOPD presents the additional advantage of a simple, high-yield and inexpensive synthesis.

3.5 A molecular dyad delivered by biodegradable polymeric nanoparticles for combined PDT and NO-PDT in cancer cells

3.5.1 Design

As already explained in the introductive chapter of this work, NO-PDT is opening new possibilities in the field of multimodal therapeutic strategies. Molecular dyads integrating PSs and NOPDs within the same molecular skeleton offer the advantage to photorelease $^1O_2$ and NO in the same cellular compartment [84]. However, for an effective outcome of the photodynamic action, the generation of comparable amounts of $^1O_2$ and NO is highly desirable. This is in general a difficult task since the $^1O_2$ quantum yields (Φ_Δ) of many PSs are often much larger than those of NO (Φ_{NO}) of organic NOPD [85].

A novel hybrid has been designed in order to release simultaneously $^1O_2$ and NO with comparable quantum yield and, as a consequence, to obtain improved photodynamic action [86]. The new hybrid combines the novel NOPD **NBF-NO** and an iodinate BODIPY as PS in the same molecular skeleton by a flexible alkyl spacer (see Figure 46). This choice is dictated by the fact that as already seen in the previous chapter of this work, **NBF-NO** releases NO with Φ_{NO} = 0.15, which increases up to 0.80 in Pluronic® micelles, the largest values ever reported for nonmetal-containing NO donors activatable by visible light. Such values are comparable with the typical Φ_Δ of many PSs, like iodinated BODIPY.

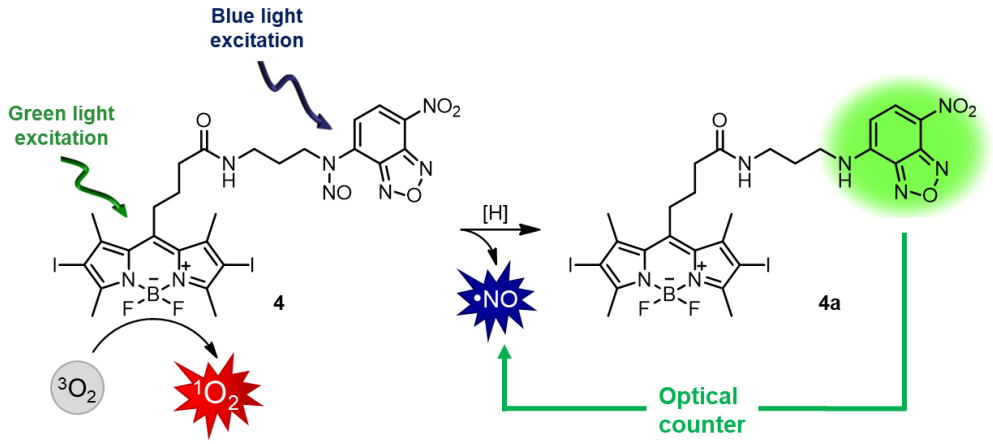

Figure 46. Structures of hybrid **4** and of its stable photoproduct **4a** which is generated after NO release.

3.5.2 Synthesis

The hybrid has been synthesized following the scheme 8 under low intensity level of visible light. Compounds **4b** and **4e** were synthetized according to literature [87]. Briefly, the coupling of the N-BOC-1,3-propanediamine **4b** with the commercially available NBD-Cl in acetonitrile at room temperature gave compound **4c** which in turn was treated with TFA in DCM to yield compound **4d.** The BODIPY succinimidyl ester **4e** was treated with compound **4d** in a mixture of DCM/THF to give the expected compound **4f**. This intermediate was easily iodinated at the 2- and 6-positions by treatment with iodine and iodic acid to afford compound **4a**. The desired compound **4** was obtained through nitrosation of compound **4a** with $NaNO_2$ and CH_3COOH.

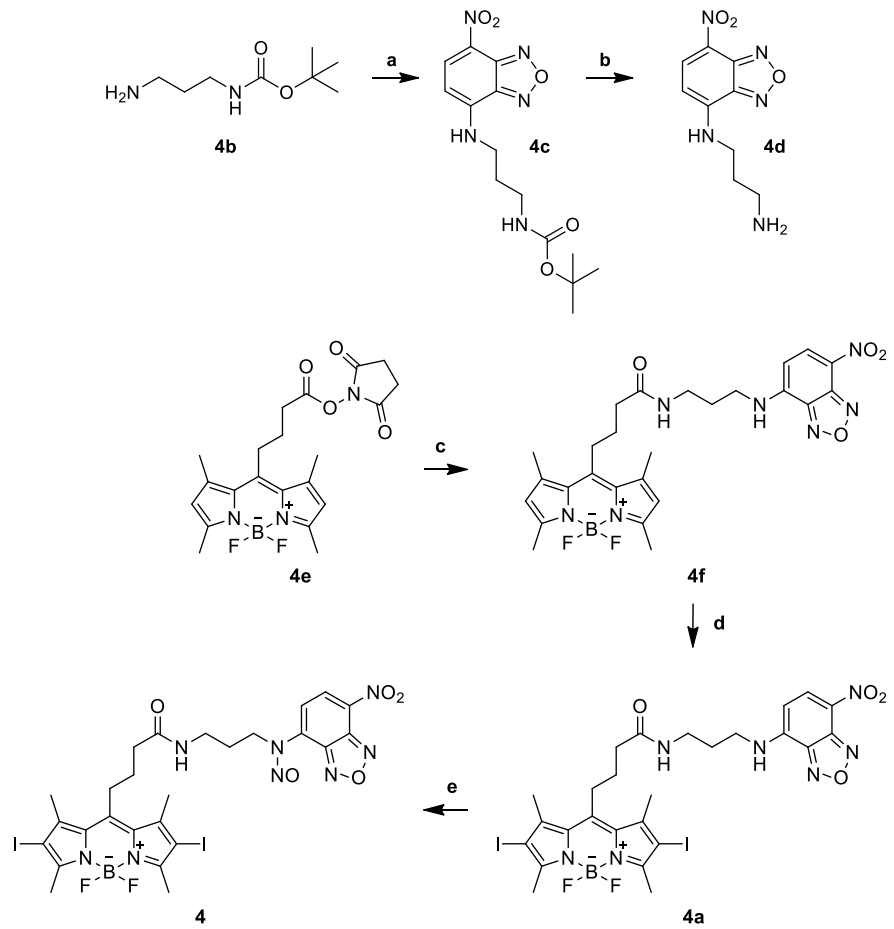

Scheme 8. a) NBD-Cl, CH_3CN, 2h, r.t..; b) DCM/TFA 10:1, 5 h, 0°C →r.t.; c) **4e**, DCM/THF 10:1, 24 h, r.t.; d) I_2, HIO_3, THF/H_2O 10:1, overnight, r.t.; e) $NaNO_2$, THF/CH_3COOH 4:1, 24 h, 0°C > r.t.

Tert-butyl (3-((7-nitrobenzo[c][1,2,5]oxadiazol-4-yl)amino)propyl)carbamate (4c)

A solution of NBD-Cl (653 mg, 3.27 mmol) in dry acetonitrile (CH_3CN, 100 mL) was slowly added to a stirring solution of **4b** (570 mg, 3.7 mmol) in dry CH_3CN (200 mL) cooled at 0 °C with an ice bath. The reaction mixture was allowed to proceed at room temperature for 2 hours. Then the solvent was removed under reduced pressure. Purification by flash chromatography eluting with Cy: EtOAc (50:50 v/v) gave compound **4c** as a brown solid (300 mg, 27%). Anal. Calcd (%) for $C_{14}H_{19}N_5O_5$:

C, 49.85; H, 5.68; N, 20.76; O, 23.71. Found: C, 49.82; H, 5.69; N, 20.77; O, 23.72. $[M+H]^+$: m/z 338,14. ^1H NMR (CH_2Cl_2, 500 MHz). δ 8.47 (d, J = 8.7 Hz, 1H), 7.49 (s, 1H), 6.20 (d, J = 8.7 Hz, 1H), 4.87 (s, 1H), 3.58 (q, 2H), 3.28 (q, J = 6.3 Hz, 2H), 1.89 (q, J = 6.3 Hz, 2H), 1.46 (s, 12H).

N^1-(7-nitrobenzo[c][1,2,5]oxadiazol-4-yl)propane-1,3-diamine (4d)

To a stirring solution of **4c** (300 mg, 0,89 mmol) in DCM (50 mL) cooled at 0 °C with an ice bath, 5 mL of trifluoroacetic acid (TFA) was added dropwise. The resulting solution was stirred for 5 hours at room temperature. The solvent was removed under reduced pressure, the residue was dissolved in EtOAc (100 mL) and washed with a saturated sodium bicarbonate solution (2 x 50 mL). The organic phase was dried over Na_2SO_4 and concentrated to dryness. Purification by flash chromatography eluting with Acetone:DCM (80:20 v/v) gave compound **4d** as an orange solid (150 mg, 70%). Anal. Calcd (%) for $C_9H_{11}N_5O_3$: C, 45.57; H, 4.67; N, 29.52; O, 20.23. Found: C, 45.58; H, 4.71; N, 29.51; O, 20.20. ESI-MS $[M+H]^+$: m/z 238,09. ^1H NMR (Acetone-d_6, 500 MHz). δ 8.5 (d, J = 8.7 Hz, 1H), 6.20 (d, J = 8.7 Hz, 1H), 3.8 (t, 2H), 3.5 (t, J = 6.3 Hz, 2H), 2,1 (m, J = 6.3 Hz, 2H).

4-(4,4-Difluoro-1,3,5,7-tetramethyl-4-bora-3a,4a-diaza-s-indacen-8-yl)-N-(-(7nitrobenzo[c][1,2,5] oxadiazol-4-yl)propyl)butanamide (4f)

To a solution of **4e** (120 mg, 0.32 mmol) in dry DCM (50 mL) and dry THF (3 mL) stirred at room temperature under N_2, compound **4d** (76 mg, 0.38 mmol) was added. The reaction was allowed to proceed at room temperature for 24 hours; then the obtained mixture was washed with H_2O (2 × 20 mL), dried over Na_2SO_4 and concentrated to dryness. Purification by flash chromatography eluting with $CHCl_3$:MeOH (98:2 v/v) gave compound **4f** as an orange solid. (105 mg, 50%). Anal.

Calcd (%) for $C_{26}H_{30}BF_2N_7O_4$: C, 56.43; H, 5.46; B, 1.95; F, 6.87; N, 17.72; O, 11.57. Found: C, 56.40; H, 5.43; B, 1.96; F, 6.90; N, 17.73; O, 11.58. ESI-MS $[M+H]^+$: m/z 554,24. ^{1}H NMR (500 MHz, DMSO-d_6) δ 9.45 (s, 1H), 8.47 (d, *J* = 8.9 Hz, 1H), 8.01 (t, *J* = 5.6 Hz, 1H), 6.38 (d, *J* = 9.0 Hz, 1H), 6.21 (s, 2H), 3.48 (s, 2H), 3.18 (q, *J* = 6.5 Hz, 2H), 2.98 – 2.87 (m, 2H), 2.39 (d, *J* = 3.0 Hz, 12H), 2.28 (t, *J* = 7.0 Hz, 2H), 1.80 (m, *J* = 26.0, 7.8 Hz, 4H).

4-(4,4-Difluoro-2,6-diiodo-1,3,5,7-tetramethyl-4-bora-3a,4a-diaza-s-indacen-8-yl)- N-(-(7-nitrobenzo[c] [1,2,5]oxadiazol-4-il)amino-propyl)butanamide (4a)

A solution of **4f** (50 mg, 0.0904 mmol) in THF (50 mL) was treated with iodine (45.9 mg, 0.181 mmol) followed by iodic acid (31.84 mg, 0.181 mmol) in 4 mL of H_2O. The reaction mixture was stirred at room temperature overnight; then the solvent was removed under reduced pressure. Purification by silica gel chromatography eluting with CH_2Cl_2:MeOH (98:2 v/v) gave **4a** as a red solid (60 mg, 83%). Anal. Calcd (%) for $C_{26}H_{28}BF_2I_2N_7O_4$: C, 38.78; H, 3.51; B, 1.34; F, 4.72; I, 31.52; N, 12.18; O, 7.95. Found: C, 38.75; H, 3.53; B, 1.35; F, 4.74; I, 31.50; N, 12.19; O, 7.94. ESI-MS $[M+H]^+$: m/z 806,04. ^{1}H NMR (500 MHz, DMSO-d_6) δ 9.46 (s, 1H), 8.47 (d, J = 9.0 Hz, 1H), 8.04 (t, J = 5.6 Hz, 1H), 6.40 (d, J = 9.0 Hz, 1H), 3.49 (s, 2H), 3.20 (q, J = 6.5 Hz, 2H), 3.06 – 2.92 (m, 2H), 2.5 (s, 6H), 2.45 (s, 6H), 2.30 (t, J = 6.5 Hz, 2H), 1.90 – 1.70 (m, 4H). ^{13}C NMR (126 MHz, DMSO-d_6) δ 171.67 , 154.96 , 146.81 , 145.83 , 144.58 , 143.30 , 136.71 , 134.05 , 131.32 , 121.04 , 107.18 , 87.99 , 36.55 , 35.63 , 31.42 , 28.52 , 27.54 , 26.65 , 18.89 , 16.32

4-(4,4-Difluoro-2,6-diiodo-1,3,5,7-tetramethyl-4-bora-3a,4a-diaza-s-indacen-8-yl)- N-(-(7-nitrobenzo[c] [1,2,5]oxadiazol-4-il)propyl-(nitroso)amino)butanamide (4)

To a solution of **4a** (30 mg, 0.038 mmol) in THF:CH_3COOH (4:1 v/v; 20 mL) cooled at 0 °C with an ice bath, sodium nitrite (196.65 mg, 2.85 mmol) was added; the reaction mixture was stirred at 0 °C for 1 h and then at room temperature overnight. The obtained mixture was diluted with DCM and washed with saturated sodium bicarbonate solution (3 × 20 mL), dried over Na_2SO_4 and concentrated to dryness. Purification of the residue by flash chromatography, using $CHCl_3$:MeOH (98:2 v/v) as the eluent, gave the compound **4** as a pink solid (24 mg, resa 80%). Anal. Calcd (%) for $C_{26}H_{27}BF_2I_2N_8O_5$: C, 37.44; H, 3.26; B, 1.30; F, 4.56; I, 30.43; N, 13.43; O, 9.59. Found: C, 37.45; H, 3.25; B, 1.32; F, 4.58; I, 30.41; N, 13.39; O, 9.60. ESI-MS $[M+H]^+$: m/z 835.03. ^{1}H NMR (500 MHz, DMSO-d_6) δ 8.79 (d, *J* = 8.2 Hz, 1H), 8.01 (s, 1H), 7.90 (d, *J* = 8.2 Hz, 1H), 4.30 (dd, *J* = 8.5, 6.5 Hz, 2H), 3.32 (s, 12H), 3.07 (q, *J* = 6.5 Hz, 2H), 3.02 – 2.96 (m, 2H), 2.27 (t, *J* = 7.0 Hz, 2H), 1.76 (t, *J* = 8.6 Hz, 2H), 1.69 (q, *J* = 7.1 Hz, 2H). ^{13}C NMR (126 MHz, DMSO-d_6) δ 171.17 , 154.46 , 146.31 , 145.33 , 144.08 , 142.80 , 136.21 , 133.55 , 133.16 , 130.82 , 116.61 , 87.49 , 41.69 , 36.05 , 35.13 , 28.02 , 27.04 , 26.15 , 18.40, 15.82.

3.5.3 Photochemical characterization and NO release

The UV-Vis absorption spectrum of compound **4** (black line figure 47A) in methanol shows an intense absorption band at 528 nm typical for the BODIPY chromophore and a less intense absorption band at 380 nm attributable to the NO donor moiety. These spectral features allow to excite simultaneously the individual components by using a broadband excitation source covering the Vis region in the interval between 400-570 nm and at the same time they permit to excite them selectively in order to investigate their photochemical properties. In order to study the NO release, a solution of compound **4** was excited in the blue region under air-equilibrated conditions (MeOH, [**4**] = 6,5 μM, λ_{exc} =405 nm) and the absorption

spectral changes have been reported in figure 47A. They show the bleaching of the absorption band at 385 nm and the formation of a new absorption band at 475 nm which are indicative of the release of NO. The spectrum at the end of the photolysis is identical to that of the corresponding non nitrosate compound **4a**.

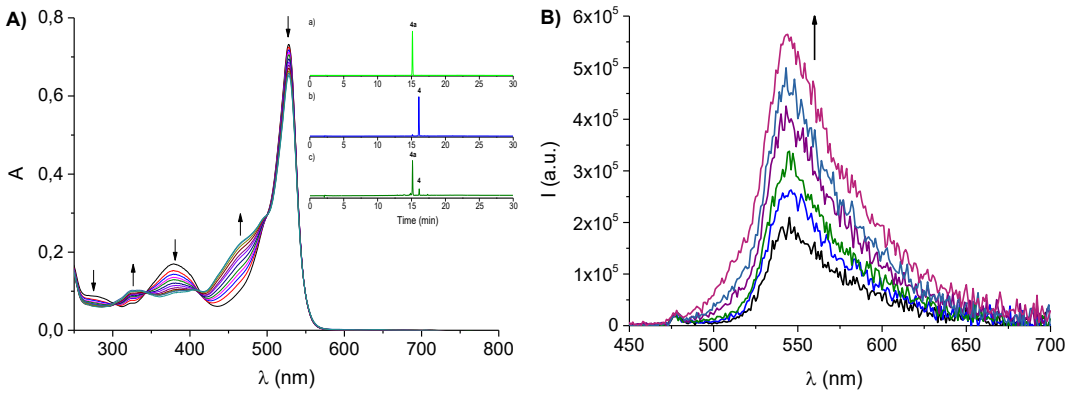

Figure 47. A) Absorption spectral changes observed upon exposure of a solution of **4** (6.5 µM) at λ_{exc} = 405 nm for time intervals from 0 to 240 s. MeOH, T = 25 °C. The arrows indicate the course of the spectral profile with the illumination time. The inset shows the HPLC traces related to solutions of a) **4a,** b) **4** and c) **4** after 120 s irradiation at λ_{exc} = 405 nm. T = 25 °C. B) Evolution of the fluorescence emission spectra corresponding to the sample of Figure 47A and recorded at λ_{exc} = 420 nm (isosbestic point).

Moreover, HPLC analysis carried out with the compound **4a** as reference confirmed this to be the only stable photoproduct (see inset Figure 47A). The quantum yield for the NO release is 0.18 ± 0.01, in good agreement with what observed for the only NO donor moiety and around one order of magnitude larger than that reported in literature for organic NOPD activatable with visible light. This value suggests that the NO photoreleasing properties are preserved even after binding with the photosensitizer and rules out any intermolecular communication between these two chromogenic centers. When the photolysis is performed under N_2-saturated conditions (data not shown), the photolysis profile and the kinetic behaviour are identical to that observed under air-equilibrated conditions, suggesting that NO

release is mediated by the short-lived excited singlet state which is not quenched by oxygen.

The hybrid shows a weak fluorescence emission when both the NOPD and the photosensitizer are selectively excited in the blue and in the green region, respectively. However, photodecomposition of **4** into **4a** leads to a significant revival of the fluorescence emission (figure 47B), like the one observed with NBF alone. This property makes **4a** an optical reporter to monitor the NO release in real time.

The excited triplet state of the PS is the precursor for the generation of $^1O_2$ [88]. Many PSs exhibit very intense triplet-triplet absorption in the visible region and lifetimes on the microseconds time regime. Therefore, laser flash photolysis with nanosecond time-resolution has been used to obtain direct spectroscopic and kinetic evidences on the population of this transient species. Figure 48A shows the transient absorption spectra of compound **4** obtained upon selective excitation of the BODIPY at 532 nm and recorded at different delay times after the initial laser pulse.

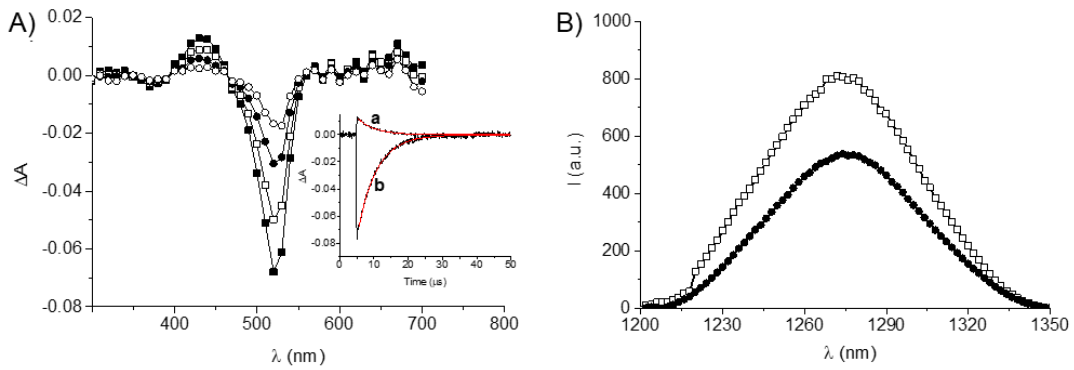

Figure 48. A) Transient absorption spectra observed 0.2 μs (■), 1 μs (□), 4 μs (●) and 8 μs (○) after 532 nm laser excitation (E532 ~ 10 mJ/pulse) of N_2-saturated solution of **4**. The inset shows the decay traces monitored at a) 440 nm and b) 520 nm and the related first-order fittings. [**4**] = 4 μM.MeOH, T = 25 °C. B) $^1O_2$ luminescence detected upon 532 nm light excitation of optically matched methanol solutions of **4** (●) and Bengal Rose (☐). T = 25 °C.

The spectrum taken at the shortest delay time shows a maximum at around 440 nm and bleaching at about 520 nm, this latter falling in the region of the ground state absorption of the BODIPY chromophore. These spectral features are in line with the typical triplet-state absorption of BODIPY derivatives [89]. The spectral evolution with elapsing time reveals that no new transient species are formed concurrently with the triplet decay. The triplet state decays mono-exponentially with a lifetime $\tau \sim 3.8$ μs (inset Figure 48A, trace a) in excellent agreement with the complete recovery of the bleaching (inset Figure 48A, trace b).

$^1O_2$ formed by collisional energy transfer between the triplet state of BODIPY component and the surrounding molecular oxygen was detected and quantified directly by its typical phosphorescence in the near-IR spectral window, upon selective excitation of BODIPY moiety with green light. Figure 48B shows the luminescence signals observed for optically-matched solutions of the compound **4** and Bengal Rose used as a standard ($\Phi_\Delta = 0.79$) [90]. A value of $\Phi_\Delta = 0.49 \pm 0.05$ was obtained; it which in good agreement with the typical values exhibited by BODIPY derivatives [91] and suggests that the functionalization of the BODIPY with the NOPD appendage does not affect its $^1O_2$ photosensitization capability.

3.5.4 Spectroscopic and photochemical properties in polymeric NPs

The hybrid **4** is not soluble in water. In view of its biomedical application, it was explored the use of mPEG-PCL nanoparticles (NPs) as biodegradable delivery system. mPEG-PCL is expected to provide more or less ordered core-shell structures with a PCL core surrounded by PEG chains depending on polymer hydrophilic/lipophilic balance and experimental conditions adopted to form NPs.

The hybrid was quantitatively entrapped in monodispersed mPEG-PCL NPs by nanoprecipitation. The colloidal properties of NPs-**4** reported in Table 1 are similar to those of the empty counterpart except for the zeta potential ζ which is lower in NPs-**4**. To elucidate this aspect mPEG-PCL micelles were prepared through dialysis, a technique generally promoting the formation of perfect core-shell nanostructures. The size of micelles was ca. 30 nm, roughly a half of that observed for both NPs-**4** and NP unloaded. Therefore, the nanoprecipitation method results in NPs where PEG chains are partly located also in the lipophilic PCL core [92]. The entrapment of the lipophilic hybrid **4** within the lipophilic PCL core encourage PEG chains to locate on the NPs surface leading to a decrease of the ζ potential in NPs-**4**.

Table 1. Properties of NPs-**4**. Results are reported as the mean of three separate measurements on three different batches ± SD. [a]mg of **4** per 100 mg of NPs. [b] Actual loading/theoretical loading %.

	NPs-4	***Empty***
Actual Loading (%)[a]	1.0	-
Encapsulation Efficiency (%)[b]	99.7 ± 0.01	-
Hydrodynamic diameter -D_H (nm ± SD)	66.2 ± 0.8	73.2 ± 6.3
Polydispersity Index-PdI	0.1	0.1
Zeta potential– ζ (mV ± SD)	-11.7 ± 2.6	-6.2 ± 2.2

Irradiation of water dispersion of the loaded NPs leads to the same absorption spectral changes observed with the free hybrid **4**, indicating the NO release from the N-nitroso moiety (Figure 49A). The NO release was unequivocally confirmed by its direct detection through an amperometric technique using an ultrasensitive electrode (inset Figure 49A). Moreover, the fluorescence emission significantly increases upon light irradiation (Figure 49B), confirming the formation of the photoproduct **4a** which represents a good optical reporter for the NO release. The

polymeric environment doesn't affect the nature of the photoreaction but it increases the efficiency of the NO generation. A value of Φ_{NO} = 0.92 ± 0.03 was observed under these conditions; this value is ca 5-fold higher than that observed for the free hybrid. Such an enhanced photoreactivity is the result of the active role played by polymeric network which provides easily abstractable hydrogens close to the anilinyl radical intermediate involved in the NO photorelease mechanism.

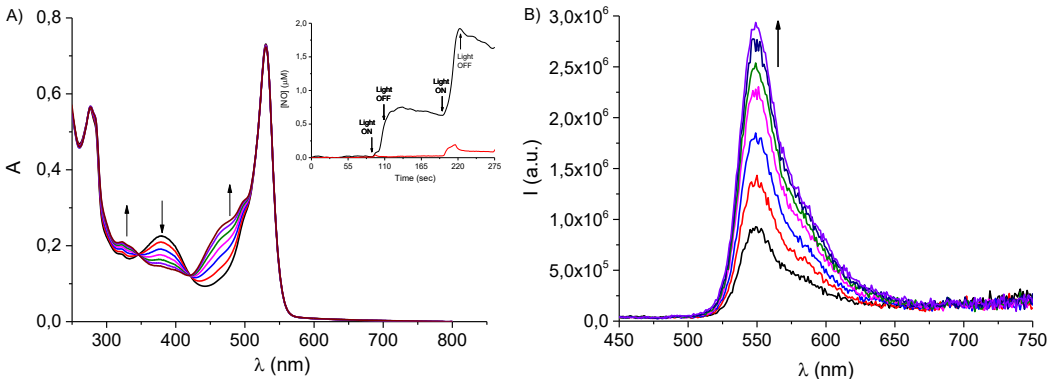

Figure 49. A) Absorption spectral changes observed upon exposure of an aqueous suspension of PEG-PCL NPs (0.83 mg mL^{-1}) loaded with **4** (16 μM) at λ_{exc} = 405 nm for time intervals from 0 to 40 s. The arrows indicate the course of the spectral profile with the illumination time. The inset shows the NO release profiles observed for the same NPs-**4** (black line) and for the empty NPs (red line) upon alternate cycles of light λ_{exc} = 405 nm. B) Evolution of the fluorescence emission spectra corresponding to the sample as in A and recorded at λ_{exc} = 420 nm (isosbestic point). T = 25 °C.

The triplet state of BODIPY unit of **4** was populated also in the presence of the polymeric network. The results of the laser flash photolysis experiment show that, analogously to the free hybrid **4**, the evolution of the absorption with the elapsing time reveals no additional transients formed concurrently to the triplet decay, excluding any possible bimolecular reaction of the species with the polymer (Figure 50A). The triplet dynamic followed a biexponential behavior characterized by a dominant component with $\tau_1 \sim$ 30 μs, more than one order of magnitude longer than that observed in the organic solvent, and a minor, faster component with $\tau_2 \sim$

3μs (inset Figure 50A). The lengthening of the triplet lifetime observed is quite common for chromophores hosted in nanocarrier systems and is usually related to the protection exerted by the host cage against external quenching impurities, to a perturbation of the inter-system crossing process to the ground state, or both [93].

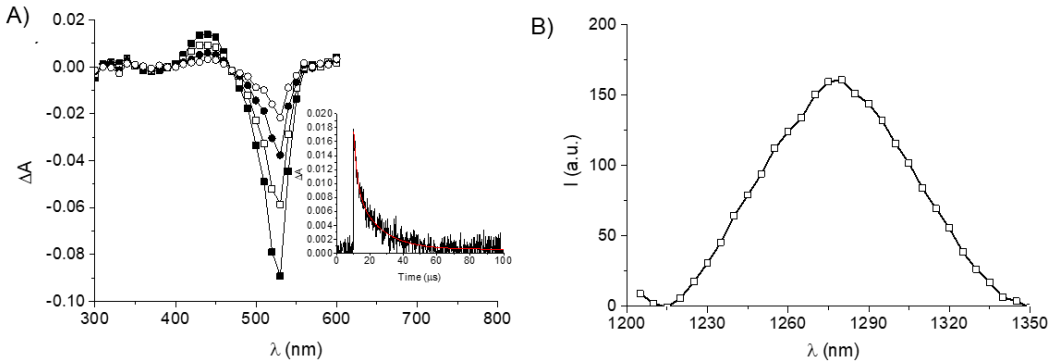

Figure 50. A) Transient absorption spectra observed 0.2 μs (■), 3 μs (□), 30 μs (●) and 50 μs (○) after 532 nm laser excitation (E_{532} ~ 10 mJ/pulse) of N_2-saturated aqueous suspension of mPEG-PCL_NPs (0.33 mg mL^{-1}) loaded with **4** (4 μM). The inset shows the decay traces monitored at 440 nm and the related bi-exponential fitting. T = 25 °C. B) $^1O_2$ luminescence detected upon 532 nm light excitation of a D_2O suspension of mPEG-PCL_NPs (0.33 mg mL^{-1}) loaded with **4** (4 μM). T = 25 °C.

Energy transfer from the triplet of **4** hosted in the NPs to molecular oxygen results in the photogeneration of $^1O_2$ (Figure 50B). However, despite the effective triplet population, a value of $\Phi_\Delta = 0.16 \pm 0.02$ was observed under these conditions, which is ca. 3-fold lower than that of the free **4**. Such a lower value is attributable to a shielding effect by the NPs from the external environment, especially from oxygen [94]. This hypothesis was well supported by the value of the quenching constant of the triplet state by molecular oxygen, $k_q(O_2)$. Indeed, in contrast to what was observed for the free **4**, the value obtained in the presence of NPs was well below the diffusional limit, being ca. 8.5×10^8 M^{-1} s^{-1}.

3.5.5 Biological evaluation

The NPs stability in the experimental conditions used for the cell studies was assessed by combining the Förster Resonance Energy Transfer (FRET) technique and the evaluation of the size distribution. This combination allows to monitor NPs disassembly and progressive time-dependent degradation both in vitro and in vivo [95]. The hydrophobic dyes DiO ($\lambda_{exc/em}$ is 488/505 nm) and DiL ($\lambda_{exc/em}$ at 543/575 nm) were selected as donor and acceptor chromophores since the DiO emission spectrum well overlaps with the DiL absorption spectrum ensuring an efficient energy transfer when the donor/acceptor couple is spatially located within the Föster radius. Figure 51A reports the emission spectra of NPs loaded with DiO/DiL (FRET-NPs), dispersed in DMEM high glucose and incubated at 37 °C for 0 and 4 h (this latter is the incubation time set for the cell studies).

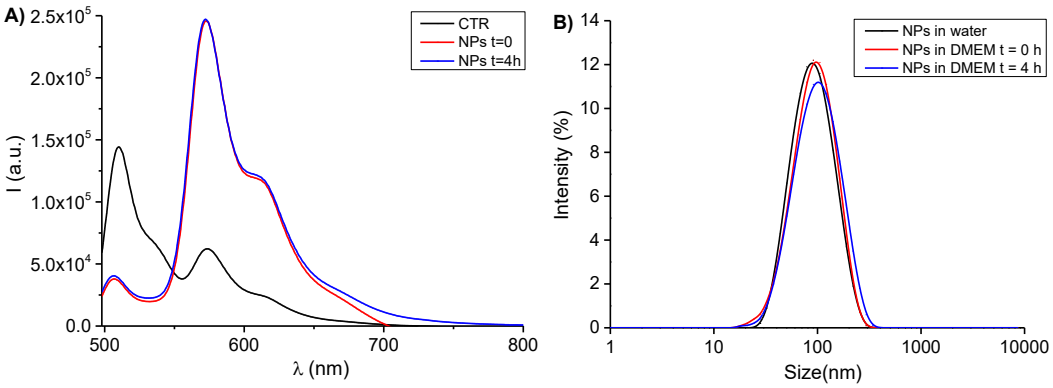

Figure 51. Stability of NPs-**4** in the conditions adopted for cell studies. A) Time evolution of emission spectra of FRET-NPs dispersed in DMEM high glucose after DiO excitation (λ_{ex} = 488 nm). As a control (CTR), the emission spectrum of NPs dissolved in THF is shown. B) The size distribution curves of NPs-**4** in DMEM high glucose. FRET-NPs concentration was 0.8 mg/mL.

Upon excitation of FRET-NPs in water at λ_{exc} = 488 nm, DiO emission at 505 nm is quenched and DiL emission is enhanced due to FRET occurring between the donor and the acceptor (blue line Figure 51A). When NPs are dissolved in tetrahydrofuran

(CTR in Figure 51A), DiO emission is restored, and DiL emission is depressed since no FRET occurs. The perfect overlap of NPs emission spectra at 0 and 4 h demonstrate that the formulation maintains its structural integrity in the conditions adopted for cell studies. Furthermore, the size distribution of the NPs is unaltered upon 4 h incubation (inset figure 51B).

The low green fluorescence emission of hybrid **4** was adequate to monitor its uptake in hepatocellular Hep-G2 cells. As evident from the fluorescence images reported in Figure 52A, both the free hybrid **4** and NP-**4** are internalized by cells after 4 h of treatment and mainly localized in the cytoplasm. The amount of NPs internalized is ca. 5% of the applied dose, which is consistent with values observed for PEGylated nanoplatforms [96].

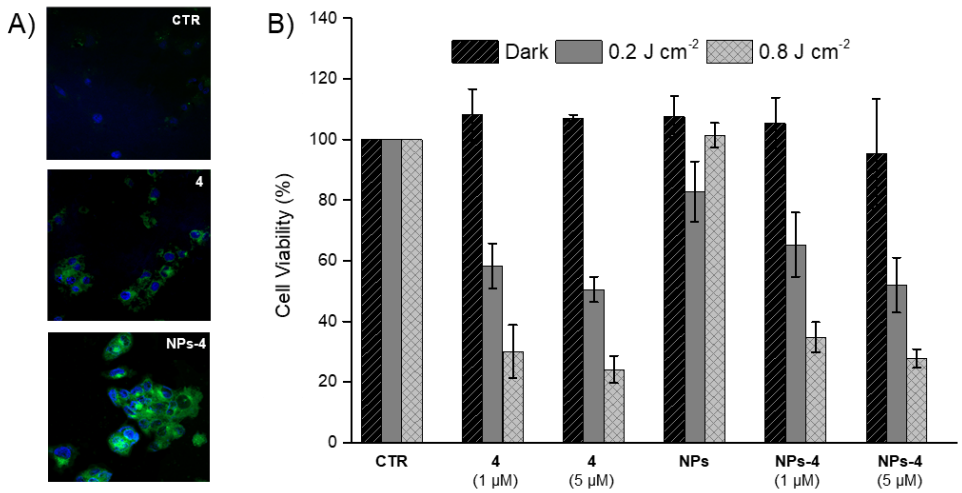

Figure 52. *A*) Fluorescence images of Hep-G2 cells incubated 4 h with **4** and NPs-**4** ([NP-**4**]= 0.42 mg/mL, [**4**]= 5 µM). Nucleus stained with DAPI (Blue); compound **4** (Green). (B) Cell viability of HepG2 cancer cells incubated 4 h with **4** and NP-**4** and either kept in the dark or irradiated with Vis light in the range 400-570 nm.

The biological activity was evaluated against hepatocellular carcinoma HepG2 cell lines. The free compound was tested as DMSO solution and its formulation in the polymeric NPs as aqueous suspension. Both groups of samples were tested at the

two different concentrations of 1-5 µM in the dark and upon irradiation with visible light using a Xenon lamp with a cut-off filter at 400 nm. This irradiation source has a constant intensity in the range 400-570 nm and ensure the excitation of both the NOPD and the BODIPY units of **4**, permitting the simultaneous generation of the cytotoxic species $^1O_2$ and NO. As illustrated in figure 52B, compounds **4** is well tolerated in the dark by the cancer cells both in the free form and when delivered by NPs. Besides, the empty NPs did not elicit significant changes in cell viability both in the dark and upon light irradiation. However, it induces a good level of cell mortality at both concentrations used. The photodynamic action of **4** delivered through the polymeric NPs is basically comparable to that obtained for the free compound incubated as DMSO solution.

3.5.6 Conclusions

A novel molecular hybrid for bimodal photodynamic action has been developed. This compound is able to simultaneously generate $^1O_2$ and NO under Vis light excitation with quantum yield on the same order of magnitude. This feature allows to generate these two unconventional anticancer agents in comparable amount without the need of double excitation light sources with different intensities or concentration of NOPD larger than the PS. A photodynamic action is observed towards hepatocarcinoma cell lines at low light doses. Furthermore, the hybrid produces a highly fluorescent stable photoproduct upon irradiation, which can act as an optical reporter for the NO released. This multifunctional molecular dyad has been encapsulated in biodegradable mPEG-PCL polymeric NPs which are stable in biological fluid and are able to deliver the photoactivatable cargo into cancer cells without precluding its effective bimodal photodynamic action.

Chapter 4

General conclusion

The present project has contributed to develop new solutions in the field of "unconventional" therapies based on the photoregulated generation of nitric oxide as intriguing alternative to those based on the "conventional" anticancer drugs. Novel classes of NOPD have been developed. Each of these hybrids present unique features and all of them work under activation with visible light which is the perfect trigger for the controlled production of such reactive species. Moreover, the novel NOPDs present the additional advantage of fluorescent emission, an useful tool in view of image-guided NO-based phototherapies. For the well-known properties of reactive species and on the bases of the first preliminary biological studies performed in vitro, we think that the novel hybrids are promising and eligible for further studies.

Chapter 5

Materials and methods

Chemicals. All solvents and chemicals used were of spectrophotometric grade and were purchased from Sigma Aldrich or TCI and used without further purification, included Pluronic® P123 (PEO_{20}–PPO_{70}–PEO_{20}, MW ca. 5.750 g mol^{-1}), Pluronic® F127 (PEO_{100}–PPO_{70}–PEO_{100}, MW ca 12.600 g mol^{-1}) and PEG_{5K} -PCL_{5K}. The concentrations of ct-DNA, in base pair (bp), was determined by absorption spectroscopy, using a molar extinction coefficient of 13,200 M^{-1} cm^{-1} at 260 nm [97].

Cell culture. Cell culture medium and supplements were purchased from Life Technologies (Italy), while sterile plasticwares were from Falcon® (Corning, USA). Dulbecco's modified Eagle's medium (DMEM), fetal bovine serum (FBS) and antibiotics were purchased from Gibco Life Technologies (Milan, Italy). BODIPY® FL C5-ceramide and ER-TrackerTM Green were from Molecular Probes (Life Technologies). The CellTiter96 Aqueous One Solution Cell Proliferation Assay (MTS) was from Promega Co. (Madison, USA).

All the cancer cell lines used for the present work (MCF-7, MDBA-MB-231, HeLa and HepG2) were purchased from American Type Culture Collection (ATCC, Rockville, USA). The cells were grown in DMEM with Glutamax™ supplemented with 10% heat inactivated fetal bovine serum (FBS), 100 U/mL streptomycin, 100 µg/mL

penicillin G and maintained at 37 °C under a humidified atmosphere containing 5% CO_2.

Instrumentation: ^{1}H-NMR and ^{13}C-NMR spectra were recorded on Varian 200, Varian UNITY Inova 500 MHz or Jeol NMR spectrometer 600 MHz. Chemical shifts (δ) are given in parts per million (ppm). The following abbreviations are used to designate the multiplicities: s = singlet, bs = broad singlet, d = doublet, t = triplet, q = quartet, quin = quintet, m = multiplet. Mass spectra were recorded on a Micromass Quattro microTM API (Waters Corporation, Milford, MA, USA) with electrospray ionization. Flash column chromatography was performed on silica gel (Merck Kieselgel 60, 230-400 mesh ASTM). The progress of the reactions was followed by thin layer chromatography (TLC) on 5×20 cm plates with a layer thickness of 0.2 mm. The purity of target compounds and the monitoring of the photodegradation reactions were performed with an HP 1100 chromatograph system (Agilent Technologies, Palo Alto, CA, USA). equipped with a quaternary pump (G1311A), a membrane degasser (G1379A), a diode-array detector (DAD) (G1315B) integrated in the HP1100 system. Data analysis were processed by HP ChemStation system (Agilent Technologies). The analytical column was a LiChrospher® 100 C18-e (250×4.6 mm, 5µm) (Merck KGaA, 64271 Darmstadt, Germany) eluted with CH_3CN/H_2O 0.1% TFA in a ratio depending on the characteristics of the compound. All compounds were dissolved in the mobile phase at a concentration of about 0.1 mg/ml and injected through a 20 µL loop. UV signals were recorded at different wavelength depending on the absorption spectrum of the compounds (with 800 nm as reference wavelength). Melting points (mp) were determined with a capillary apparatus (Büchi 540).

UV/vis absorption spectra were recorded in a quartz cell with a 1.0 cm path length and 3 mL capacity or a specific holder for thin films on a Jasco V 650 spectrophotometer or on Perkin Elmer spectrophotometer (mod. Lambda 365).

Fluorescence emission spectra were performed with Fluorolog-2 (Model, F111) spectrofluorimeter in right angle mode for solution. Fluorescence lifetimes were recorded with the same spectrofluorometer equipped with a TCSPC Triple Illuminator. Solutions were excited by a Nanoled pulsed diode excitation source at 455 nm or 370 nm. The system measured fluorescence lifetimes with a resolution >200 ps. The multiexponential fit of the fluorescence decay was obtained using the equation 13:

$$I(t) = \Sigma\alpha_i \exp(^{-t/\tau i}) \qquad (13)$$

Hydrodynamic diameter (DH), polydispersity index (PdI) and zeta potential (ζ) of the were measured on a Zetasizer Nano ZS (Malvern Instruments Ltd, Malvern, UK).

Laser flash photolysis: All of the samples were excited with the second harmonic of a Nd–YAG Continuum Surelite II-10 laser (532 nm, 6 ns FWHM), using quartz cells with a path length of 1.0 cm. The excited solutions were analyzed with a Luzchem Research mLFP-111 apparatus with an orthogonal pump/probe configuration. The probe source was a ceramic xenon lamp coupled to quartz fibre-optic cables. The laser pulse and the mLFP-111 system were synchronized by a Tektronix TDS 3032 digitizer, operating in pre-trigger mode. The signals from a compact Hamamatsu photomultiplier were initially captured by the digitizer and then transferred to a personal computer, controlled by Luzchem Research software operating in the National Instruments LabView 5.1 environment. The solutions were deoxygenated via bubbling with a vigorous and constant flux of pure nitrogen (previously saturated with solvent). In these experiments, the solutions were renewed after

each laser shot (in a flow cell with a 1 cm optical path), to prevent photodegradation. The sample temperature was 295 ± 2 °K. The energy of the laser pulse was measured at each shot with a SPHD25 Scientech pyroelectric meter.

Singlet oxygen detection: The NIR luminescence of $^1O_2$ was registered with the same spectrofluorometer as above equipped with a NIR-sensitive liquid nitrogen cooled photomultiplier, exciting the air-equilibrated samples with an external continuum laser source. $^1O_2$ quantum yields were determined at λ_{exc} = 532 nm using optically-matched solutions at the excitation wavelength of compounds **4** and NPs-**4** and Rose Bengal in methanol as standard (Φ_Δ= 0.79) [90]. The values of Φ_Δ were determined from the following equation:

$$\Phi_\Delta = \Phi_{\Delta(s)} \times (I/I_{(s)}) \times (\tau_{(s)}/\tau) \quad (14)$$

where $\Phi_{\Delta(s)}$ is the $^1O_2$ quantum yield of the standard, I and $I_{(s)}$ are the areas of the phosphorescence emission spectra of **4** or NPs-**4** and the standard, respectively, and $\tau_{(s)}$ and τ are the $^1O_2$ phosphorescence lifetimes in the reference and the sample solvents.

Photolysis experiment and NO photorelease quantum yield. Irradiation was performed in a thermostated quartz cell (1 cm pathlength, 3 mL capacity) under gentle stirring. The photolysis experiments under anaerobic conditions were performed deoxygenating the solution by bubbling with a vigorous and constant flux of pure nitrogen (previously saturated with solvent).

The photodegradation quantum yield, Φ_{NO}, was determined at λ_{exc} used, within 20% photo-transformation of the compounds by using equation 15:

$$\Phi_{NO} = [\text{Photocage-NO}] \times V/t \times (1–10^{-A}) \times I \quad (15)$$

where [Photocage-NO] is the concentration of the phototransformed compound, V is the volume of the sample, t is the irradiation time, A is the average absorbance of the sample at the excitation wavelength and I is the intensity of the excitation light source. The concentration of the phototransformed compounds were determined spectrophotometrically, and I was calculated by potassium ferrioxalate actinometry.

Amperometric NO detection: NO release was measured with a World Precision Instrument, ISO-NO meter, equipped with a data acquisition system, and based on direct amperometric detection of NO with short response time (< 5 s) and sensitivity range 1 nM – 20 µM. The analog signal was digitalized with a four-channel recording system and transferred to a PC. The sensor was accurately calibrated by mixing standard solutions of $NaNO_2$ with 0.1 M H_2SO_4 and 0.1 M KI according to the reaction:

$$4H^+ + 2I^- + 2NO_2^- \rightarrow 2H_2O + 2NO + I_2$$

Irradiation was performed in a thermostated quartz cell (1 cm path length, 3 mL capacity) under gentle stirring and under continuum laser light at different λ_{exc}.

Chemical Detection of NO and NO_2^- analysis. NO release was also measured indirectly by means of the well-known, highly sensitive (detection limit on the order of the picomoles) fluorimetric bioassay of Misko et al. [79] based on the ring closure of the nonfluorescent DAN with nitrite to form the highly fluorescent product. Aliquots of 2 mL of solutions of compound **3** were irradiated with the red laser or kept in the dark. Afterwards, the samples were dried under vacuum, resuspended in 2 mL of water and filtered with a 0.2 µm GHP Acrodisc membrane filter. The filtered solution was added of 200 µL of DAN solution (DAN 0.30 M in 0.62 M HCl)

and stirred for 20 min at room temperature. 300 µL of NaOH 3 M was then added to the previous solution and stirred for 20 min at room temperature. The resultant solution was put into the fluorescent cuvette and the fluorescence emission and excitation spectra were recorded at λ_{exc} = 360 nm and λ_{em} = 405 nm, respectively. A standard calibration curve was carried out by using freshly prepared solutions of sodium nitrite in a phosphate buffer 10 mM at pH 7.4.

NO_2^- were quantitatively evaluated by the Griess assay [80]. A 50 µM solution of compound **3** in MeOH:PB (1:1 v/v) was prepared and this solution was irradiated for 30 minutes using the white LED. After 30 minutes, 0.5 mL aliquots of the irradiated solution were treated with 125 µL of the Griess reagent (4% w/v of sulphanilamide, 0.2% w/v of N-naphthylenylenediamine dihydrochloride, 1.47 M of phosphoric acid); after 10 minutes at room temperature, the sample was analyzed with RP-HPLC to detect the azo dye. The sample was eluted on a HyPURITY Elite C18 column (250 × 4.6 mm, 5 µm, Hypersil, ThermoQuest Corporation, UK). The injection volume was 20 µL (Rheodyne, Cotati, CA). The mobile phase consisting of acetonitrile 0.1% TFA (solvent A) and water 0.1% TFA (solvent B) at flow-rate = 1.0 mL/min with gradient conditions: 50% A until 4 min, from 50 to 90% A between 4 and 8 min, 90% A between 8 and 12 min, and from 90 to 50% A between 12 and 15 min. The column effluent was monitored at 540 mn referenced against a 800 nm wavelength. The values obtained from integration of the peak of azo dye were interpolated in a calibration curve obtained using standard solutions of sodium nitrite at 0.5 µM to 50 µM (r2 =0.996). The yield in nitrite was expressed as percent NO_2^- (mol/mol, relative to the initial compound concentration) ± SEM. The percentage of NO_2^- released was evaluated with respect to the amount of compound initially present in the irradiated solution. The total amount of NO_2^- and NO_3^- to nitrite was evaluated with a procedure adapted from the method of Miranda et al [98]. A 50 µM solution of compound **3** in MeOH/PB 1/1 was prepared

and this solution was irradiated for 30 minutes using the white LED. After 30 minutes aliquots of 0.5 mL of the irradiated solution was treated with 125 µL of VCl_3 solution (400 mg of VCl_3 dissolved in 50 mL of 1 M HCl) and 125 µL of the Griess reagent; after 30 minutes of stirring at room temperature the sample was analyzed with RP-HPLC to detect the azo dye. The values obtained from integration of the peak of azo dye were interpolated in a calibration curve obtained using standard solutions of sodium nitrite at 0.5 µM to 50 µM (r^2 =0.996). The yield in nitrite was expressed as percent NO_2^- (mol/mol, relative to the initial compound concentration) ± SEM. The percentage of NO_2^- released was evaluated with respect to the amount of compound initially present in the irradiated solution.

$ONOO^-$ assay. $ONOO^-$ were revealed by using the very sensitive and selective method recently developed by Radi et al [81]. A 25 µM solution of the compounds **3** or **3a** were irradiated in the presence of equimolar amount of Fl-B with the red continuum laser at different times. Afterwards the fluorescence emission and excitation spectra were recorded. Quantitative comparison between compound 3a and the fluorescein generated were performed after 30 minutes of irradiation of a 25 µM solution of compound 3 in the presence of equimolar amount of Fl-B using the white LED. The irradiated solution was analyzed with RP-HPLC to detect the fluoresceine and compound **3a** obtained. The sample was eluted on a Zorbax Eclipse XDB-C18 column (150 × 4.6 mm, 5 µm, Agilent Technologies). The injection volume was 20 µL (Rheodyne, Cotati, CA). The mobile phase consisting of CH_3CN 0.1% TFA (solvent A) and H_2O 0.1% TFA (solvent B) at flow-rate of 1.0 mL/min with gradient conditions: 30% A until 5 min, from 30 to 90% A between 5 and 15 min, 90% A between 15 and 17 min, and from 90 to 30% A between 17 and 20 min. The signals were obtained on fluorescence using an excitation and emission wavelength of 492 nm and 515 nm, respectively (gain factor = 10). The values obtained from

integration of the peak of Fluoresceine were interpolated in a calibration curve obtained using standard solutions of Fluoresceine from 1 to 25 µM (r^2 =0.999).

$O_2^{\bullet-}$ assay. Dihydrorhodamine123 (DHR123) was used as the superoxide anion radical probe [69a]. Compound **3a** and DHR123 were prepared as 10 µM in PB:MeOH (1:1 v/v). Then the cuvette was exposed to 670 nm monochromatic light for different time and the fluorescence spectra were recorded immediately after each irradiation. As control, DHR123 in the same solvent without compound **3a** was used and no increase of fluorescence was observed upon the same irradiation times.

Fluorescence Quantum Yields: Fluorescence quantum yields (Φ_f) were determined using optically matched solutions at the excitation wavelength, of hybrids and of standards through the following equation:

$$\Phi_f = \Phi_{f(s)} (In^2/I_{(s)}n^2_{(s)}) \qquad (15)$$

where $\Phi_{f(s)}$ is the fluorescence quantum yield of the standard; I and $I_{(s)}$ are the areas of the fluorescence spectra of compounds and standard, respectively; n and $n_{(s)}$ are the refraction index of the solvents used for compounds and standard. Absorbance at the excitation wavelength was less than 0.1 in all cases.

Lipophilicity studies. n-octanol–water partition coefficients were quantified using a miniaturized shake-flask approach based on OECD 107 [99]. To investigate the analytes in the ionized state occurring in vitro, measurements were performed using 0.1 M phosphate buffer at pH 7.4. Buffer solution was saturated with n-octanol (W_o) prior to analysis and vice versa (O_w) by vigorous shaking and rest for

24 h to get spontaneous separation. Stock solutions (1 mL) of DOX and compound **2** (0.5 mg/mL) prepared in O_w or W_o, respectively, were added with the second phase, vortexed for 1 min and then shaken for 2 h (125 rpm) at room temperature (25 ± 3 °C) to reach equilibrium and phase distribution. Following phase separation through centrifugation (2900 x g, 5 min), the aqueous or n-octanol phases were analyzed separately by UV-vis spectrophotometry at 490 nm after dilution to obtain an OD around 0.5. Lipophilicity of the compounds (Log $D_{7.4}$) was derived from the difference in the blank corrected OD from the reference stock solution (OD_{ref}) and that in the partitioned samples (OD_{part}) by Log $D_{7.4}$=Log (OD_{ref}/ OD_{part} – 1).

Binding studies with BSA. The protein concentration has been determined spectrophotometrically using the extinction coefficient of 36.500 M^{-1} cm^{-1} at 280 nm. 3 mg of compound **2** were dissolved in 500 µL of DMSO to obtain a stock solution 6 mM. Titration was carried out by successive addition of this stock solution (from 0 to 80 µM) to a 2.5 mL of a solution of BSA in TRIS-HCl buffer pH 7.4 at 25 °C. The final solutions were left under stirring in the dark for 15 minutes before recording the absorption and emission spectra.

Evaluation of the biological activity.

Expression of MDR-pumps. Expression of MDR-related pumps in cells was assessed by flow cytometry using the EFLUXX-ID® Green Multidrug Resistance assay kit (Enzo Life Sciences, Italy) and following manufacturer's instructions. This assay allows an evaluation of MDR1 (p-glycoprotein), MRP1/2, BCRP expression on cell membrane calculated as MDR Activity Factor (MAF) by measuring cell retention of the EFLUXX-ID reagent, a substrate of MDR pumps. Briefly, $5x10^5$ cells/sample were incubated for 5 min with verapamil (5 mM), MK-571 (10 mM) and novamicin (50 mM) in order to inhibit MDR1, MRP1/2, BCRP, respectively, before adding the EFLUXX-ID reagent

for 30 min at 37 °C. At the end of incubation time, cells were centrifuged, resuspended in Versene and analyzed by the flow cytometer (BD LSR Fortessa™ X-20), recording EFLUXX-ID reagent fluorescence in the FITC channel. MAF of each MDR pump was calculated as:

$$MAF = (F_i - F_0)/F_i \times 100 \qquad (16)$$

where F_i is the value of the sample pre-treated with pump inhibitors, F_0 the fluorescence of the sample incubated only with the EFLUXX-ID reagent. When MAF>25 for a certain pump, the cell line is considered MDR-positive.

Intracellular uptake studies. Cellular uptake was measured by flow cytometry. Cells were grown in 24-well plates for 24 h and incubated for different interval times in cell culture medium added with 10% serum. After incubation the cells were washed twice with Versene, detached from the plates with trypsin that was neutralized by the addition of FBS. Cells were centrifuged and resuspended in Versene before measuring the hybrid fluorescence using a BD LSR Fortessa™ X-20 flow cytometer. A blue laser at 488 nm was used to excite the fluorophore; for each sample 10^5 events were acquired and analyzed using the FACSDiva software.

Flow cytometry was used also to measure the capacity of cells to extrude the drug. Cells were seeded as described above and pretreated or not with the MDR1 selective inhibitor Verapamil (50 μM) for 1 h before adding the tested drug.

Intracellular localization studies. The intracellular localization of compound **2** and **3** was evaluated by confocal microscopy. Cells were grown in 35 mm imaging dishes (Eppendorf AG, Hamburg, Germany) for 24 h and incubated for different time intervals with the tested drug. Fifteen minutes before completing the incubation, cells were stained with Hoechst-33342, BODIPY® FL C5-ceramide, ER-TrackerTM Green, used as probes for nucleus, Golgi apparatus and endoplasmic reticulum,

respectively. Cells were then washed twice with HBSS and observed with a Leica SP5 confocal microscope; acquired images were analyzed using ImageJ software.
For compound **4** and NPs-**4,** Hep-G2 cells were incubated with NPs-**4** at 80, 420 or 800 μg/mL, corresponding to 1, 5 and 10 mM of **4**, respectively. After 4 h of incubation at 37 °C in the dark, cells were washed. The coverslips were mounted on microscope slides (Epredia, Braunschweig, Germany) by using the UltraCruz Hard-set mounting medium with 4',6-diamidino-2-phenylindole (Santa Cruz Biotechnology, Dallas,TX) and analyzed under a laser confocal microscope (Zeiss LSM 700 Confocal Laser Scanning Microscope equipped with Argon (488 nm) and HeNe (561, 639 nm) lasers and a 40X/1.2 NA objective).

Intracellular quantification of NO. In order to measure the extent of NO released intracellularly, the probe DAF-FM^{TM} diacetate (Thermo Fisher Scientific) was used. Cells were seeded as for phototoxicity experiments and incubated for 2 h with 10 or 25 μM compound **2** or DOX. At the end of incubation time cells were stained for 20 min with 10 μM of DAF-FM probe and irradiated with green light (72 J/cm^2). After irradiation, cells were rinsed with HBSS and released for 20 min in fresh medium in the dark before reading DAF-FM fluorescence with a Victor3^{TM} 2030 Multilabel Reader (Perkin Elmer) using the FITC channel. Fluorescence of DAF-FM in treated cells was expressed as fold changes with respect to the fluorescence signal measured in controls and set equal to 1.

Evaluation of MDR1 inhibition. The NO capacity to inhibit MDR1 in MDA-MB-231 cells was measured using the EFLUXX-ID® kit. Briefly, 0.5 x 10^6 cells were allowed to growth in 50 mm dishes for 24 h, were treated for 2 h with 2.5 μM DOX or compound **2** before being exposed or not to green light (72 J/cm^2). Cells were then detached from plates with trypsin, centrifuged and resuspended in medium added

with the EFLUXX-ID reagent for 30 min and analyzed by flow cytometry as described above.

Dark and photo-toxicity of compound 2 and 3. The cytotoxicity of compound **2** and compound **3** was measured with the MTS assay (Cell- Titer 96® Aqueous One Solution Cell Proliferation Assay, Promega Co., USA) according to manufacturer's instructions. 8×10^3 cells/well were seeded in 96-well plates and, after 24 h of growth, treated for 2 h with increasing drug concentrations (1-10 µM for compound 2 and free DOX; 0.1-2 µM for compound 3). To evaluate cytotoxicity in the absence of irradiation (dark cytotoxicity), at the end of the 2 h of drug exposure, cells were release in drug-free medium for further 24 h before assessing cell viability. Indeed, for phototoxicity experiments, drug treatment was removed, and cells washed twice with PBS added with Ca^{2+} and Mg^{2+}, before irradiating them (Green light for compound **2** and free DOX with a total dose of 72 J/cm^2, irradiation time 30 min, power density 40 mW/cm^2. Red light (600–800 nm) emitted from a Waldmann PDT 1200L lamp (Waldmann Medizintechnik, Germany) with a total light fluence of 1 J/cm^2; power density 40 mW/cm^2; irradiation time 25 seconds). At the end of irradiation, cells were released for additional 24 h in drug-free medium before measuring cell viability. For the MTS assay the medium was replaced with 100 µL of serum-free medium and 20 µL of the CellTiter 96® reagent. The samples were incubated for 60 min at 37 °C; the absorbance at 492 nm was measured with a Multiskan Go (Thermo Fischer Scientific, USA) plate reader and cell viability was expressed as a function of absorbance relative to that of control cells (considered as 100% viability).

Statistical analysis. The Primer software for biostatistics (McGraw-Hill, Columbus, OH, USA) was used for statistical analysis of the data. The data are expressed as

means ± standard deviations (SD) for at least three independent experiments, carried out in triplicate. The difference between two groups of treatments was evaluated by Student's test while the differences between more than two groups of treatment was evaluated with one-way ANOVA test with the Bonferroni's correction and was considered significant for $p < 0.05$.

Pluronic Mixed Micelles and Loading with NBF-NO or NBF. Empty micelles were prepared by thin-film hydration method [100]. Briefly, 40 mg of Pluronics (20 mg of P123 and 20 mg of F127) were dissolved in absolute ethanol (4 mL) in a round-bottom flask. Then, the solvent was evaporated by rotary evaporation (45 °C, 25 min) to obtain a solid matrix film. The film was left under vacuum overnight to remove residual solvent. After that, the dried film was hydrated with 4 mL of water and the material was sonicated (10 min) giving a micellar solution. A stock solution of loaded micelles was prepared by adding ca. 1 mg of solid either **NBF-NO** or **NBF** to the previously prepared empty micelles. This suspension was stirred for 2 h at room temperature and filtered (0.22 mm filters, RC Chemtek, Italy) to remove the unincorporated components or possible large cylindrical aggregates formed by P123. The actual concentration of the loaded drugs was optimized by dilution with the solution of empty micelles and determined by UV-vis spectrophotometry.

Preparation and characterization of NPs-4. Polymeric NPs were prepared by nanoprecipitation. Briefly, PEG_{5k}-PCL_{5k} (10 mg) and compound **4** (30 mM) were dissolved in 2 mL of tetrahydrofuran (THF), and the resulting solution was added dropwise in water (4 mL) under magnetic stirring through a syringe pump (1mL/min). After organic solvent evaporation at reduced pressure, the sample was filtered on an RC filter (0.20 mm).

NPs giving Förster Resonance Energy Transfer (FRET-NPs) were prepared analogously entrapping DiO ($\lambda_{ex}/\lambda_{em}$ = 488 and 505 nm) and DiL (λ_{ex} = 543 nm, λ_{em} = 575 nm) as FRET pair. In this case, 50 mL of THF solutions of DiO and DiL (1 mg/mL each) were added to 1.9 mL of a THF solution containing PEG_{5k}-PCL_{5k} (10 mg). The organic phase was nanoprecipitated in water, as reported above.

To evaluate the actual loading, NPs were centrifuged at 9000× g for 20 min through VIVASPIN® 6 (MW 5 kDa) and the eluate fluorescence emission intensity at nm (λ_{ex} = 510nm) was measured. A calibration curve of **4** was constructed in the concentration range 0.01-5 mg/mL (r^2= 0.99). Results are expressed as actual loading % (amount of drug in 100 mg of NPs %) and encapsulation efficiency (actual loading/theoretical loading %).

Stability of NPs and quantification of NPs internalization. The stability and the integrity of NPs in conditions mimicking cell experiments were investigated through size monitoring and FRET experiments. FRET-NPs were dispersed in DMEM high glucose without phenol red (0.8 mg/mL), and their emission spectra were collected at λ_{ex} = 488 nm at different time points (0 and 4 h). At the same time points, the size distribution was assessed.

To quantify NPs internalization, cells were incubated with 420 µg/mL of NP-**4** for 4 h and then the medium was collected, and the fluorescence emission at 546 nm was measured (λ_{ex} 470 nm). The percentage of NPs internalized inside cells was derived by the amount remaining in the medium. NPs were quantified based on the calibration curve of an NP-**4** dispersion in the cell medium in the concentration range of 20–420 µg/mL. The medium alone collected from untreated cells was used as a control.

Dark and phototoxicity of compound 4 and NPs-4. The 3-(4,5-dimethyl-2-thiazolyl)-2,5-diphenyl-2H-tetrazolium bromide (MTT) assay was applied to analyze cell viability both in dark condition and under visible light excitation for compound **4** and for NPs-**4**. Cells were seeded in 96-well flat bottom plates (ThermoScientific Nunc, Rochester, NY, USA) at a density of $1x10^4$ cells/well, and incubated for 48 hours to reach a confluency of 80%. Then, cells were exposed to free-compound, unloaded and loaded NPs. All samples were tested at 1 and 5 µM, and incubated for 4 hours. Untreated cells were maintained as control. After a wash, phenol red-free and FBS-free medium was added into each well. Some cell plates were kept in the dark, while the other ones irradiated by exposure to a 150 W Xe lamp through a cut-off filter at 400 nm for 5 and 20 seconds. Immediately after the irradiation, the treatment medium was changed by complete medium. After an overnight in standard cell culture conditions, the solution of MTT salts (Sigma-Aldrich, Milan, Italy) was added into each well and incubated for 3 hours at 37°C. Cell viability was linked to the conversion of the tetrazolium ring of MTT into formazan crystals by mitochondrial dehydrogenases of live cells. Formazan was solubilized in 100 µL of DMSO, and the absorbance measured at 570 nm with a microplate reader (AMR-100, Allsheng, Zhejian, China). Results were reported as percentage of viability versus untreated controls ± SD. Each test was repeated at least three times (n=3) in triplicate wells. Statistical analysis was carried out using GraphPad Prism software v. 7.00 (San Diego, CA) and performed by one-way analysis of variance (ANOVA) followed by Tukey's multiple comparisons test. Results were considered significant with a value of $p < 0.05$.

Conformational studies.

Conformational study on free 1. The molecular hybrid **1** was parameterized according to GAFF2 force field [101]. QM-fitted RESP charges [102] were calculated

at the HF/6-31G* level by RED server [103] using GAMESS-US [104], [after minimizing structure with MMFF94 [105] force field implemented in Open Babel] [106]. The molecule was solvated in a periodic TIP3P [107] water cubic box and neutralized with NaCl. The simulation was performed using NAMD 2.12 [108]. Long range electrostatic interactions were computed through the Particle Mesh Ewald (PME) algorithm [109]. Non-bonded interactions were calculated with a cut-off distance of 8 Å. Langevin dynamics with a damping coefficient of 1 ps-1 was used to control the temperature of the system (298 K). Constant pressure (1 atm) was maintained using the Nosé-Hoover Langevin piston method [110]. Well-tempered metadynamics simulation was carried out using Colvars module [111] implemented in NAMD 2.12. Newton's equation was integrated with a 1 fs-1 timestep. The representative structures were obtained through clustering the selected frames, using GROMACS 2016.4 [112]. The structure pictures were rendered using VMD 1.9.3 [113]. The system was minimized and equilibrated at 10 K for 0.15 ns in the NVT ensemble keeping heavy atoms of 5 fixed; then it was thermalized to 298 K during 0.1 ns and equilibrated at the same temperature for further 0.4 ns. After that it was finally equilibrated in the NpT ensemble for 0.5 ns. The well-tempered metadynamics simulation was then run for 80 ns. In order to describe the conformational behaviour of the molecule as collective variables were chosen the distance between the center of mass of pyridine-like ring of acridine moiety and the center of mass of nitro-aniline ring, and a torsional angle formed by C9, N10, C1' and C4' S8. The hill width was 0.25 Å for distance collective variable and 2.5 rad for dihedral collective variable; the hill height was 0.05 kcal mol^{-1} ; hills were updated every 50 fs; the bias temperature was set to 1200 °C. Conformational study on **1** with DNA. Both systems were modelled starting from the 1xrw structure, upon removal of the ligand. In the single acridine system, the ligand has been placed, in different orientations, 15 Å faraway from the G-C and C-G base pairs in which the

cognate ligand was originally intercalated. The base pairs position has been restrained with a force constant of 1000 kcal/mol Å 2 . In the multiple acridine system seven ligand copies have been randomly placed in the water box around the DNA octamer. No restrain was applied. To run the MD simulations the systems were embedded in a cubic box and solvated in TIP3P water molecules, with addition of Na+ and Clas counterions for neutralizing the total charge. The LINCS algorithm was employed to fix bond length between hydrogens and heavy atoms at the equilibrium distance. Periodic boundary conditions (PBC) were set, long range electrostatic effects were adjusted with the Particle-Mesh Ewald (PME) method, a cut-off value of 11Å was fixed for both electrostatic and van der Waals interactions. The complexes were first minimized using the steepest descent algorithm, then a slow equilibration (four steps in isothermal-isochoric (NVT) and two steps in the isothermal-isobaric canonical (NPT) ensembles, respectively) was performed for heating the system from 0 to 300 K, with a temperature ramp of 50 K every 1 ns. The Newton's equation was integrated every 2 fs, collecting frames every 10 ps, rescaling velocities with the Berendsen thermostat to control the temperature and coupling the system in NPT to a Parrinello-Rahman barostat. Lastly, a short equilibration of 2 ns in the NPT ensemble at 300K was carried out before the 1 μs long simulation in NVT ensemble. For the single acridine system we run fifteen 50/100 ns long replicas, while for the multiple acridine systems three 300 ns long replicas were simulated. The ligand placement and the system setup were performed using the BiKi software suite (http://www.bikitech.com/).

Plain Molecular Dynamics with compound 2. The most probable proromeric state of the nitrosylated doxorubicin derivative **2** was check and assigned using Moka [114]. The ligand was parametrized with the ab initio RESP charges fitting methodology, as implemented in the BiKi Life Science software suite [115]. The MD

simulation setup was performed with BiKi. Gromacs 4.6.1 was used to run MD simulations [116]. The water model employed was TIP3P. The solvated system was preliminary minimized by 5000 steps of steepest descent. The integration step was equal to 1 fs. The Verlet cutoff scheme, the Bussi−Parrinello thermostat, LINCS for the constraints (all bonds), and the particle mesh Ewald for electrostatics, with a short-range cutoff of 11 Å, were applied. The system was equilibrated in four subsequent steps: 100 ps in NVT ensemble at 100 K, 100 ps in NVT ensemble at 200 K, 100 ps in NVT ensemble at 300 K, and a 1 ns long NPT simulation to reach the pressure equilibrium condition. No restraint was applied. The production run was carried out in the NVT ensemble at 300 K without any restraint for 50 ns. Two replicas were simulated upon velocity reassignment.

Upon completion of the simulation we employed the algorithm proposed in Decherchi et al [117]. and used the backbone RMSD with optimal alignment (Kabsch algorithm) between frames as metric for distance computation, to cluster the trajectories. We obtained ten clusters for each replica and inspected the corresponding representative medoid.

Molecular Docking with compound 2. The reference crystallographic structure used for static and dynamic docking simulations was retrieved from the Protein Data Bank (PDB code 1xrw) [118]. The structure originally contained a platinum acridine derivative, intercalating a DNA octamer in between G-C and C-G base pairs. The cognate ligand was removed and the binding site, thus defined, used for the following simulations.

Static docking simulations were performed using the GOLD suite version 5.5. Five different poses were generated and scored with CHEMPLP scoring function. the DNA octamer was maintained rigid. The best docking pose, in complex with the

octamer was submitted to two plain MD replicas of 50 ns each to check the complex stability. The same settings reported in the MD paragraph were adopted.

Molecular Modeling of compound 3. The compound **3** was parametrized with the ab initio RESP charges fitting methodology [115]. The MD simulation setup was performed with BiKi and Gromacs 4.6.1 was used to run MD simulations [119]. The water model employed was TIP3P. The solvated system was preliminary minimized by 5000 steps of steepest descent. The integration step was equal to 1 fs. The Verlet cutoff scheme, the Bussi−Parrinello thermostat, LINCS for the constraints (all bonds), and the particle mesh Ewald for electrostatics, with a short-range cutoff of 11 Å, were applied. The system was equilibrated in four steps: 100 ps in NVT ensemble at 100 K, 100 ps in NVT at 200 K, 100 ps in NVT at 300 K. 1 ns long NPT simulation was subsequently run to reach the pressure equilibrium condition. No restraint was applied. The production was carried out in the NVT ensemble at 300 K for 20 ns. Three replicas were simulated upon velocity reassignment. To investigate if the compound can assume a U-shaped conformation, two plain molecular dynamics (MD) replicas of 20 ns each were performed. All the trajectories were cleaned, analyzed, and clustered, automatically generating 10 cluster for each. In the two trajectories, in 7/10 and 6/10 clusters, respectively, the compound assumed a U-shaped conformation. This conformation is strongly stabilized by π-π stacking and hydrophobic interactions.

Acknowledgements

Words cannot express my gratitude to all the people that with their precious contribution, made possible this work.

I'm extremely grateful to my tutor Prof. Salvatore Sortino, for giving me the possibility of working in his group and for having taught me everything I know. I am also thankful to all the people of the Photochemistry Laboratory for their help and support.

A special thanks to Professor Fabiana Quaglia (University of Napoli), Professor Roberta Fruttero (University of Turin), Professor Francesca Spyrakis (University of Turin), Professor Elena Reddi (University of Padova) and their groups for their contribution in part of this work.

I am also grateful to Professor Cameron Alexander for having hosted me in his laboratories and having given me the possibility to acquire new skills. I am also thankful to all the amazing people of the *Molecular Therapeutics and Formulation Laboratory* for their help.

Bibliography

[1] R. SoRelle, *Circulation*. **1998**, *98*, 2365-2366.

[2] *Nitric Oxide: Biology and Pathobiology*, ed. Ignarro, L. J. Elsevier Inc., **2010.**

[3] J.D. Luo, A.F. Chen*, Acta Pharmacol. Sin*., **2005**, *26*, 259-264.

[4] D. Fukumura,S. Kashiwagi, R. K. Jain, *Nat. Rev. Cancer,* **2006,** *6*, 521-534.

[5] Z. Huang, J. Fu, Y. Zhang, *J. Med. Chem.,* **2017**, *60*, 7617–7635.

[6] S. Moncada S, A. Higgs, *N. Engl. J. Med*., **1993**, *329*, 2002-2012.

[7] a) D. A. Geller, A. K. Nussler, M. Di Silvio, C. J. Lowenstein, R. A. Shapiro, S. C. Wang, R. L. Simmons, T. R. Billiar, *Proc. Natl. Acad. Sci. U. S. A.*, **1993**, *90*, 522−526. b), R. G. Knowles, S. Moncada, *Biochem. J.,* **1994**, *298*, 249−258.

[8] a) H.H. Al-Sa'doni, A. Ferro, *Mini Rev. Med. Chem.,* **2005**; *5,* 247-254; b) H. Yasuda, *Nitric Oxide,* **2008**, *19*, 205-216.

[9] M. Blangetti, A. Fraix, L. Lazzarato, E. Marini, B. Rolando, F. Sodano, R. Fruttero, A. Gasco, S. Sortino, *Chem. Eur. J.,* **2017**, *23*, 9026-9029.

[10] S. H. Abman, *Handb. Exp. Pharmacol*., **2013**, *218*, 257−276.

[11] P. G. Wang, M. Xian, X. Tang, X. Wu, Z. Wen, T. Cai, A. J. Janczuk, *Chem. Rev.*, **2002**, *102*, 1091-1134

[12] S. Mocellein, V. Bronte, D. Nitti, *Med. Res. Rev*., **2007**, *27*, 317–352.

[13] D. A. Wink, Y. Vodovotz, J. Laval, F. Laval, M. W. Dewhirst, J. B. Mitchell, *Carcinogenesis*, **1998**, *19*, 711–721.

[14] a) I.R. Hickok, D.D. Thomas, *Curr. Pharm. Des*, **2010**, *16*, 381-391; b) C.F. Chang, A.R. *Diers, N. Hogg, Free Radic. Biol. Med.*, **2015**, *79*, 324-336.

[15] S. Sortino, *J. Mater. Chem*., **2012**, *22,* 301-318.

[16] a) P. C. Ford, *Acc. Chem. Res*., **2008**, *41*, 190-200; b) P.C. Ford, **2013**, *34*, 56-65; c) H.J. Xiang, M. Guo, J. G. Liu, *Eur. J. Inorg. Chem*., **2017**, 1586-1595; c) N. L. Fry, P. K. Mascharak, *Acc. Chem. Res*., **2011**, *44*, 289-298.

[17] A. Fraix, S. Sortino, *Photochem. Photobiol. Sci*., **2018**, *17*, 1709-1727.

[18] a) E. B. Caruso, S. Petralia, S. Conoci, S. Giuffrida, S. Sortino*, J. Am. Chem. Soc.*, **2007**, *129*, 480-481; b) S. Conoci, S. Petralia, S. Sortino, Use of nitroaniline derivatives for the production of nitric oxide, EP 2051935A1/US20090191284, **2006**; c) T. Suzuki, O. Nagae, Y. Kato, H. Nakagawa, K. Fukuhara, N. Miyata, *J. Am. Chem. Soc*., **2005**, *127*, 11720-11726; d) K. Kitamura, N. Ieda, K. Hishikawa, T. Suzuki, N. Miyata, K. Fukuhara, H. Nakagawa*, Bioorg. Med. Chem. Lett.*, **2014**, *24*, 5660-5662.

[19] a) N. Ieda, Y. Hotta, N. Miyata, K. Kimura, H. Nakagawa*, J. Am. Chem. Soc.*, **2014**, *136*, 7085-7091; b) M. Blangetti, A. Fraix, L. Lazzarato, E. Marini, B. Rolando, F. Sodano, R. Fruttero, A. Gasco, S. Sortino, *Chem. – Eur. J*., **2017**, *23*, 9026-9029.

[20] a) K. Kitamura, M. Kawaguchi, N. Ieda, N. Miyata, H. Nakagawa, *ACS Chem. Biol*., **2016**, *11*, 1271–1278. b) H. He, Y. Xia, Y. Qi, H.-Y. Wang, Z. Wang, J. Bao, Z. Zhang, F.-G. Wu, H. Wang, D. Chen, D. Yang, X. Liang, J. Chen, S. Zhou, X. Liang, X. Qian and Y. Yang*, Bioconjugate Chem*., **2018**, *29*, 1194–1198.

[21] C. Parisi, M. Failla, A. Fraix, B. Rolando, E. Giaquinto, F. Spyrakis, E. Gazzano, C. Riganti, L. Lazzarato, R. Fruttero, A. Gasco, S. Sortino, *Chem. Eur. J*., **2019**, *25*, 11080-11084.

[22] J.P. Pellois, M. E. Hahn, T. W. Muir, *J. Am. Chem. Soc*., **2004**, *126*, 7170-7171.

[23] a) C. A. Robertson, D. Hawkins Evans and H. Abrahamse, *J. Photochem. Photobiol., B*, **2009**, *96*, 1–8.b) M. R. Hamblin and T. Hasan, *Photochem. Photobiol. Sci.*, **2004**, *3*, 436–450.

[24] a) A.P. Castano, T. N. Demidova, M. R. Hamblin, *Photodiagn. Photodyn. Ther*., **2004**, *1*, 279–293. b) J. P. Celli, B. Q. Spring, I. Rizvi, C. L. Evans, K. S. Samkoe, S. Verma, B. W. Pogue, T. Hasan, *Chem. Rev*., **2010**, *12*, 2795–2838.

[25] P. R. Ogilby, *Chem. Soc. Rev.*, **2010**, *39*, 3181–3209.

[26] a) F. Quaglia, S. Sortino, in Applied Photochemistry: When Light Meets Molecules, ed. G. Bergamini and S. Silvi, Springe International Publishing, Switzerland, 2016, 397–426. b) A. Fraix, N. Marino, S. Sortino, *Top. Curr. Chem*., **2016**, *370*, 225–257.

[27] a) B. Halliwell, J. M. C. Gutteridge, **1993**. Oxidative stress: Adaptation, damage,repair and death. *In Free Radicals in Biology and Medicine*, 3rd Ed.; Oxford University Press Inc.: New York, 247–349; b) J. B. Hibbs Jr., R. R. Taintor, Z. Vavrin, *Science*, **1987**, *235*, 473-476; b) T. deRojas-Walker, S. Tamir, H. Ji, J. S. Wimollshnok, S. R. Tannenbaum, *Chem. Res. Toxicol*., **1995**, *8*, 473-477; c) K. Fukuhara, M. Kurihara, N. Miyata, *J. Am. Chem. Soc*., **2001**, *123*, 8662-8666.

[28] C. Parisi, A. Fraix, S. Guglielmo, F. Spyrakis, B. Rolando, L. Lazzarato, R. Fruttero, A. Gasco, S. Sortino, *Chem. Eur. J*., **2020**, *26*, 13627-13633.

[29] T. Matsubara, K. Kusuzaki, A. Matsumine, K. Shintani, H. Satonaka, A. Uchida, *Anticancer Res*., **2006**, *26*, 187-193.

[30] a) M. E. Lamm, J. D. M. Neville, *J. Phys. Chem*., **1966**, *69*, 3872–3877; b) D. J. Blears, S. S. Danyluk, *J. Am. Chem. Soc*., **1967**, *89*, 21–26.

[31] N. Ieda, Y. Hotta, N. Miyata, K. Kimura, H. Nakagawa, *J. Am. Chem. Soc*., **2014**, *136*, 7085-7091.

[32] D. Rehm, A. Weller, *Isr. J. Chem*. **1970**, *8*, 259-271.

[33] E. Lund, *Acta Chem. Scand*., **1957**, *11*, 990-996.

[34] M. Tanaka, K. Yukimoto, K. Ohkubo, S. Fukuzumi, *J. Photochem. Photobiol., A: Chem*., **2008**, *197*, 206-212.

[35] Estimated by the end of the absorption and the onset of the fluorescence emission spectra of **1**.

[36] A. Barducci, G. Bussi, M. Parrinello, *Phys. Rev. Lett.,* **2008**, *100*, 020603.

[37] a) S. Sortino, G. Condorelli, *New J. Chem*., **2002**, *26*, 250-258; b) S. Sortino, G. Marconi, G. Condorelli, *Chem. Comm*., **2001**, 1226-1227; c) S. Monti, S. Sortino, *Chem. Soc. Rev*., **2002**, *31*, 287-300.

[38] a) D. Zhao, J. Li, T. Yang and Z. He, *Biosens. Bioelectron*., **2014**, *52*, 29–35; b) M. Sayed, H. Pal, *Phys. Chem. Chem. Phys*., **2015**, *17*, 9519–9532; c) Y. Temerk, M. Ibrahim, H. Ibrahim and M. Kotb, *J. Electroanal. Chem.,* **2016**, *769*, 62–71; d) M. Shaikh, J. Mohanty, A. C. Bhasikuttan, V. D. Uzunova, W. M. Nau and H. Pal, *Chem. Commun*., **2008**, 3681–3683; e) M. Sayed, H. Pal, *J. Mater. Chem. C*., **2016**, *4*, 2685–2706; f) M. Sayed, K. Shinde, R. Shah, H. Pal, *Chemistry Select*, **2016**, **1**, 989–999; g) S. Freire, F. Rodriguez-Prieto, M. C. R. Rodriguez, J. C. Penedo, W. Al-Soufi and M. Novo, *Chem. – Eur. J*., **2015**, *21*, 3425–3434; h) M. M. Islam, V. K. Sonu, P. M. Gashnga, N. S. Moyon and S. Mitra, *Spectrochim. Acta*, Part A, **2016**, *152*, 23–33.

[39] a) A. Subastri, C. H. Ramamurthy, A. Suyavaran, R. Mareeswaran, P. L. Rao, M. Harikrishna, M. S. Kumar, V. Sujatha and C. Thirunavukkarasu, *Int. J. Biol. Macromol*., **2015**, *78*, 122–129; b) A. Manna, S. Chakravorti, *J. Phys. Chem. B,* **2012**, *116*, 5226–5233; c) M. F. Dehkordi, G. Dehghan, M. Mahdavi, M. A. H. Feizi, *Spectrochim. Acta*, **2015**, *145*, 353–359.

[40] a) M. Sayed, B. Krishnamurthy, H. Pal, *Phys. Chem. Chem. Phys*., **2016**, *18*, 24642-24653; b) A. K. Shaw, S. K. Pal, *J. Phys. Chem. B*, **2007**, *111*, 4189-4199; c) E. Fredericq, C. Houssier, *Biopolymers*, **1972**, *11*, 2281-2308.

[41] a) T. Esteves, C. Xavier, S. Gama, F. Mendes, P. D. Raposinho, F. Marques, A. Paulo, J. Costa Pessoa, J. Rino, G. Viola. I. Santos, *Org. Biomol. Chem*., **2010**, *8*, 4104-4116; b) E. Pereira, L. do Quental, E. Palma, M. C. Oliveira, F. Mendes, P. Raposinho, I. Correia, J. Lavrado, S. Di Maria, A. Belchior, P. Vaz, I. Santos, A. Paulo, *Sci. Reports*, **2017,** *7*, 42544;

c) N. Agorastos, L. Borsig, A. Renard, P. Antoni, G. Viola, B. Spingler, P. Kurz, R. Alberto, *Chem. Eur. J*. **2007**, *13*, 3842-3852.

[42] A. M. Pyle, J. P. Rehmann, R. Meshoyer, C. V. Kumar, N. J. Turro, J. K. Barton, *J. Am. Chem. Soc*., **1989**, *111*, 3051-3058.

[43] M. B. Lyles, I. L. Cameron, *Biophys. Chem*., **2002**, *96*, 53-76.

[44] M. Sayed, H. Pal, *Phys. Chem. Chem. Phys*., **2015**, *17*, 9519-9532.

[45] N. A. Colabufo; F. Berardi; M. Cantore; M. Contino; C. Inglese; M. Niso; R. Perrone, *J. Med. Chem.,* **2010**, *53*, 1883-1997.

[46] a) C. Riganti, E. Miraglia, D. Viarisio, C. Costamagna, G. Pescarmona, D. Ghigo and A. Bosia, *Cancer Res*., **2005**, *65*, 516-525; b) S. De Boo, J. Kopecka, D. Brusa, E. Gazzano, L. Matera, D. Ghigo, A. Bosia and C. Riganti, *Mol. Cancer*, **2009**, *8*, 108.

[47] A. Fraix, C. Parisi, M. Failla, K. Chegaev, F. Spyrakis, L. Lazzarato, R. Fruttero, A. Gasco, S. Sortino, *Chem.Commun*. **2020**, *56*, 6335-6335.

[48] A. Andreoni, E. J. Land, V. Malatesta, A. J. McLean, T. G. Truscott, *Biochim. Biophys. Acta, Gen. Subj.,* **1989**, *990*, 190-197.

[49] P. Sarathi Guin, S. Das, *Int. J. Electrochem.* Volume 2014, Article ID 517371, 8 pages, http://dx.doi.org/10.1155/2014/517371.

[50] *R.L. Momparler, M. Karon, S.E. Siegel, F. Avila, Cancer Res.* ***1976****, 36, 2891–2895.*

[51] O Tacar; P. Sriamornsak; C.R. Dass, *J. Pharm. Pharmacol*., **2013**, *65*, 157–170.

[52] a) M. Airoldi, G. Barone, G. Gennaro, A.M. Giuliani, M. Giustini, *Biochemistry*, **2014**, *53*, 2197-2207; b) A. Agudelo, P. Bourassa, G. Bérubé, H.-A. Tajmir-Riahi, *Int. J. Biol. Macromol.*, **2014**, *66*, 144-150.

[53] G. Viola, H. Ihmels, H. Kraußer, D. Vedaldi, F. Dell'Acqua, *ARKIVOC* (Gainesville, FL, U.S.), **2004**, 219.

[54] C. Parisi, F. Moret, A. Fraix, L. Menilli, M. Failla, F. Sodano, C. Conte, F. Quaglia, E. Reddi, S. Sortino, *ACS Omega,* **2022**, 7, *9*, 7452–7459.

[55] F. Xu, F. Wang, T. Yang, Y. Sheng, T. Zhong, Y. Chen, *Cancer Cell Int*., **2014**, *14*, 142-154.

[56] C. Peetla, R. Bhave, S.; Vijayaraghavalu, A. Stine, E. Kooijman, V. Labhasetwar, *Mol. Pharm.,* **2010**, *7*, 2334–2348.

[57] D. Sleep, J. Cameron, L.R. Evans, *Biochim. Biophys. Acta*, **2013**, *1830*, 5526-5534.

[58] E. N. Hoogenboezem, C. L. Duvall, *Adv. Drug Delivery Rev.,* **2018**, *130*, 73–89.

[59] X.M. He, D.C. Carter, *Nature*, **1992**, *358*, 209-215.

[60] R.F. Steiner, L. Weinryb, Plenum Press, New York, 1971, p. 40.

[61] J. R. Lakowicz, Principles of fluorescence spectroscopy, second ed., Plenum Press, New York, 1999, pp. 237–265.

[62] N. Tayeh, T. Rungassamy, J.R. Albani, *J. Pharm. Biomed. Anal*. **2009**, *50*, 107–116.

[63] D. Agudelo, P. Bourassa, J. Bruneau, G. Bérubé, É. Asselin, H-A Tajmir-Riahi, *PLoS ONE*, **2012**, *7*, e43814.

[64] J. S. Mandeville, H. A. Tajmir-Riahi, *Biomacromolecules*., **2010**, *11*, 465–472.

[65] K. Chegaev, A. Fraix, E. Gazzano, G. E. F. Abd-Ellatef, M. Blangetti, B. Rolando, S. Conoci, C. Riganti, R. Fruttero, A. Gasco, S. Sortino, *ACS Med. Chem. Lett*., **2017**, *8*, 361-365.

[66] a) N. V. Blough, O. C. Zafiriou, *Inorg. Chem*., **1985**, *24*, 3502–3504; b) R. Kissner, T. Nauser, P. Bugnon, P. G. Lye, W. H. Koppenol, *Chem. Res. Toxicol*., **1997**, *10*, 1285–1292; c) S. Goldstein , G. Czapski, *Free Radical Biol. Med*., **1995**, *19*, 505–510.

[67] a) C. Szab´o, H. Ischiropoulos, R. Radi, *Nat. Rev. Drug Discovery*, **2007**, *6*, 662–679; b) J. S. Beckman, W. H. Koppenol, *Am. J. Physiol*., **1996**, *271*, 1424–1437; c) N. Hogg, V. M. Darley-Usmar, M. T. Wilson, S. Moncada, *Biochem. J*., **1992**, *291*, 419–424.

[68] C. Parisi, M. Failla, A. Fraix, L. Menilli, F. Moret, E. Reddi, F. Spyrakis, B. Rolando, L. Lazzarato, R. Fruttero, A. Gasco, S. Sortino, *Chem. Sci.,* **2021,** *12*, 4740-4746.

[69] a) M. Li, J. Xia, R. Tian, J. Wang, J. Fan, J. Du, S. Long, X. Song, J. W. Foley, X. Peng, *J. Am. Chem. Soc.*, **2018**, *140*, 14851–14859; b) B. Gurram, M. Li, M. Li, K. H. Gebremedhin, W. Sun, J. Fan, J. Wang, X. Peng, *J. Mater. Chem. B*, **2019**, *7*, 4440–4450.

[70] S. Verma, U. W. Sallum, H. Athar, L. Rosenblum, J. W. Foley, T. Hasan, *Photochem. Photobiol.*, **2009**, *85*, 111–118.

[71] The lowest excited singlet state of the N-nitroso unit is ca. 1.5 eV higher than the lowest excited singlet state of the benzophenothiazine chromophore.

[72] D. Rehm, A. Weller, *Isr. J. Chem.,* **1970**, *8*, 259-262.

[73] a) M. Jonsson, J. Lind, T.E. Eriksen, G. Merényi, *J. Am. Chem. Soc.*, **1994**, *116*, 1423-1427; b) Y. L. Chow, *Acc. Chem. Res.,* **1973**, *6*, 354-360.

[74] T. Ohno, N. N. Lictin, *J. Am. Chem. Soc.*, **1980**, *102*, 4636-4643.

[75] M. Montalti, A. Credi, L. Prodi, M.T. Gandolfi, Handbook of Photochemistry, 3rd ed., CRC Press, Boca Raton, **2006**.

[76] a) A. P. Castano, P. Mroz, M. R. Hamblin, *Nat. Rev. Cancer*, **2006**, *6*, 535–545; b) J. P. Celli, B. Q. Spring, I. Rizvi, C. L. Evans, K. S. Samkoe, S. Verma, B. W. Pogue, T. Hasan, *Chem. Rev*., **2010**, *12*, 2795–2838.

[77] a) I. J. McDonald, T. Doughery, *J. Porphyrins Phthalocyanines*, **2001**, *5*, 105-129; b) T. Hasan, A. C. E. Moor, B. Ortel, Cancer Medicine, Decker BC Inc., Hamilton, Ontario, Canada, 5th edn, 2000.

[78] L. J. Ignarro, J. M. Fukuto, J. M. Griscavage, N. E. Rogers, R. E. Byrns, *Proc. Natl. Acad. Sci. U. S. A*., **1993**, *90*, 8103–8107.

[79] T. P. Misko, R. J. Schilling, D. Salvemini, W. M. Moore, M. G. Currie, *Anal. Biochem*., **1993**, *214*, 11–16.

[80] N. S. Bryan, M. B. Grisham, *Free Radical Biol. Med*., **2007**, *43*, 645–657.

[81] N. Riosa, L. Piacenza, M. Trujillo, A. Mart´ınеza, V. Demichelia, C. Prolo, M. N. ´Alvareza, G. V. L´opezb, R. Radi, *Free Radical Biol. Med.*, **2016**, *101*, 284–295.

[82] C. Parisi, M. Seggio, A. Fraix, S. Sortino, *ChemPhotoChem*, **2020**, *4*, 742-748.

[83] a) A. Buldt, U. Karst, *Anal. Chem*., **1999**, *71*, 3003–3007; b) S. Uchiyama, T. Santa, T. Fukushima, H. Homma, K. Imai, *J. Chem. Soc. Perkin Trans. 2*, **1998**, 2165–2174; c) S. Uchiyama, T. Santa and K. Imai, *J. Chem. Soc. Perkin Trans. 2*, **1999**, 2525–2532.

[84] a) A. Fraix, M. Blangetti, S. Guglielmo, L. Lazzarato, N. Marino, V. Cardile, A. C. E. Graziano, I. Manet, R. Fruttero, A. Gasco, S. Sortino, *ChemMedChem*, **2016**, *11*, 1371-1379. b) C. Parisi, M. Failla, A. Fraix, A. Rescifina, B. Rolando, L. Lazzarato, V. Cardile, A. C. E. Graziano, R. Fruttero, A. Gasco, S. Sortino, *Bioorg. Chem*., **2019**, 8, 18-22.

[85] A. W. Girotti, *Cancers*, **2016**, *8*, 96-112.

[86] C. Parisi, G. Longobardi, A. C. E. Graziano, A. Fraix, C. Conte, F. Quaglia, S. Sortino, *Bioorg. Chem.*, **2022**, https://doi.org/10.1016/j.bioorg.2022.106050

[87] a) S. Tamesue, S. Noguchi, Y. Kimura, T. Endo; *ACS Appl. Mater. Interfaces*, **2018**, *10* 27381–27390. b) D. Wang, J. Fan, X. Gao, B. Wang, S. Sun, X. Peng, *J. Org. Chem*., **2009**, *74*, 7675–7683.

[88] J. P. Celli, B. Q. Spring, I. Rizvi, C. L. Evans, K. S. Samkoe, S. Verma, B. W. Pogue, T. Hasan, *Chem. Rev*., **2010**, *110*, 2795-2838.

[89] J. Zhao, K. Xu, W. Yang, Z. Wang, F. Zhong, *Chem. Soc. Rev*., **2015**, *44*, 8904-8939.

[90] S. Mathai, T. A. Smith, K. P. Ghiggino, *Photochem. Photobiol. Sci*., **2007**, *6*, 995-1002.

[91] a) E. Bassan, A. Gualandi, P. G. Cozzi, P. Ceroni, *Chem. Sci.,* ***2021****, 12*, 6607–6628. b) L. Huang, J. Zhao, S. Guo, C. Zhang, J. Ma, *J. Org. Chem*., **2013**, *78*, 5627−5637

[92] A. Venuta, F. Moret, G. Dal Pogetto, D. Esposito, A. Fraix, C. Avitablie, F. Ungaro, M. Malinconico, S. Sortino, A. Romanelli, P. Laurenzio, E. Reddi, F. Quaglia, *Eur. J. Pharm. Sci.,* ***2018****, 111*, 177–185.

[93] S. Swaminathan, J. Garcia-Amoròs, A. Fraix, N. Kandoth, S. Sortino, F. M. Raymo, *Chem. Soc. Rev.,* **2014**, 43, 4167-4178.

[94] M. A, Filatov, S. Baluschev, C. Landfesterc, *Chem. Soc. Rev.,* ***2016****, 45*, 4668-4689.

[95] E. Swider, S. Maharjan, K. Houkes, N. K. van Riessen, C. Figdor, M, Srinivas, O. Tagit, *ACS Appl. Bio Mater*., **2019**, *2*, 1131-1140.

[96] C. Conte, G. Dal Poggetto, B. J. Swartzwelter, D. Esposito. F. Ungaro, P. Laurienzo, D. Boraschi, F. Quaglia, *Nanomaterials*, **2019**, *9*, 1354-1372.

[97] J. K. Barton, J. M. Goldberg, C. V. Kumar, N. J. Turro, *J. Am. Chem. Soc.,* **1986**, *108*, 2081-2088.

[98] K. M. Miranda, M. G. Espey, D. A. Wink, *Nitric Oxide: Biol. Chem.*, **2001**, *5*, 62–71.

[99] M. Işık, D. Levorse, D. L. Mobley, T. Rhodes, J. D. Chodera, *J. Comput. Aided Mol. Des.*, **2020**, *34*, 405–420.

[100] A. M. Bodratti, P. Alexandridis, *J. Funct. Biomater*. **2018**, *9*, 11, doi:10.3390/jfb9010011.

[101] J. Wang, R. M. Wolf, RJ. W. Caldwell, P. A. Kollman, D. A. Case, *J. Comput. Chem.* **2004**, *25*, 1157-1174.

[102] J. Wang, P. Cieplak and P. A. Kollman, *J. Comput. Chem*. **2000**, *21*, 1049-1074.

[103] F. Y. Dupradeau, A. Pigache, T. Zaffran, C. Savineau, R. Lelong, N. Grivel, D. Lelong, W. Rosanski, P. Cieplak, *Phys. Chem. Chem. Phys*. **2010**, *12*, 7821-7839.

[104] M. W. Schmidt, K. K. Baldridge, J. A. Boatz, S. T. Elbert, M. S. Gordon, J. H. Jensen, S. Koseki, N. Matsunaga, K. A. Nguyen, S. Su, et al. *J. Comput. Chem.* **1993**, *14*, 1347–1363.

[105] T. A. Halgren, *J. Comput. Chem.* **1996**, *17*, 616-641.

[106] N. M. O'Boyle, M. Banck, C. A. James, C. Morley, T. Vandermeersch, G. R. Hutchison, *J. Cheminform*., **2011,** 3, 33-47.

[107] W. L. Jorgensen, J. Chandrasekhar, J. D. Madura, R. W. Impey, M. L. Klein, *J. Chem. Phys*. **1983**, *79*, 926.

[108] J. C. Phillips, V. Braun, W. Wang, J. Gumbart, E. Tajkhorshid, E. Villa, C. Chipot, R. D. Skeel, L. Kalé, K. Schulten, *J. Comput. Chem.* **2005**, *26*, 1781-1802.

[109] U. Essmann, L. Perera, M. L. Berkowitz, *J. Chem. Phys.***1995**, *103*, 8577.

[110] S. E. Feller, Y. Zhang, R. W. Pastor, *J. Chem. Phys*. **1995**, *103*, 4613.

[111] G. Fiorin, M. L. Klein, J. Hénin, *Mol. Phys*. **2013**, *111*, 3345-3362.

[112] H. J. C. Berendsen, D. van der Spoel, R. van Drunen, *Comp. Phys. Comm*. **1995**, *91*, 43-56.

[113] W. Humphrey, A. Dalke, K. Schulten, *J. Molec. Graphics*. **1996,** *14*, 33-38.

[114] F. Milletti, L. Storchi, G. Sforna and G. Cruciani, *J. Chem. Inf. Model.* **2007**, *47*, 2172-2181.

[115] a) http://www.bikitech.com; b) S. Sciabola, P. Benedetti, G. D'Arrigo, R. Torella, M. Baroni, G. Cruciani and F. Spyrakis, *ACS Med. Chem. Lett.*, **2019**, *10*, 487-492.

[116] B. Hess, C. Kutzner, D. van der Spoel and E. Lindahl, *J. Chem. Theory Comput.*, **2008**, *4*, 435-447.

[117] S. Decherchi, A. Nerteotti, G. Bottegoni, W. Rocchia and A. Cavalli*, Nat. Commun*., **2015**, *6*, 6155-6165.

[118] H. Baruah, M. W. Wright and U. Bierbach, *Biochemistry,* **2005**, *44*, 6059-6070.

119] B. Hess, C. Kutzner, D. van der Spoel, E. Lindahl, *J. Chem. Theory Comput.*, **2008**, *4*, 435−447.